

# Hydrodeoxygenation of lignin-derived model compound isoeugenol over Fe-, Ni-, and Fe-Ni-supported on zeolites

**Master's Thesis**

**Bibesh Gauli**

Supervisors:

**Prof. Dmitry Murzin,**

**Docent Narendra Kumar and Associate Prof. Päivi Mäki-Arvela**



Johan Gadolin

Process Chemistry Centre

Laboratory of Industrial Chemistry and Reaction Engineering

Faculty of Science and Engineering

Åbo Akademi University

Turku/Åbo 2021, Finland

## Abstract

**Bibesh Gauli**

Hydrodeoxygenation of lignin-derived model compound isoeugenol over Fe-, Ni-, and Fe-Ni-supported on zeolites

**Master's Thesis**

Carried out under the supervision of Professor Dmitry Murzin, Associate Professor Päivi Mäki-Arvela, and Docent Narendra Kumar in the Laboratory of Industrial Chemistry and Reaction Engineering (Teknisk kemi och reaktionsteknik), Åbo Akademi University, Åbo/Turku

**Keywords**

HDO, lignin, renewable fuel, bio-oil, isoeugenol, zeolites, bifunctional catalysts, iron, precursors, catalyst characterizations, iron-nickel synergy

As the world is transitioning away from fossil fuels, lignocellulosic biomass is scrutinized as a source of renewable fuels and chemicals. Political motivations and environmental concerns have increased the research in lignin, an underutilized resource currently, as a potential source of bio-oils. These bio-oils cannot be used in the existing petroleum-based infrastructures due to their high oxygen content and complex structures. Hence, catalytic hydrodeoxygenation could be used to reduce the oxygen content of the bio-oils.

This thesis aims to contribute to the ever-growing knowledge of the HDO of lignin-derived model compounds, as the HDO of isoeugenol over Fe- and Fe-Ni-based catalysts was conducted for the first time in this work. The reaction was investigated at 300 °C, and 30 bar total H<sub>2</sub> pressure with hexadecane as a solvent. Iron was chosen for the metal modifications of zeolites because it is inexpensive, oxophilic, and environmentally friendly. The synthesized fresh and spent catalysts were characterized using different characterization techniques to explain their activity, selectivity, and stability in the HDO of isoeugenol.

The Fe-modified zeolites contained highly dispersed metal nanoparticles and microporous structures, according to the characterization results. However, the unreduced Fe-based catalysts exhibited poor activity in the HDO of isoeugenol as neither cycloalkanes nor alkylbenzenes were formed. A plethora of cracking products was produced, which could have originated both from the reactant and the solvent. The reduced Fe-based catalysts still did not exhibit sufficient HDO activity, as only minor concentrations of deoxygenated products were formed.

A suite of novel Fe, Ni, and Fe-Ni supported on H-Y-5.1 support was synthesized to study the synergistic effects of Fe and Ni active sites. Compared to the monometallic Fe and Ni catalysts, the bimetallic Fe-Ni catalyst exhibited better performance in the catalytic HDO of isoeugenol due to the synergy between Fe and Ni sites. The yield of the desired compounds such as propylcyclohexane, ethyl-methylcyclohexane, butylcyclopentane, and propylbenzene over the Fe-Ni catalyst with Fe to Ni weight ratio of 1:1 was 18%, 15%, 7%, and 3%, respectively.

## Acknowledgements

I am incredibly grateful to my supervisors' prof. Dmitry Murzin, associate prof. Päivi Mäki-Arvela, and docent Narendra Kumar. Thank you, prof. Dmitry Murzin for many inspiring courses about catalysis, chemical process technology, and giving me the chance to be part of this project. I want to thank associate prof. Päivi Mäki-Arvela for her methodological approach and guidance throughout the project. I want to pay my special gratitude to docent Narendra Kumar for teaching me different aspects of catalysis: from the synthesis of catalysts to characterization and testing.

I would like to thank all my colleagues from the Laboratory of Industrial Chemistry and Reaction Engineering in Åbo Akademi for their guidance and for sharing their knowledge with me, especially Dr. Kari Eränen, Dr. Irina Simakova, Dr. Zuzana Vajglová, and MSc. Mark Martinez-Klimov. I want to express my appreciation to Mr. Linus Silvander, Dr. Markus Peurla, Dr. Ilari Angervo, and Dr. Johan Linden for their invaluable assistance in the characterizations of the prepared catalysts.

I have learned a lot in the past two years studying and working as a research assistant in Åbo Akademi. Thank you, everyone, for these wonderful two years in Åbo/Turku.

There might be errors in this thesis that I am unaware of. I am solely responsible for all the mistakes and discrepancies found in this thesis.

Regards,

Bibesh

## List of Tables

<b>Table 1:</b> Compositions and properties of wood-based bio-oil and conventional fuel adapted from (13), (14).....	3
<b>Table 2:</b> Catalytic activities of Fe and Fe-Ni-based bifunctional catalysts that have been used in HDO of lignin-derived model compounds according to the literature.....	12
<b>Table 3:</b> Catalytic activities of supported noble metals-based bifunctional catalysts on the HDO of eugenol and isoeugenol according to the literature .....	15
<b>Table 4:</b> Chemicals used .....	21
<b>Table 5:</b> The catalysts prepared by the ion-exchange method with their characterization methods (loadings of catalysts determined by EDS) .....	23
<b>Table 6:</b> The catalysts prepared by the conventional evaporation-impregnation method, the deposition-precipitation method, and their characterization methods .....	24
<b>Table 7:</b> The performed characterizations for Ni, Fe, and Ni-Fe/H-Y-5.1 catalysts .....	25
<b>Table 8:</b> Reduction program used for the ex-situ reduction of catalysts before experiments .....	25
<b>Table 9:</b> GC retention times of compounds present in the liquid phase in the HDO of isoeugenol.....	26
<b>Table 10:</b> Average metal particle size of some Fe-Beta catalysts determined by TEM .....	33
<b>Table 11:</b> H <sub>2</sub> -TPR results of different Fe-Beta catalysts.....	37
<b>Table 12:</b> H <sub>2</sub> -TPR results of monometallic and bimetallic catalysts synthesized on H-Y-5.1 support.....	38
<b>Table 13:</b> Textural properties of Ni, Fe, and Ni-Fe/H-Y-5.1 catalysts.....	40
<b>Table 14:</b> Textural properties of Fe catalysts prepared with the ion-exchange method.....	40
<b>Table 15:</b> Textural properties of Fe catalysts prepared with the evaporation-impregnation method and the deposition-precipitation method .....	41
<b>Table 16:</b> Acidity measurements of the synthesized Fe-modified catalysts by FTIR .....	42
<b>Table 17:</b> Average particle size determined by TEM and XRD .....	45
<b>Table 18:</b> Name of the products formed during the HDO of isoeugenol with 5 wt.% Fe - 5 wt.% Ni/H-Y-5.1 as identified by GC-MS.....	52
<b>Table 19:</b> The results from HDO of isoeugenol over Fe, Ni, and Fe-Ni catalysts. Nomenclature: DH (dihydroeugenol) and PCH (propylcyclohexane). .....	54

## List of Figures

<b>Figure 1:</b> Monomers of lignin: <b>a)</b> p-coumaryl alcohol, <b>b)</b> coniferyl alcohol, and <b>c)</b> sinapyl alcohol adapted from [2].	2
<b>Figure 2:</b> <b>a)</b> Compounds found in lignin-derived bio-oils and <b>b)</b> possible reaction mechanisms of these compounds during HDO upgrading adapted from [8,20].	4
<b>Figure 3:</b> Proposed reaction mechanisms by different active sites in bifunctional catalysts adapted from [1].	7
<b>Figure 4:</b> Framework structures of <b>a)</b> Faujasite (zeolite Y), <b>b)</b> BEA (beta), and <b>c)</b> MOR (mordenite) in the right adapted from International Zeolite Association [49].	9
<b>Figure 5:</b> A simplified reaction scheme showing guaiacol HDO over Fe/SiO <sub>2</sub> with the formation of an intermediate product (phenol) and the desired products (benzene and toluene) adapted from [1,52].	9
<b>Figure 6:</b> The proposed reaction mechanisms for HDO of guaiacol over different Ni and Fe-based monometallic and bimetallic catalysts, namely: (a) Ni/CNT, (b) Ni <sub>5</sub> -Fe <sub>1</sub> /CNT, (c) Fe/CNT, and (d) Ni <sub>1</sub> -Fe <sub>5</sub> /CNT adapted from [45].	11
<b>Figure 7:</b> The proposed reaction pathways for catalytic HDO of isoeugenol over bifunctional Pt/H-Beta and Ir/H-Beta catalysts adapted from (19).	15
<b>Figure 8:</b> SEM micrographs (left) and crystal size distribution (right) of fresh and spent 5 wt.% Fe - 5 wt.% Ni/H-Y-5.1.	31
<b>Figure 9:</b> TEM micrograph (left) and the particle size distribution (right) of 7 wt.% Fe/H-Beta-25 prepared with the ferric acetate precursor.	32
<b>Figure 10:</b> TEM micrograph (left) and the Fe particle size distribution (right) of 9.5 wt.% Fe/H-Beta-38 prepared with the ferric chloride precursor.	32
<b>Figure 11:</b> TEM micrographs (left) and particle size distributions (right) of the fresh and the spent 5 wt.% Ni/H-Y-5.1.	33
<b>Figure 12:</b> TEM micrographs (left) and particle size distributions (right) of fresh and spent 5 wt.% Fe - 5 wt.% Ni/H-Y-5.1.	34
<b>Figure 13:</b> TEM micrographs (left) and particle size distributions (right) of fresh and spent 5 wt.% Fe/H-Y-5.1.	35
<b>Figure 14:</b> H <sub>2</sub> -TPR profiles of some Fe-modified Beta catalysts. Catalyst 1 is prepared with the deposition-precipitation method, and the rest of the catalysts are synthesized with the evaporation-impregnation method.	36
<b>Figure 15:</b> H <sub>2</sub> -TPR profiles of Fe/H-Y-5.1, Ni/H-Y-5.1, and Fe-Ni/H-Y-5.1.	38
<b>Figure 16:</b> N <sub>2</sub> adsorption-desorption isotherms (left) and pore distribution curves (right) of 5 wt.% Fe/H-Y-5.1, 5 wt.% Ni/H-Y-5.1, and 5 wt.% Fe - 5 wt.% Ni/H-Y-5.1.	40
<b>Figure 17:</b> XRD patterns of 2.5 wt.%, 7 wt.%, and 12.5 wt.% H-B-25 prepared by the ion-exchange method with the ferric acetate precursor.	43
<b>Figure 18:</b> XRD images of 5wt.% Ni/H-Y-5.1, 5 wt.% Fe/H-Y-5.1, and 5 wt.% Fe - 5 wt.% Ni/H-Y-5.1.	44
<b>Figure 19:</b> Mössbauer spectra of two different Fe-modified zeolites prepared by the ion-exchange method: 7 wt.% Fe/H-Beta-25-FeAc (left) and 9 wt.% Fe/H-Beta-38-FeAc (right).	45
<b>Figure 20:</b> Conversion of isoeugenol, dihydroeugenol, and GCLPA % versus time in isoeugenol HDO at 300 °C and 30 bar total pressure in the absence of any catalyst.	47

**Figure 21:** GC retention times of the products formed during experiment using an unreduced 9 wt.% Fe/H-Beta-38-FeN with the solvent only (red) and solvent with the reactant (black). .....48

**Figure 22:** **a)** Conversion of isoeugenol, dihydroeugenol, GCLPA% and CB% versus time and **b)** selectivity to products by the carbon number and the yield versus time over 5 wt.% Fe/H-Y-5.1 .....49

**Figure 23:** **a)** Conversion of isoeugenol, dihydroeugenol, GCLPA% and CB% versus time and **b)** selectivity by the carbon number and the yield versus time over 5 wt.% Ni/H-Y-5.1. ....50

**Figure 24:** GC retention times of the products formed during the HDO of isoeugenol with 5 wt.% Fe - 5 wt.% Ni/H-Y-5.1.....51

**Figure 25:** **a)** Molar concentrations of the products versus time, **b)** conversion of isoeugenol, dihydroeugenol, GCLPA% and CB% versus time, and **c)** selectivity by the carbon number versus time over 5 wt.% Fe - 5 wt.% Ni/H-Y-5.1. ....53

**Figure 26:** The proposed reaction pathways for the HDO of isoeugenol over Fe-Ni/H-Y-5.1.56

## List of abbreviations

HDO:	Hydrodeoxygenation
ASTM:	American Society for Testing and Materials
n/d:	not defined
HDS:	Hydrodesulfurization
MCS:	Mesoporous Carbon Spheres
MWCNT:	Multi-walled carbon nanotube
WLHSV:	Weight liquid hourly space velocity
WHSV:	Weight hourly space velocity
XRD:	X-ray powder diffraction
SEM:	Scanning Electron Microscopy
FTIR:	Fourier Transform Infrared Spectroscopy
GC-MS:	Gas chromatography – Mass Spectrometry
GC-FID:	Gas chromatography – Flame Ionization Detector
FID:	Flame Ionization Detector
TCD:	Thermal Conductivity Detector
TEM:	Transmission Electron Microscopy
CNT:	Carbon nanotubes
TPR:	Temperature Programmed Reduction
BTX:	benzene, toluene, and xylene
PCH:	Propylcyclohexane
FeAc:	Ferric acetate
FeN:	Ferric nitrate
FeCl <sub>3</sub> :	Ferric chloride
CB:	carbon balance
IMC:	Intermetallic compounds

## Table of Contents

<b>1</b>	<b>Introduction</b>	<b>1</b>
1.1	<b>Components of lignocellulosic biomass</b>	<b>1</b>
1.2	<b>Bio-oils and different model compounds</b>	<b>2</b>
1.2.1	Properties of bio-oils	3
1.2.2	Model compounds of bio-oils	4
1.2.3	Isoeugenol as a model compound	5
1.3	<b>Hydrodeoxygenation (HDO) reaction</b>	<b>5</b>
1.4	<b>Zeolites and bifunctional catalysts</b>	<b>6</b>
1.5	<b>Literature review of catalysis in HDO reaction</b>	<b>7</b>
1.5.1	HDO of phenolic compounds over Fe- and Fe-Ni-based catalysts	8
1.5.2	HDO of phenolic compounds over supported noble metal catalysts	14
1.5.3	HDO of isoeugenol over Fe supported transition metal catalysts	17
1.6	<b>Catalyst characterization methods</b>	<b>17</b>
1.6.1	Scanning Electron Microscopy and Energy Dispersive X-rays Spectroscopy (SEM-EDS)	17
1.6.2	Transmission Electron Microscopy (TEM)	17
1.6.3	Temperature Programmed Reduction (TPR)	18
1.6.4	Nitrogen physisorption	18
1.6.5	Fourier-transform infrared (FTIR) spectroscopy	18
1.6.6	X-Ray Diffraction (XRD)	19
1.6.7	Mössbauer Spectroscopy	19
1.7	<b>Analysis of reaction mixtures</b>	<b>19</b>
1.7.1	Gas chromatography (GC) for analysis of liquid phases	20
1.7.2	Gas chromatography-mass spectrometry (GC-MS) for substance detection	20
1.8	<b>Objectives and scope of catalyst preparation and HDO of isoeugenol</b>	<b>20</b>
<b>2</b>	<b>Experimental</b>	<b>21</b>
2.1	<b>Chemicals</b>	<b>21</b>
2.2	<b>Catalyst synthesis</b>	<b>22</b>
2.2.1	Precursors and supports used for the preparation of Fe-based catalysts	22
2.2.2	Catalyst synthesis methods	22
2.2.3	Synthesis of Fe-supported bifunctional catalysts	22
2.2.4	Synthesis of Fe, Ni, and Fe-Ni supported bifunctional catalysts on H-Y-5.1	24

2.2.5	Reduction procedures.....	25
<b>2.3</b>	<b>Batch reactor set-up, analyses of the reaction products, and catalyst characterization .....</b>	<b>25</b>
2.3.1	Analysis of the reaction mixture .....	26
2.3.2	Catalyst characterization methods .....	27
2.3.3	Formulae and definitions .....	29
<b>3</b>	<b>Results and Discussion .....</b>	<b>30</b>
<b>3.1</b>	<b>Catalyst characterization results .....</b>	<b>30</b>
3.1.1	Scanning Electron Microscopy and Energy Dispersive X-rays Spectroscopy (SEM-EDS) .....	30
3.1.2	Transmission Electron Microscopy (TEM) .....	32
3.1.3	Temperature Programmed Reduction (TPR) .....	35
3.1.4	Nitrogen physisorption .....	39
3.1.5	Fourier-transform infrared (FTIR) spectroscopy.....	41
3.1.6	X-Ray Diffraction (XRD) .....	42
3.1.7	Mössbauer Spectroscopy.....	45
<b>3.2</b>	<b>Hydrodeoxygenation of isoeugenol .....</b>	<b>46</b>
3.2.1	HDO of isoeugenol on Fe-based monometallic catalysts .....	46
3.2.2	HDO of isoeugenol on Fe-Ni-based bimetallic catalysts.....	49
<b>4</b>	<b>Conclusions and Recommendations .....</b>	<b>57</b>
<b>5</b>	<b>References .....</b>	<b>60</b>
<b>6</b>	<b>Appendix I: Experimental set-up .....</b>	<b>64</b>
<b>7</b>	<b>Appendix II: SEM images.....</b>	<b>65</b>
<b>8</b>	<b>Appendix III: TEM images.....</b>	<b>69</b>
<b>9</b>	<b>Appendix IV: Mössbauer spectra.....</b>	<b>72</b>
<b>10</b>	<b>Appendix V: Experiments performed in the HDO of isoeugenol .....</b>	<b>73</b>
<b>11</b>	<b>Appendix VI: Mass spectra comparison .....</b>	<b>75</b>

# 1 Introduction

Lignocellulosic biomass has generated considerable interest as a source of renewable liquid fuels and chemicals due to the depletion of fossil-based feedstocks, and the environmental concerns associated with fossil fuels. Political motivations have also played a significant part in the research and development of renewable energy sources, as many governments have set ambitious goals to generate domestic energy and chemical production from biomass in the foreseeable future [1], [2], [3].

Lignocellulosic biomass has been used for decades in the production of paper via the Kraft process. This process utilizes cellulose to produce paper, whereas major biomass components such as hemicellulose and lignin are burned as low-value fuels [3]. Lignin, an underutilized resource currently, has enormous potential as a source of renewable energies, chemicals, and aromatic compounds due to its unique structure [3]. Compared to cellulose and hemicellulose, lignin is highly aromatic and contains lower oxygen content, making it suitable for fuels [4]. It also consists of the most reduced carbon fraction of lignocellulosic biomass and utilizes less hydrogen to form linear and cyclic alkanes [5]. Hence, considerable research is being done to develop lignin valorization processes [2].

One of the options in lignin valorization is the production of renewable jet fuels. Such fuels contain iso-paraffins, n-paraffins, naphthenes, olefins, and aromatics [6]. The aromatics and naphthenes in jet fuels can be produced from the pyrolysis of lignin [7]. In jet fuels, olefins are undesirable due to their high reactivity. ASTM regulations state that the arene content should be lower than 25% to diminish the soot formation [7]. However, a low aromatic content of 10–15% is still required to avoid leaks in the seals of fuel systems. In the commercial jet fuels studied by Pires et al. [6], naphthene content was found to be in the range of 3–15%. Additionally, small amounts of phenols were used as antioxidants in the fuel [6].

The complete hydrogenation of the phenolic ring derived from lignin on the metal sites of a bifunctional catalyst followed by dehydration and re-hydrogenation yield aliphatic hydrocarbons. These processes have high hydrogen consumption and reduction of carbon number of the compounds formed, which is not desired. Although the use of aromatics is limited in jet fuel by legislative and technical aspects, they can still be used as a blend in jet fuel [8].

## 1.1 Components of lignocellulosic biomass

The proper utilization of different fractions of lignocellulosic biomass requires understanding its various components or building blocks.

Lignocellulose consists of cellulose, hemicellulose, and lignin. The dry weight portions of cellulose, hemicellulose, and lignin range 35–50%, 20–35%, and 10–25%, respectively,

depending on cell types and sources [9]. Lignin, a three-dimensional amorphous polymer, fills the space between cellulose and hemicellulose in plant cell walls [3].

**Cellulose:** Cellulose is the most abundant organic polymer on earth. It is a polysaccharide consisting of a linear chain of  $\beta$ -1,4 linked D-glucose units. The degree of polymerization of this chain varies from hundreds to many thousands, depending on the plant species. The hydroxyl groups found in cellulose are bonded by hydrogen bonds that provide the compact crystalline structure of cellulose. Small amounts of unorganized cellulose chains make up the amorphous cellulose [9], [10].

**Hemicellulose:** The chemical structure of hemicellulose can vary depending on the plant. Hemicelluloses are branched heteropolymers consisting of monosaccharides such as pentoses (xylose, arabinose), hexoses (glucose, galactose, and mannose) and uronic acids. The degree of polymerization is usually around 200. Due to their branched structure, hemicelluloses are likely amorphous polymers. Xylan, the most abundantly found hemicellulose, consists of  $\beta$ -D-xylopyranosyl residues linked by 1,4 glycosidic bond [9,10].

**Lignin:** Lignin is a complex, cross-linked polymer consisting of phenolic monomers. The three phenyl propionic alcohols that are lignin monomers are coniferyl, p-coumaryl, and sinapyl alcohols (**Figure 1**). Different kinds of bonds, such as alkyl-aryl, alkyl-alkyl, and aryl-aryl ether bonds, exist in lignin that links these monomers together. Lignins do not contain regular structures like cellulose and are variable both in structures and compositions due to the variety of monomers of lignin and the random linkages between these monomers [9–11].

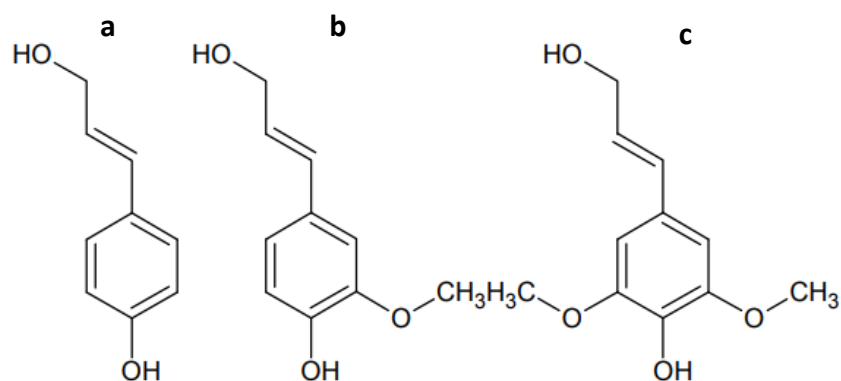


**Figure 1:** Monomers of lignin: **a)** p-coumaryl alcohol, **b)** coniferyl alcohol, and **c)** sinapyl alcohol adapted from [2].

## 1.2 Bio-oils and different model compounds

The transformation of lignocellulosic biomass to liquid fuels through flash pyrolysis and fast pyrolysis offers a cost-efficient method for biomass conversion. In the fast pyrolysis method, the biomass undergoes thermal degradation in a moderate temperature range of 450–600 °C and residence time of shorter than two seconds in the absence of oxygen. The yield of condensed bio-oil consisting of chemicals such as aldehydes, ketones, alcohols, phenolics, etc.,

through this process can be up to 75%. The fast pyrolysis products of lignin are such compounds as phenol, anisole, guaiacol (about 39%), cresol, syringol, etc. Additionally, char, noncondensable gases such as carbon dioxide and methane, and water are formed as products from fast pyrolysis [2,12,13].

### 1.2.1 Properties of bio-oils

The composition of bio-oil obtained from fast pyrolysis differs significantly depending on the used raw materials. The bio-oil contains high oxygen concentrations (up to 40 wt.%) and water (up to 30 wt.%), as depicted in **Table 1**. In addition, it is acidic (pH 2.8–3.8), highly viscous, has a low heating value which is less than half of the one for petroleum, due to its high oxygen content [2,14]. The oxygen-containing bio-oil has an increased tendency to polymerize. It is thermally and chemically unstable, and it is not miscible with conventional petroleum [15]. It cannot be used as such in the current petroleum-based infrastructures. Thus, the produced bio-oil must be upgraded by eliminating oxygen to convert it into high-quality transportation fuels or chemicals. Hence, catalytic deoxygenation is a critical step to selectively remove oxygen from pyrolysis oil to improve its properties as a fuel [4].

**Table 1:** Compositions and properties of wood-based bio-oil and conventional fuel adapted from (13), (14)

<b>Composition</b>		
Elemental analysis	Wood-based bio-oil (wt.%)	Fossil fuel (wt.%)
carbon	40–50	85
hydrogen	6.0–7.6	11–13
oxygen	36–52	0.1–1.0
nitrogen	0.00–0.15	0.1
sulfur	0.00–0.02	1.0–1.8
water	17–30	0.02–0.1
solid	0.03–0.7	1
<b>Properties</b>		
pH	2.4–2.8	–
specific gravity (kg/m <sup>3</sup> )	1.2	0.94
distillation residue (wt.%)	>50	1
viscosity (323 K), cP	13–30	180
higher heating value (MJ/kg)	16–20	40
density (kg/m <sup>3</sup> )	1.2–1.3	0.9–1.0

## 1.2.2 Model compounds of bio-oils

Due to the complexity in the chemical compositions of fast pyrolysis products, various complex reactions occur in the catalytic HDO process. HDO of pyrolysis oils is complicated to understand and model due to the plethora of these reactions occurring simultaneously. Thus, various lignin-derived bio-oil model compounds have been extensively studied in the literature to test synthesized catalysts and elucidate the respective reaction patterns and mechanisms. Guaiacol [16] seems to be the often used prototype compound to represent lignin-derived bio-oils, as it resembles lignin and its derivatives by consisting of two types of C-O bonds. Similarly, other lignin-derived oxygenates have been used as model compounds in the literature, such as phenol [17], p-cresol, 4-propyl-phenol, isoeugenol [18], anisole, vanillin, etc., [19] due to their similarities to depolymerized lignin (**Figure 2a**).

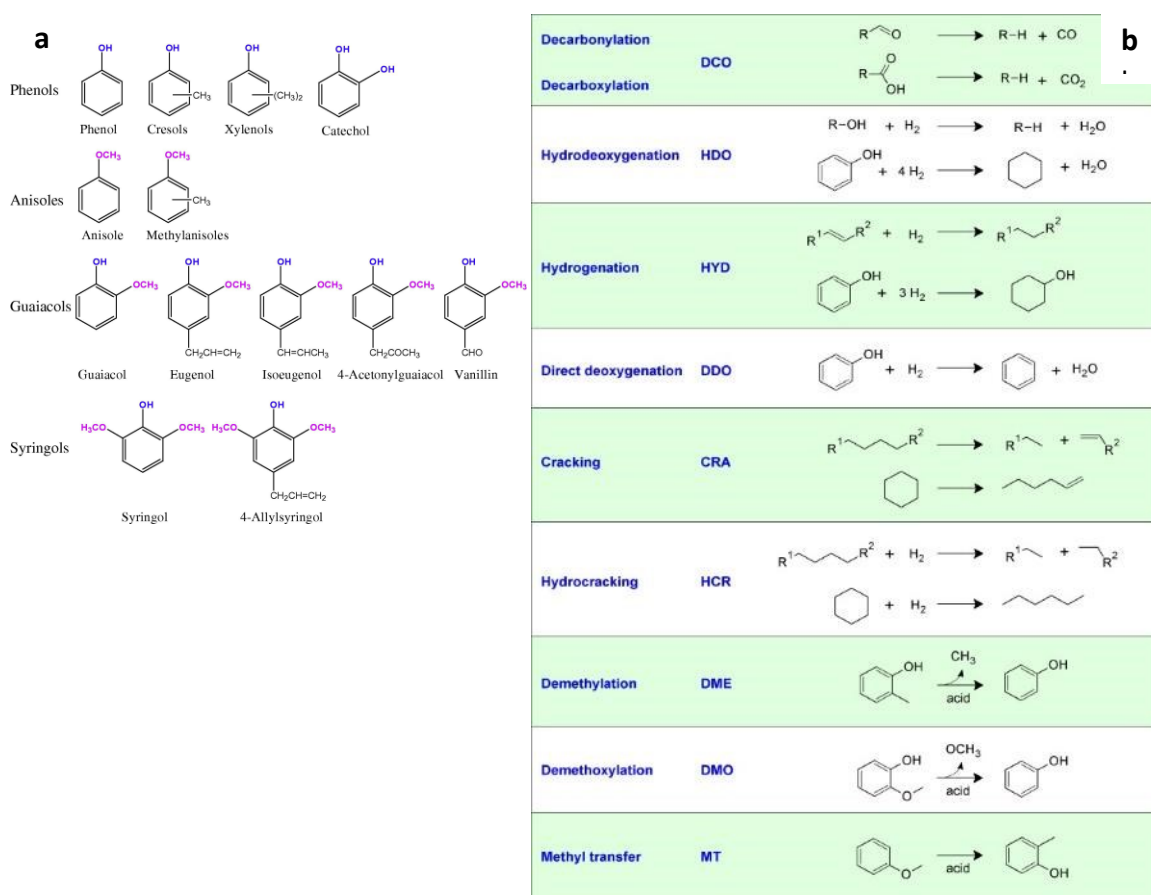


**Figure 2:** a) Compounds found in lignin-derived bio-oils and b) possible reaction mechanisms of these compounds during HDO upgrading adapted from [8,20].

### 1.2.3 Isoeugenol as a model compound

HDO of lignin-derived model compound isoeugenol has been less intensively studied compared to other model compounds. Some publications can be found in the literature about HDO of isoeugenol over nickel, cobalt, noble metals supported on silica, alumina, zirconia, etc. [18,21–23].

Isoeugenol is a good representative model as it contains the common methoxy, hydroxyl, and oxygenated allyl groups as depolymerized lignin and coniferyl alcohol [18]. Isoeugenol is a part of the guaiacol family and an isomer of eugenol. Many publications about eugenol HDO can be found in the literature [24–28].

## 1.3 Hydrodeoxygenation (HDO) reaction

In hydrodeoxygenation reaction, oxygen-containing compounds are converted to oxygen-free hydrocarbons and water at high hydrogen partial pressures (up to 200 bar) and temperatures of around 300 °C in the presence of a catalyst [14]. The purpose of HDO of bio-oil is to remove oxygen from the compounds, especially aromatic hydroxyl and methoxy-containing compounds, making the upgraded bio-oil favorable to be used as fuels [2]. An example of HDO is shown in the reaction below for a model compound [15]:



There are wide ranges of reactions occurring during catalytic HDO, such as decarboxylation, hydrogenation, hydrocracking, hydrogenolysis, dehydration, which modify the C-O-C, C-O-H, and C-C linkages (**Figure 2b**) [4]. As lignin-derived phenols contain several functional groups such as alkyl, hydroxyl, alkoxy, olefinic double bonds, etc., there is a competition between HDO reactions and hydrogenation reaction of double bond/aromatic ring during upgrading of these compounds. Excessive ring hydrogenation is not desired due to the high hydrogen consumption in such reactions and the high costs associated with such processes.

The catalysts used in catalytic HDO reactions are typically noble metals, transition metal carbides, bifunctional metal-acid catalysts, and metal sulfides supported on metal oxides or carbon. Among these catalysts, bifunctional catalysts containing both metal and acid sites have shown better hydrogenation and hydrodeoxygenation activity for the HDO of lignin-derived bio-oil [29]. The pre-sulfided forms of CoMo/Al<sub>2</sub>O<sub>3</sub> and NiMo/Al<sub>2</sub>O<sub>3</sub> catalysts similar to those used in the HDS process have also been investigated for the HDO process [30,31]. The major drawback for these catalysts is the need to use a sulfur source for catalyst activation, as biomass is nearly sulfur-free [15]. Noble metals such as Pt, Ru, and Pd loaded on carbon, H-Y, ZSM-5, etc., have shown excellent catalytic activity for HDO. The drawbacks for these catalysts are the high price of noble metals and their tendency towards aromatic ring hydrogenation, which increases the hydrogen consumption [4,32].

## 1.4 Zeolites and bifunctional catalysts

Zeolites are crystalline silicates and aluminosilicates with a three-dimensional framework consisting of  $\text{SiO}_4$  and  $\text{AlO}_4$  tetrahedra as building units [33], [34]. Due to the presence of aluminum in zeolites, one negative charge is developed at each tetrahedron having aluminum in its center. The zeolitic framework contains channels, channel intersections, and cages where water molecules and small cations are present that compensate for the negative framework charge [34]. These microporous solids with uniform pore sizes of 0.3–2 nm in diameter possess the unique property of shape selectivity due to the proximity of their pore dimensions with many substrate molecules. Due to their molecular dimensions, acidity, high internal surface area, and ability to confine metal species, zeolites are widely used in many heterogeneous catalytic processes [35], [36]. Synthetic zeolites with MFI, FAU, and BEA frameworks are used in many processes in oil refining and petrochemical industries [37]. Bifunctional catalysts are materials that contain two distinct types of active sites working in tandem in a surface-catalyzed reaction. These sites can either participate in the same chemical reaction step or separately catalyze different elementary steps in the reaction [1]. Bimetallic and metal-metal oxides are both examples of such bifunctional catalysts.

**Bimetallic catalysts:** The catalytic performance of a supported metal catalyst can be modified by adding another metal to the catalyst. The addition of a second metal might influence the properties of the first metal by ligand effects, ensemble effects, or bifunctional effects [1]. The ligand effect is the shifting of the d-band density of the first metal. Pt catalysts modified with 3d elements such as Ni, Co, Fe, and Ti have shown improved performance in the electrocatalytic oxygen reduction reaction due to the ligand effect [7], [8]. An example of the ensemble effect is the improvement of catalytic activity by adding Au to Pd olefin hydrogenation catalysts. The addition of relatively inactive Au decreases the number of adjacent Pd clusters, which have been shown to accumulate the unreacted species and reduce the activity of the catalyst [40]. In bifunctional effects, both the metals present at the surface of the catalyst participate in the reaction. In a study about the bifunctional effects of catalysts, dispersed biphasic Pd-Au nanoparticles were found to be highly active for low-temperature CO oxidation. The Pd sites from the catalysts participated in dissociative adsorption of oxygen, whereas the Au sites were involved in CO oxidation, as shown in **Figure 3a** [41]. Similarly, bimetallic Ni-Fe catalysts supported on MCSs showed better performance in the liquid-phase hydrodeoxygenation of phenol compared to their monometallic counterparts on the same support. Bimetallic catalyst with Ni/Fe weight ratio of 3/1 yielded around 93% of cyclohexane due to the formation of Ni-Fe alloy [42].

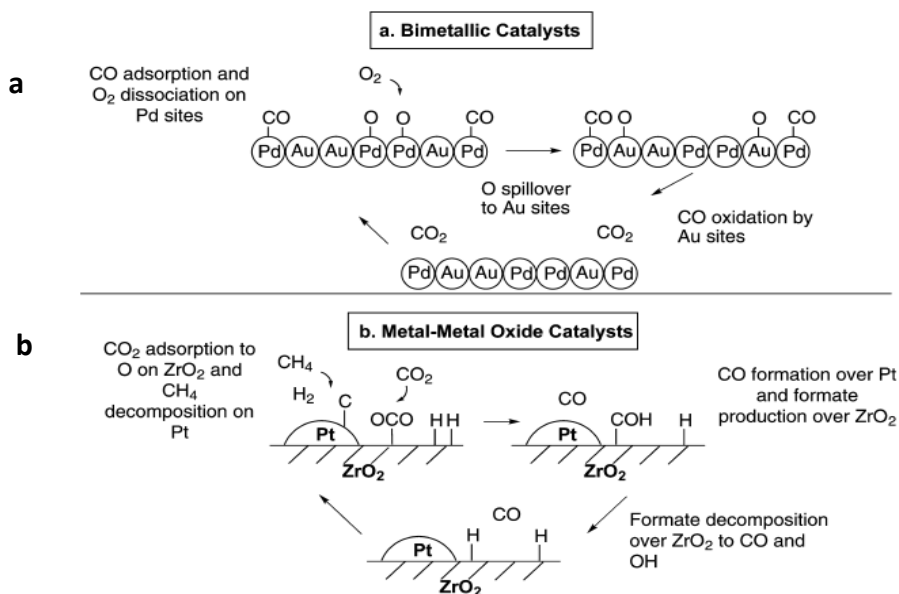


**Figure 3:** Proposed reaction mechanisms by different active sites in bifunctional catalysts adapted from [1].

**Metal-Metal Oxide Catalysts:** These types of bifunctional catalysts combine metal sites that perform hydrogenation/dehydrogenation function and acid sites that are active in protonation/deprotonation. For example, in the dry reforming of methane shown in **Figure 3b**, the Pt metal dehydrogenates methane, and the active sites at Pt/ZrO<sub>2</sub> catalyst serve to dissociate CO<sub>2</sub>. Therefore, the interfacial contact area plays a vital role in these kinds of bifunctional catalysts [1]. Similarly, bifunctional catalysts are efficient for transformations of phenolic compounds present in bio-oil [43]. Pt/H-Beta was found to be superior to H-Beta and Pt/SiO<sub>2</sub> in the hydrodeoxygenation of anisole due to the combination of the metal and acid sites [8]. Conversion and selectivity of lignin-derived phenolics over bifunctional metal/zeolites are influenced by the synergistic effect between these sites according to the following reaction aspects: (i) hydrogenation over metal sites; (ii) acid-catalyzed reactions over acid sites in combination with hydrogenation over metal sites; (iii) influence of porosity of the support, dispersion of the metal, and accessibility of the metal active centers by the molecules [44]. Thus, these factors influence the catalytic activity of metal-modified zeolites.

## 1.5 Literature review of catalysis in HDO reaction

According to the literature, bifunctional metal/zeolite catalysts and bimetallic catalysts are efficient in upgrading phenolics obtained from bio-oil through the HDO route [4,42,44]. The structure of the zeolite, pore-dimensions and acid sites influence the dispersion of metal nanoparticles of a metal-modified zeolite, which consequently affects its catalytic activity. The aspects that affect the performance of bifunctional metal/zeolite catalysts are [44]:

- Choice of the metal phase affects the reaction pathway. Fe as the metal phase on zeolites improves direct deoxygenation of phenolics, whereas the use of noble metals on zeolites promotes the hydrogenation-dehydration route.
- Size of metals and metal particle distributions also affect catalytic performance, as small particle sizes and higher metal dispersions are preferred. A low metal particle size distribution that provides more metal sites for the reaction and a balance between metallic and acidic sites are preferred. In the HDO of guaiacol over Fe-Ni/CNT, smaller metallic particles enhanced the hydrogenolysis of C-O bonds, while larger particles were found to be less active in the reaction [45].
- Acidity of the zeolitic support is required to maintain a synergistic effect between the metal and the acid sites. Strong acid sites favor HDO also leading to more side reactions such as hydro-isomerization and hydrocracking. Therefore, an optimum number of acid sites is required for efficient HDO [44,46].
- Appropriate pore sizes of zeolites are required to obtain a high metal dispersion and facilitate the diffusion of molecules inside the zeolitic channels. Large pore sizes provide space for the formation of large molecules and side reactions, which can deactivate the catalyst. In contrast, small pore sizes diminish diffusion of reactants/products within the zeolite pores [44].

### 1.5.1 HDO of phenolic compounds over Fe- and Fe-Ni-based catalysts

Bomont et al. [23] have demonstrated that the HDO of lignin-derived compound isoeugenol proceeds rapidly and to complete conversion with a high yield of the desired propylcyclohexane already at 200 °C and 30 bar hydrogen over Pt supported on different H-Beta zeolites. Similar results were obtained by Alda-Onggar et al. [22] over bimetallic IrRe and PtRe catalysts on Lewis acidic support alumina at 250 °C and 30–40 bar hydrogen pressure. However, due to the high costs of these noble metals, considerable research is currently being done to develop transition metal catalysts for HDO. Nickel, cobalt, and iron have all been studied for this purpose. Nickel-based catalysts have been extensively investigated as a cheaper alternative for the HDO process, as they have comparable activity to Pt-based catalysts. Compared to nickel and cobalt, iron has been scarcely studied for this process.

H-Beta, which has three-dimensional 12-membered ring channels ( $0.66 \times 0.67$  and  $0.56 \times 0.56$  nm) (**Figure 4b**), was chosen as the zeolitic support for this project because of its ability to accommodate larger phenolic compounds compared to zeolites with 10-membered ring such as ZSM-5 ( $0.51 \times 0.55$  and  $0.53 \times 0.56$  nm) [8]. The larger channels of H-Beta improve the diffusion of phenolic molecules inside the catalyst channels [47]. Similarly, the use of large-pore zeolitic support H-Y ( $0.74 \times 0.74$  nm) (**Figure 4a**)[43] might be beneficial for the dispersion of metal nanoparticles and the diffusion of phenolic compounds inside the catalyst channels to access these metal particles [44]. Yang et al. have asserted that there is a better Fe nanoparticles dispersion and smaller nanoparticles size on the catalyst prepared on Y zeolite compared to mordenite (**Figure 4c**) and ZSM-5 [48].

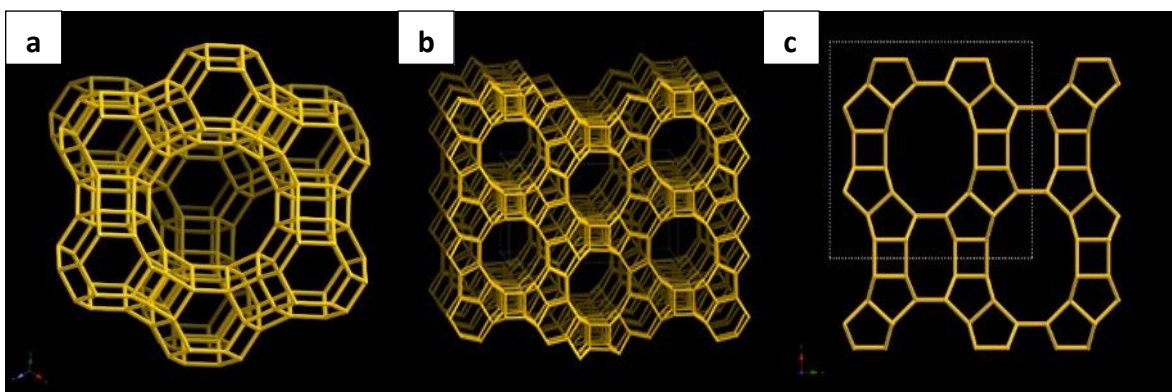


**Figure 4:** Framework structures of **a)** Faujasite (zeolite Y), **b)** BEA (beta), and **c)** MOR (mordenite) in the right adapted from International Zeolite Association [49].

Iron was chosen for the metal modifications of zeolites because it is inexpensive, oxophilic, and environmentally friendly. Iron has been proven effective by Rezaei et al. [47,50] for the selective conversion of lignin-derived phenolics into aromatic hydrocarbons on H-Beta, zirconia, rhenium oxide, MCM-41, etc. Due to the combination of mesoporosity, oxophilicity, and balanced acidity, FeReOx supported on ZrO<sub>2</sub> produced BTX with a high HDO efficiency (BTX yield of 50.5 wt.%) during HDO of m-cresol at 250 °C and 1 atm. When iron was combined with an acidic support such as H-Beta, saturated cyclic compounds were not produced. The reaction mechanism was postulated as the hydrogenation of the carbonyl group followed by dehydration leading to selective production of aromatic hydrocarbons due to the oxophilicity of iron [47,50].

Similar results were obtained by Nie et al. [51] during selective conversion of m-cresol to toluene over Ni, Fe, and Fe-Ni catalysts. It was stated that over Ni/SiO<sub>2</sub> catalyst ring hydrogenation occurs, leading to formation of 3-methylcyclohexanone and a lower HDO degree. In contrast, Fe/SiO<sub>2</sub> and bimetallic Fe-Ni/SiO<sub>2</sub> hydrogenate chemoselectively the carbonyl group of formed ketone intermediate to produce the desired toluene [51]. Olcese et al. achieved a 38% yield of benzene and toluene over Fe/SiO<sub>2</sub> with a high HDO selectivity. Fe/SiO<sub>2</sub> catalyst did not hydrogenate the aromatic ring (**Figure 5**). Hence, Fe is a compromise between activity and selectivity during HDO as minimal ring hydrogenation takes place on Fe compared to Ni and Co (**Table 2, entry 23**)[47].

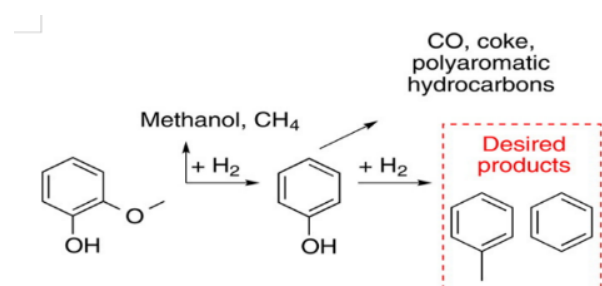


**Figure 5:** A simplified reaction scheme showing guaiacol HDO over Fe/SiO<sub>2</sub> with the formation of an intermediate product (phenol) and the desired products (benzene and toluene) adapted from [1,52].

Bimetallic catalysts have attracted considerable interest due to their unique properties and a better catalytic activity than their monometallic counterparts [48]. Fe-Ni bimetallic catalyst was chosen for this project because of its inexpensive preparation and high hydrogenation ability of Ni [46]. The use of Ni alone in HDO reactions is undesirable due to a tendency of Ni to saturate the benzene ring during the HDO of phenolics and high methanation activity. However, an addition of a more oxophilic metal such as Fe can modify the geometry and electronic properties of Ni, leading to formation of alloys or intermetallic compounds (IMC) [54,55].

The synergistic effects between Ni and Fe active sites promoting the HDO pathway have been discussed in many articles in the literature [42,45,51,55,56]. Ishihara et al. emphasized in their paper from 1986 that bimetallic Fe-Ni, Fe-Co, and Co-Ni supported on SiO<sub>2</sub> had better catalytic activities in the hydrogenation of carbon monoxide to produce olefins, paraffins, and gasoline compounds compared to the respective monometallic catalysts. Higher activity and selectivity were attributed to the formation of metallic alloys on the bimetallic catalysts [57].

Han et al. have confirmed in their paper a synergistic effect between Ni and Fe sites in the HDO of different lignin-derived compounds. They demonstrated that 10 wt.% and 20 wt.% loaded Ni-Fe/MCSs catalysts with Ni to Fe atomic ratio of 3:1 were excellent catalysts for the HDO of different model compounds such as guaiacol, phenol, catechol, etc. Increasing the Ni/Fe atomic ratio to more than 3:1 decreased the activity and selectivity of these catalysts to produce cyclohexane, which inferred that there is an optimum Ni/Fe atomic ratio (a volcano curve) for these catalysts to have synergy between metallic Ni and Ni-Fe alloy sites. All the bimetallic catalysts tested with different Ni and Fe ratios were found to be catalytically superior to the corresponding monometallic catalysts (**Table 2, entry 7–13**) [42]. Similarly, Fe-Co/SiO<sub>2</sub> catalyst tested by Cheng et al. exhibited better performance for the production of hydrocarbons than Fe/SiO<sub>2</sub> or Co/SiO<sub>2</sub> during the upgrading of bio-oils [58].

Fang et al. reported better guaiacol HDO activity of Fe-Ni bimetallic catalysts supported on carbon nanotubes than the monometallic catalysts [45]. Ni promotes hydrogen dissociation, whereas Fe has oxygen affinity, leading to the hydrogenation of aromatic ring and formation of cyclohexane when Ni/Fe atomic ratio is high, and the formation of phenol when Ni/Fe atomic ratio is low, as shown in **Figure 6**. They stated that the activity and the selectivity of these catalysts could be correlated with the Ni/Fe atomic ratio and nanoparticle size of these metals, and these parameters could be fine-tuned to produce cyclohexane or phenol as the main product (shown in **Table 2, entry 14–17**) [45].

The guaiacol molecule has the following three types of carbon-oxygen bonds [59,60]:

- i. C(sp<sub>3</sub>)-OAr (methoxy group) with the bond energy of 247 kJ/mol
- ii. C(sp<sub>2</sub>)-OMe with the bond energy of 356 kJ/mol
- iii. C(sp<sub>2</sub>)-OH (hydroxyl) with the bond energy of 414 kJ/mol

The phenol production over Fe-supported carbon nanotubes is thermodynamically favorable as demethoxylation has a lower bond dissociation energy than C(sp<sub>2</sub>)-OH bond [60]. However, in Ni-based catalysts, hydrogenation of the aromatic ring producing cyclohexane easily occurs after thermodynamically favored demethylation and demethoxylation steps due to the ability

of Ni to efficiently dissociate hydrogen [45]. This was in agreement with a study by Shafaghat et al. [43], who obtained cycloalkanes (cyclohexane, cyclopentane, etc.) over Ni/H-Beta and aromatic hydrocarbons (benzene, toluene, etc.) over Fe/H-Beta in the HDO of simulated bio-oil containing phenol (50 wt.%), o-cresol (25 wt.%) and guaiacol (25 wt.%). The selection of metals leads to the production of either cycloalkane through the hydrogenation-dehydration-hydrogenation route with Ni or benzene through the hydrogenolysis (direct deoxygenation) route with Fe (**Table 2, entry 1–5**).

Xu et al.[46] have demonstrated that the acidity of zeolitic support plays an essential role in the activity of bimetallic catalysts used in HDO reactions. The Fe-Ni/H-Beta catalyst showed the highest activity in the HDO of anisole at 350 °C and ambient pressure with a 24% yield of BTX (**Table 2, entry 18**). The catalytic activity decreased in the same order as the number of acid sites and intensity, i.e., Fe-Ni/H-Beta > Fe-Ni/HY > Fe-Ni/ZSM-5 > Fe-Ni/Al<sub>2</sub>O<sub>3</sub>.

In the conducted literature review, 20 wt.% loaded Ni-Fe/MCSs with the Ni/Fe atomic ratio of 3:1 was found to be the catalyst producing the highest yields of hydrocarbons in HDO of guaiacol (93.9%), p-cresol (96.7%), and eugenol (94.5%) as shown in **Table 2, entry 11–13**.

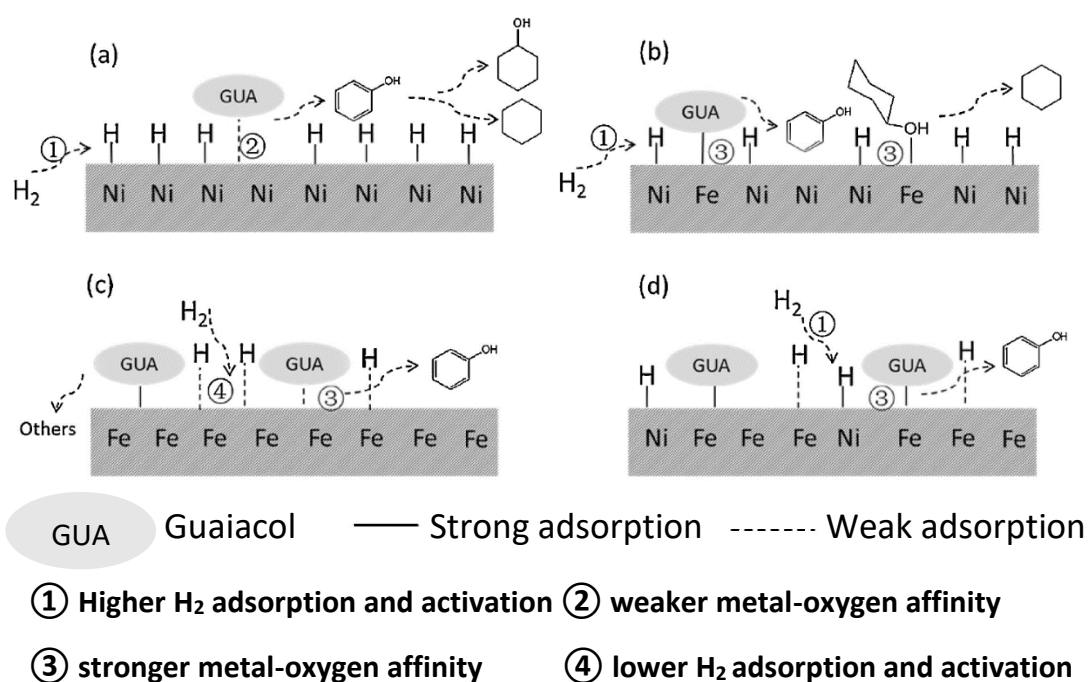


**Figure 6:** The proposed reaction mechanisms for HDO of guaiacol over different Ni and Fe-based monometallic and bimetallic catalysts, namely: (a) Ni/CNT, (b) Ni<sub>5</sub>-Fe<sub>1</sub>/CNT, (c) Fe/CNT, and (d) Ni<sub>1</sub>-Fe<sub>5</sub>/CNT adapted from [45].

**Table 2:** Catalytic activities of Fe and Fe-Ni-based bifunctional catalysts that have been used in HDO of lignin-derived model compounds according to the literature.

Entry	Catalyst	Solvent	Reactant	Reaction duration, pressure, temperature	Conversion %	Main products selectivity	Reference
1	5 wt.% Ni/H-Beta	Water	Phenol	4 h, 16 bar, 300 °C,	59	deoxygenated products: 38%	[43]
2	5 wt.% Ni/H-Beta		Phenol (50 wt.%), o-cresol (25 wt.%), guaiacol (25 wt.%)		Not given	deoxygenated products: 32%	
3	5 wt.% Fe/H-Beta					deoxygenated products: 24%	
4	2.5 wt.% Ni - 2.5 wt.% Fe /H-Beta	Water	phenol (50 wt.%), o-cresol (25 wt.%), guaiacol (25 wt.%)	4 h, 16 bar, 300 °C	Not given	deoxygenated products: 36.2%	[43]
5	5 wt.% Ni - 5 wt.% Fe/H-Beta				phenol = 50 cresol = 68 guaiacol = 88	deoxygenated products: 54%	
6	15 wt.% Fe/SiO <sub>2</sub>	–	guaiacol	0.5 h, 1 bar, 400 °C	92	Ybenzene and toluene = 71%	[61]
7	10 wt.% Ni/MCSs	dodecane	phenol	10 h, 50 bar, 250 °C,	99.6	Ycyclohexane = 8.7%	[42]
8	10 wt.% Fe/MCSs				6.4	Ycyclohexane = 0.2%	
9	10 wt.% Ni <sub>3</sub> - Fe <sub>1</sub> /MCSs (Ni:Fe=3:1)				99.8	Ycyclohexane = 49.8%	
10	20 wt.%		catechol	10 h, 50 bar,	99.9	hydrocarbons = 70.4%	

11	Ni <sub>3</sub> - Fe <sub>1</sub> /MCSs (Ni:Fe=3:1)	dodecane	guaiacol	250 °C,	99.4	hydrocarbons = 94%	
12	20 wt.%	dodecane	p-cresol	10 h, 50 bar,	99.9	hydrocarbons = 96.7%	[42]
13	Ni <sub>3</sub> - Fe <sub>1</sub> /MCSs (Ni:Fe=3:1)		eugenol	250 °C,	99.9	hydrocarbons = 94.5%	
14	7 wt.% Ni <sub>5</sub> - Fe <sub>1</sub> /CNT (Ni:Fe=5:1)	-	guaiacol	WLHSV <sub>GU</sub> A = 6.0 h <sup>-1</sup> , 30 bar, 300 °C	96.8	83.4% C6-ring selectivity to cyclohexane	[45]
15	5.5 wt.% Ni <sub>1</sub> - Fe <sub>5</sub> /CNT (Ni:Fe=1:5)				47.2	83.3% C6-ring selectivity to phenol	
16	7 wt.% Ni/CNT				79	53% C6-ring selectivity to cyclohexane	
17	6.5 wt.% Fe/CNT				17.2	40.4% C6-ring selectivity to phenol	
18	8.6 wt.% Fe - 10.8 wt.% Ni/ H-Beta	-		1 h, 1 bar, 350 °C	100	X <sub>HDO</sub> = 72.7% YBTX = 25%	[46]
19	8 wt.% Fe - 9.8 wt.% Ni/HY	-	anisole	1 h, 1 bar, 350 °C	94	X <sub>HDO</sub> = 68% YBTX = 7.11%	[46]
20	8 wt.% Fe - 9 wt.% Ni /ZSM-5				100	X <sub>HDO</sub> = 62% YBTX = 5.5%	
21	8.6 wt.% Fe - 10 wt.% Ni /Al <sub>2</sub> O <sub>3</sub>				31	X <sub>HDO</sub> = 71% YBTX = 16.6%	
22	5 wt.% Ni/SiO <sub>2</sub>	-	m-cresol	W/F=0.4 6 h, 1 bar, 300 °C	16.2	14.2% toluene	[51]
23	5 wt.% Fe/SiO <sub>2</sub>				8.8	60.2% toluene	
24	5 wt.% Ni/SiO <sub>2</sub> + 5 wt.% Fe/SiO <sub>2</sub> (physical mixture)				12.6	18.5% toluene	
25	5 wt.% Ni - 5 wt.% Fe/SiO <sub>2</sub>				13.7	52.6% toluene	

Notation:

$Y$  denotes the yield of products.

$X_{\text{HDO}}$  denotes HDO conversion

### 1.5.2 HDO of phenolic compounds over supported noble metal catalysts

A summary of the results obtained from eugenol and isoeugenol hydrodeoxygenation over supported noble metal catalysts is shown in **Table 3**. Alda-Onggar et al. [22] and Bomont et al. [23] have conducted HDO of isoeugenol over supported noble metal catalysts producing deoxygenated product propylcyclohexane, with high activity and selectivity. Alda-Onggar et al. produced propylcyclohexane with a yield of 99% over bimetallic IrRe catalyst supported on alumina. Similarly, Bomont et al. obtained propylcyclohexane with a high yield of 89% on Pt/H-Beta-300. The reaction scheme for isoeugenol HDO proposed by Bomont et al. is shown in **Figure 7**. Yohe et al. [62] obtained a 98% yield of propylcyclohexane in the HDO of dihydroeugenol, a hydrogenated product of isoeugenol, over bimetallic PtMo/MWCNT. They stated that the deoxygenation occurred through a bifunctional pathway, with hydrogenation occurring over Pt sites and dehydration over Mo sites. Zhang et al. performed HDO of eugenol over a physical mixture of 5 wt.% Pd/C and H-ZSM-5 zeolite with Si/Al ratios of 12.5 and 25. They obtained a high conversion of around 85% in both cases, and selectivity towards propylcyclohexane was 64.1% and 53.9%, respectively [24].

The highest yield of propylcyclohexane was obtained over IrRe/Al<sub>2</sub>O<sub>3</sub> (**Table 3, entry 3**). Such high HDO activity of the bimetallic IrRe catalyst was attributed to a high metal dispersion with a size close to 1 nm, mild acidity, and the presence of Re<sup>4+</sup> valence state. According to the authors, the activity of Ir for C-O bond hydrogenolysis and the Re<sup>4+</sup> valence state of rhenium are the reasons for an efficient bimetallic IrRe catalyst [22]. The high pressure of 40 bar was found to be suitable for the HDO reaction compared to 17 and 25 bar.

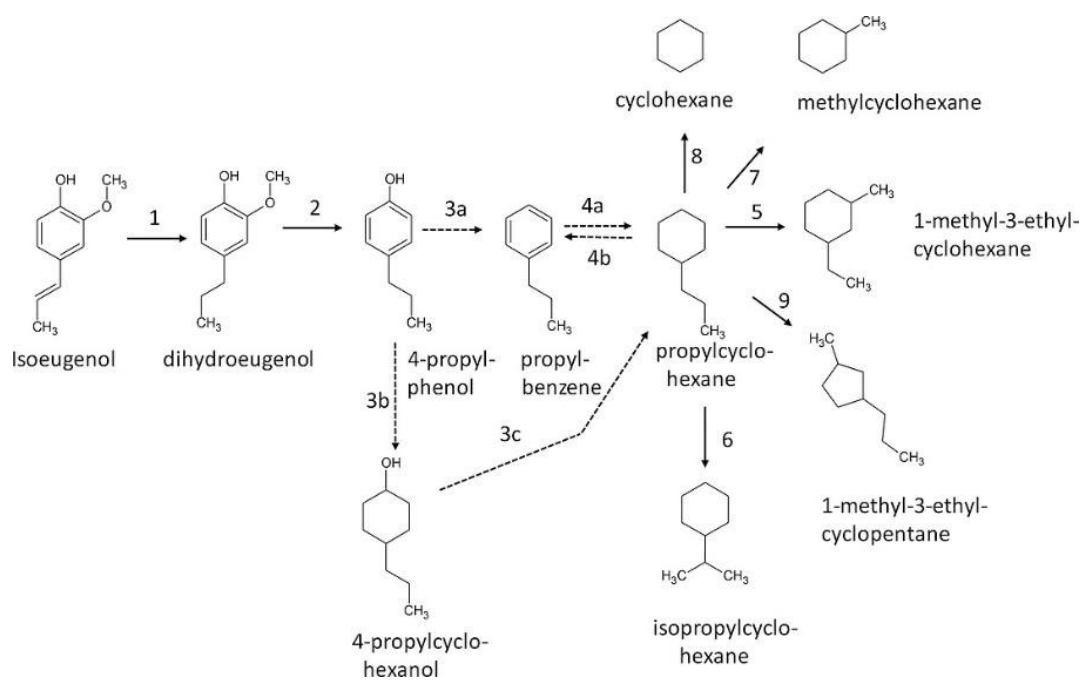


**Figure 7:** The proposed reaction pathways for catalytic HDO of isoeugenol over bifunctional Pt/H-Beta and Ir/H-Beta catalysts adapted from (19).

**Table 3:** Catalytic activities of supported noble metals-based bifunctional catalysts on the HDO of eugenol and isoeugenol according to the literature

Entry	Catalyst	Solvent	Reactant	Reaction duration, pressure, temperature	Conversion %	Yield of the main product	Reference
1	PtRe/Al <sub>2</sub> O <sub>3</sub>	dodecane	isoeugenol	4 h, 30 bar, 250 °C	100	propylcyclohexane: 54%	[22]
2	IrRe/Al <sub>2</sub> O <sub>3</sub>	dodecane	isoeugenol	4 h, 30 bar, 250 °C	100	propylcyclohexane: 69%	
3	IrRe/Al <sub>2</sub> O <sub>3</sub>	dodecane	isoeugenol	4 h, 40 bar, 250 °C	100	propylcyclohexane: 99%	
4	Pt/H-Beta-300	dodecane	isoeugenol	4 h, 30 bar, 200 °C	100	propylcyclohexane: 89%	[23]
5	Pt/H-Beta-150	dodecane	isoeugenol	4 h, 30 bar,	98	propylcyclohexane: 82%	

				200 °C			
<b>6</b>	Pt/H-Beta-25	dodecane	isoeugenol	4 h, 30 bar, 200 °C	100	propylcyclohexane: 82%	
<b>7</b>	Ru/Silica Alumina	hexadecane	eugenol	1 h, 30 bar, 250 °C	100	dihydroeugenol: 44% Propylcyclohexane: 15%	[63]
<b>8</b>	Pt/Silica Alumina	hexadecane	eugenol	1 h, 30 bar, 250 °C	100	dihydroeugenol: 75% Propylcyclohexane: 16%	
<b>9</b>	0.6 wt.% Pt/ $\gamma$ -Al <sub>2</sub> O <sub>3</sub>	n-hexane	eugenol	WHSV= 9h <sup>-1</sup> , 40 bar, 300 °C	77.27	cycloalkanes: 38.23% Propylcyclohexane: 24.43%	[64]
<b>10</b>	5 wt.% Pd/C + H-ZSM-5 (Si:Al=12.5) Physical mixture)	water	eugenol	4h, 50 bar, 240 °C	86.5	Selectivity: 64.1% towards propylcyclohexane	[24]
<b>11</b>	5 wt.% Pd/C + H-ZSM-5 (Si:Al=25) Physical mixture)	water	eugenol	4h, 50 bar, 240 °C	88.3	Selectivity: 53.9% towards propylcyclohexane	[24]
<b>12</b>	5 wt.% Pt - 2.5 wt% Mo/MWCNT	–	dihydroeugenol	WHSV= 5h <sup>-1</sup> , 24 bar, 300 °C	99.99	propylcyclohexane: 98%	[62]
<b>13</b>	2 wt.% Pd - 10 wt.% Fe/C	–	guaiacol	P <sub>guaiacol</sub> = 0.4kPa, P <sub>H<sub>2</sub></sub> =40 kPa, W/F= 0.15 s.g. STP/ml, 450 °C	100	benzene/toluene/TMB: 83.2%	[65]

### **1.5.3 HDO of isoeugenol over Fe supported transition metal catalysts**

According to our knowledge, HDO of isoeugenol over Fe-based catalysts is performed for the first time in the current work. HDO of isoeugenol over monometallic and bimetallic Fe and Ni supported on H-Y-5.1 zeolite is also done for the first time in this work. HDO of isoeugenol over other transition metals, i.e., Ni- and Co-based catalysts, can be found in the literature [18,21]. Lindfors et al. [21] have studied HDO of isoeugenol over Co supported on TiO<sub>2</sub>, SiO<sub>2</sub>, Al<sub>2</sub>O<sub>3</sub>, and SBA-15, and Ni supported on graphite and SiO<sub>2</sub>. They stated that the maximum yield of deoxygenated product, propylcyclohexane, and the highest GCLPA were obtained over 10 wt.% Co/SBA-15 mesoporous catalyst. Tieuli et al. [18] performed HDO of isoeugenol over non-acidic Ni-SBA-15 with a 75% yield of propylcyclohexane at 300 °C and 30 bar. A slightly acidic Ni-SZ-SBA-15 mesoporous catalyst exhibited lower HDO activity than the non-acidic Ni-SBA-15 mesoporous catalyst due to coking because of the oligomerization of phenolic compounds, and location of Ni inside the structure of the support [18].

## **1.6 Catalyst characterization methods**

The study of the physical and chemical properties of a synthesized catalyst is important in predicting, understanding, and explaining catalytic activity. The following characterization techniques have been used to study the physico-chemical properties such as morphology, texture, acidity, and reducibility:

### **1.6.1 Scanning Electron Microscopy and Energy Dispersive X-rays Spectroscopy (SEM-EDS)**

SEM-EDX is used to observe and analyze the microstructure morphology of catalytic materials. In this method, the sample is irradiated with a finely focused electron beam revealing information about its morphology and chemical composition. SEM has a much higher resolution than light-optical instruments and produces 3D images. These images are crucial in determining the catalyst morphology, surface, and internal microstructure of catalysts. EDX provides information about the elemental composition of materials [66].

### **1.6.2 Transmission Electron Microscopy (TEM)**

TEM is a powerful tool for material characterization. During TEM measurements, a high-energy beam of electrons is shown through a very thin sample, and the interactions between electrons and atoms are used to observe features about the material. 2D imaging in TEM is used to study morphology, porosity, texture, and channel systems of the synthesized catalysts.

TEM is also used in catalysis to analyze particle size, lattice structure, and defects, as it has a higher magnifying power and resolution than SEM [66].

### **1.6.3 Temperature Programmed Reduction (TPR)**

Temperature Programmed Reduction technique is used to study the reduction rates of metal oxide catalysts as a function of temperature [67]. This technique can be used to characterize oxidative-reductive properties of both bulk and supported catalysts by evaluating the ease of their reduction with hydrogen [68]. During TPR measurements, a gas used for reduction (for instance, H<sub>2</sub>) continuously flows through a porous catalyst. As the temperature is low at the beginning of TPR experiments, the reduction rate is almost zero. When the temperature is increased constantly, the reduction of a solid material increases and progresses until the material is completely reduced [69]. This method is used to determine the most suitable reduction conditions for the catalyst.

### **1.6.4 Nitrogen physisorption**

Nitrogen physisorption is utilized to determine specific surface area, pore-volume, and pore size distributions of catalytic materials. The determination of these parameters is important to understand and predict the catalytic activity of materials. Determining the pore dimension of a zeolite helps to predict the diffusion ability of various molecules inside the zeolite framework. Most experimental surface areas are derived from nitrogen adsorption isotherms at -196 °C. These are reported as either Langmuir surface area or BET surface area. BET measurements predict multilayer adsorption whereas, in the case of Langmuir, monolayer adsorption is supposed. In the BET method, typically, values at a relative pressure ( $P/P_0$ ) between 0.05 and 0.35 are taken [70]. The surface area of a microporous zeolite is evaluated by the Dubinin-Radushkevich method.

### **1.6.5 Fourier-transform infrared (FTIR) spectroscopy**

Adsorption of acidic or basic probe molecules on the catalyst and the determination of their amounts is done by FTIR spectroscopy [66]. In FTIR spectroscopy, radiation interference between two beams results in a signal called interferogram, which is usually generated by the Michelson interferometer [71]. FTIR can be used to characterize the Brønsted and Lewis acid sites on the surface of catalysts with the help of adsorbed probe molecules. Various basic probe molecules such as amines, ammonia, pyridine, and acidic probe molecule such as carbon dioxide can be used. The estimation of the amount and strength of surface active sites of catalysts with FTIR can be used to predict the catalytic performance in a given reaction and to optimize the properties of the catalyst [72].

## 1.6.6 X-Ray Diffraction (XRD)

XRD is one of the most frequently used characterization techniques in catalysis. X-rays have wavelengths in the angstrom range, which are sufficient to penetrate solids and probe their internal structures. When an X-ray beam penetrates a crystalline material, a diffraction pattern that reflects its structural property is formed. Diffraction patterns are like fingerprints that can identify the crystalline sample with the help of a database [73]. XRD is used to identify bulk phases and to estimate crystallite particle sizes. Diffraction patterns can be used to identify various phases in a catalyst. X-ray powder diffraction is applied to study the structure, phase purity, and presence of amorphous materials in catalysts. Furthermore, XRD can also measure the crystal size of metal nanoparticles in catalytic materials using the Scherrer equation [74]. However, due to the measurement limit of the instrument, metal nanoparticles that are less than 3 nm cannot be measured.

## 1.6.7 Mössbauer Spectroscopy

Mössbauer spectroscopy is a characterization technique in which  $\gamma$ -rays emitted from excited nuclei are absorbed by other nuclei of the same element, and hyperfine interactions between electrons and nuclear moments are subsequently measured. A Mössbauer spectrum has various observable parameters such as the isomer shift, electric quadrupole splitting, and magnetic dipole splitting [75], [76]. Mössbauer spectra provide information on:

- a) the oxidation state, coordination number, and ligand type of the resonant atom
- b) the electron distribution, molecular symmetry of the resonant atom
- c) the magnetic properties [74]

Mössbauer spectroscopy is mainly used to study iron (Fe) and tin (Sn). This spectroscopy, mainly with  $^{57}\text{Fe}$ , is used as a “fingerprint analysis” of iron-bearing compounds to determine the type of iron oxide present in the solid material [76]. In catalysis, this technique is applied to identify active sites or active phases for catalysis processes, study the correlation between structure and performance of catalysts, and characterization of catalysts during activation and deactivation [75].

## 1.7 Analysis of reaction mixtures

The analysis of the reaction mixture is important in identifying and determining the concentrations of substances formed during the reaction.

### **1.7.1 Gas chromatography (GC) for analysis of liquid phases**

Gas chromatography is an analytical tool in which gases or evaporated liquids to be analyzed pass through a chromatographic column consisting of a stationary phase and a mobile phase. The substances in the mixture have different affinities towards these phases and are separated. The chromatographic column consists of thin capillary tubes which can be from few meters to 100 m long. The tube is coated with a thin layer of a stationary phase which has different interactions with the components in the sample to separate them. The liquid stationary phase can be classified into two types: polyethylene glycol based or polydimethylsiloxane based. The mobile phase used to transport the mix in the capillary column are gases such as hydrogen, nitrogen, and helium [77].

### **1.7.2 Gas chromatography-mass spectrometry (GC-MS) for substance detection**

GC-MS is a powerful analytical technique with the ability to separate, detect, and identify a range of volatile and semi-volatile organic molecules even at trace levels in complex mixtures. The mass spectrum obtained from GC-MS is the fingerprint of a molecule [78].

## **1.8 Objectives and scope of catalyst preparation and HDO of isoeugenol**

The transformations of bio-oil using hydrodeoxygenation have been extensively studied in the literature using catalysts loaded with noble metals. However, cheaper Fe and Fe-Ni-based bifunctional catalysts have been only scarcely studied. The objective of this work was to study the HDO of lignin-derived phenolic compound isoeugenol in a batch reactor on monometallic (Fe) and bimetallic (Fe-Ni)-based catalysts on different supports. The scope of the project included the following catalyst synthesis research targets and investigation of isoeugenol HDO:

#### **Catalyst synthesis research targets:**

1. To study the influence of Fe precursors, preparation methods, acidities of Beta zeolites, metal loading, and zeolitic structure on the prepared bifunctional catalysts.
2. To characterize the fresh catalysts with different characterization techniques such as SEM, TEM, and FTIR. Select different catalysts for HDO testing based on these characterization results and the literature review.
3. To screen the catalysts and analyze the liquid phase products of the HDO reaction to assess if any reaction occurs under the used operational conditions with the prepared catalysts.
4. To characterize some spent catalysts to study crystal size, morphology, and coke formation after the reactions.

### Isoeugenol HDO research targets:

1. To perform a non-catalytic experiment for hydrogenation of isoeugenol under the selected operational conditions.
2. To compare the performance of different monometallic and bimetallic Fe-based catalysts supported on different zeolites.
3. To perform a set of reactions with three different catalysts made with the same preparation method to compare the product distributions. The three catalysts synthesized for this objective were Fe/H-Y-5.1, Ni/H-Y-5.1, and Fe-Ni/H-Y-5.1.
4. To determine the products obtained from the reaction as a function of time.

## 2 Experimental

The experimental section consists of the following subsections:

- Chemicals
- Catalyst synthesis
- Batch reactor set-up, analyses of the reaction products, and catalyst characterization

### 2.1 Chemicals

Chemicals used were obtained from different commercial sources and used without any purifications.

**Table 4:** Chemicals used

Chemical	Purity (%)	Supplier
Isoeugenol (cis and trans)	98	Sigma-Aldrich
n-Hexadecane	≥99	Alfa Aesar
4-propylphenol	99	Sigma-Aldrich
Nickel nitrate	-	CJSC Souzchimprom
Ferric nitrate nonahydrate	≥98	Sigma-Aldrich
Ferric nitrate nonahydrate	99.99	Sigma-Aldrich
Ferric chloride	97	Sigma-Aldrich
Ferric acetate basic pure	99	Riedel-de Haen AG
Ammonia solution 32%	32	Merck KGaA
NH <sub>4</sub> -Beta-25	-	Zeolyst International
NH <sub>4</sub> -Beta-38	-	Zeolyst International
H-Beta-300	-	Zeolyst International
H-Y-5.1	-	Zeolyst International
NH <sub>4</sub> -Mordenite-20	-	Zeolyst International

## 2.2 Catalyst synthesis

### 2.2.1 Precursors and supports used for the preparation of Fe-based catalysts

The zeolites used were obtained from Zeolyst International: BEA (nominal Si/Al = 25, Si/Al= 38, both NH<sub>4</sub> - form, and Si/Al= 300, H - form), MOR (nominal Si/Al = 20, NH<sub>4</sub> - form), Y zeolite (nominal Si/Al= 5.1, H - form). The ammonium forms of the obtained zeolites were converted into proton forms at 400 °C in a muffle oven using a step calcination procedure. The following scheme was used for calcination: 60 min – increasing temperature to 250 °C, then hold at 250 °C for 40 min, 70 min – increasing temperature to 400 °C, and hold at 400 °C for 240 min, then back to 25 °C in 100 min. The iron precursors used to prepare bifunctional catalysts were ferric acetate basic pure, ferric nitrate nonahydrate, and ferric chloride.

### 2.2.2 Catalyst synthesis methods

Three different methods of iron introduction in the zeolitic supports were studied:

- Conventional impregnation: In wet impregnation, an excess of the solution containing the precursor is contacted with the solid support to deposit the precursor on the support. The imbibed solvent is subsequently removed by drying [79].
- Ion-exchange: The metal ions are deposited into the support by replacing an ion inside the support with the ion of the precursor. This method is called ion-exchange, and an excess precursor solution is taken for the metal deposition. The ions between the support and the solution are exchanged until an equilibrium is established [79].
- Deposition-precipitation: In this method, an alkali solution is added to cause precipitation from the slurry containing the metal precursor and the support [79].

### 2.2.3 Synthesis of Fe-supported bifunctional catalysts

Wet impregnation, ion-exchange, and deposition-precipitation methods were used to study the effect of preparation methods on the synthesized Fe catalysts. The preparation of Fe-modified zeolite consists of the following steps:

- i. Transformation of NH<sub>4</sub>-form of the zeolite to the H-form by step-calcination,
- ii. introduction of Fe to the zeolite through impregnation, ion-exchange, or deposition-precipitation,
- iii. filtration, drying, and step-calcination.

Different amounts of iron precursors were taken depending on the target metal loading and then dissolved in 250 ml of distilled water in the ion-exchange method. The supporting zeolite

was then mixed in the solution and stirred for 24 hours at room temperature. In this step, the H-forms of the zeolite were ion-exchanged with the iron precursor. The resulting product was subsequently washed, dried overnight at 100 °C, and then calcined using a step calcination procedure [80]. During the step calcination, the temperature was increased to 250 °C with a temperature ramp of 4.5 °C/min, and then the temperature was held at 250 °C for 40 minutes. Subsequently, the temperature was increased to 450 °C with a ramp of 5 °C/min, where after the temperature was held at 450 °C for 240 minutes [80]. Hence, with this method, different Fe-loaded zeolites with variable Fe loadings were prepared to be tested in the HDO of isoeugenol.

One non-acidic catalyst Fe/SiO<sub>2</sub> prepared by the solid-state ion-exchange method in another project, was used in the HDO of isoeugenol to study the influence of acidity in the reaction.

The list of catalysts prepared by the ion-exchange method and characterization techniques used can be seen in **Table 5**.

**Table 5:** The catalysts prepared by the ion-exchange method with their characterization methods (loadings of catalysts determined by EDS)

<b>Ion-exchange method</b>				
<b>Number</b>	<b>Catalyst</b> (Loading determined by EDS)	<b>Iron precursor used</b>	<b>SEM</b>	<b>TEM</b>
1	2.5 wt.% Fe/H-Beta-25	Ferric acetate	✓	✓
2	7 wt.% Fe/H-Beta-25	Ferric acetate	✓	✓
3	12.5 wt.% Fe/H-Beta-25	Ferric acetate	✓	✓
4	9 wt.% Fe/H-Beta-38	Ferric acetate	✓	✓
5	5.5 wt.% Fe/H-Y-5.1	Ferric acetate	✓	✓
6	9 wt.% Fe/H-Mor-20	Ferric acetate	✓	✓
7	2 wt.% Fe/H-Beta-38	Ferric nitrate	✓	✓
8	1 wt.% Fe/H-Y-5.1	Ferric nitrate	✓	✓
9	1 wt.% Fe/H-Mor-20	Ferric nitrate	✓	✓
<b>Solid-state ion-exchange</b>				
10	2 wt.% Fe/SiO <sub>2</sub>	Ferric nitrate	✓	✓

In the **conventional evaporation-impregnation method**, iron was loaded on zeolites by using water as a solvent. Catalysts with different supports and different iron loadings were prepared. The iron precursor, solvent (250 ml), and zeolite support mixture were stirred in a rotavapor for 24 h at 60 °C. Subsequently, the mixture was evaporated under vacuum. The synthesized catalysts were dried at 100 °C overnight, and calcined using the same calcination procedure mentioned in the ion-exchange method [81].

In the **deposition-precipitation method**, the proton form of zeolite was mixed with an aqueous solution of iron precursor (500 ml). Then, 22 ml of the aqueous ammonia solution (32%) was taken to increase the pH of the solution to 10. The suspension was stirred for 24 h at room temperature. The synthesized catalyst was filtered, washed with deionized water,

dried overnight at 100 °C, and calcined using the same calcination process as stated above [81].

The list of catalysts prepared by the evaporation-impregnation and the deposition-precipitation methods with the characterization techniques used can be seen in **Table 6**.

**Table 6:** The catalysts prepared by the conventional evaporation-impregnation method, the deposition-precipitation method, and their characterization methods

<b>Evaporation-impregnation method</b>					
<b>Number</b>	<b>Catalyst (Loading determined by EDS)</b>	<b>Nominal loading</b>	<b>Iron precursor used</b>	<b>SEM</b>	<b>TEM</b>
1	12 wt.% Fe/H-Beta-25	15	Ferric acetate	✓	✓
2	12 wt.% Fe/H-Beta-38	15	Ferric acetate	✓	✓
3	15 wt.% Fe/H-Beta-300	15	Ferric acetate	✓	✓
4	8 wt.% Fe/H-Y-5.1	11	Ferric acetate	✓	✓
5	7.5 wt.% Fe/H-Beta-25	12	Ferric nitrate	✓	✓
6	9 wt.% Fe/H-Beta-38	12	Ferric nitrate	✓	✓
7	10 wt.% Fe/H-Beta-300	12	Ferric nitrate	✓	✓
8	9.5 wt.% Fe/H-Beta-25	12	Ferric chloride	✓	✓
9	9.5 wt.% Fe/H-Beta-38	12	Ferric chloride	✓	✓
10	10 wt.% Fe/H-Beta-300	12	Ferric chloride	✓	✓
<b>Deposition-precipitation method</b>					
11	12 wt.% Fe/H-Beta-25	15	Ferric acetate	✓	✓

## 2.2.4 Synthesis of Fe, Ni, and Fe-Ni supported bifunctional catalysts on H-Y-5.1

A set of Fe, Ni, and Fe-Ni supported bifunctional catalysts on H-Y-5.1 zeolitic support were prepared by Dr. Irina Simakova from Boreskov Institute of Catalysis (BIC) Novosibirsk, Russia. The single metal catalysts (Fe and Ni) with 5 wt.% nominal metal loading were prepared by the incipient wetness impregnation method with an aqueous solution of the corresponding nitrate precursor, Ni (NO<sub>3</sub>)<sub>2</sub>·6H<sub>2</sub>O or Fe (NO<sub>3</sub>)<sub>3</sub>·9H<sub>2</sub>O, respectively. The bimetallic Ni-Fe catalyst containing 5 wt.% loading of each metal was prepared by subsequent impregnation of the H-Y-5.1 zeolite with the corresponding iron nitrate and nickel nitrate aqueous solutions and a drying step (100 °C overnight) in the middle. Thereafter, the single-metallic and bimetallic samples were dried at 100 °C overnight and calcined at 450 °C for 6 h with a temperature ramp of 2 K/min. The decomposition of nickel and iron nitrates was controlled in the calcination step by measuring the pH of the outgoing gases. The synthesized catalysts were activated in the flow of molecular hydrogen using the corresponding TPR profile before the catalytic runs (see **Table 8**).

**Table 7:** The performed characterizations for Ni, Fe, and Ni-Fe/H-Y-5.1 catalysts

Number	Catalyst (Loading expressed as nominal loading)	Iron precursor used	SEM	TEM
1	5 wt.% Fe/H-Y-5.1	Ferric nitrate	✓	✓
2	5 wt.% Ni/H-Y-5.1	Ferric nitrate	✓	✓
3	5 wt.% Fe - 5 wt.% Ni/H-Y-5.1	Ferric nitrate	✓	✓

## 2.2.5 Reduction procedures

Some of the prepared catalysts were used in the HDO of isoeugenol without reduction. Only four of the synthesized catalysts were reduced before the reaction. The same reduction program was used for the reduction of all four catalysts. The catalysts were sieved to < 63  $\mu\text{m}$  before ex-situ reduction in Microtrac Belcat II equipment under hydrogen (AGA, 99.999%) flow. The amount of catalyst taken for reduction was 100 mg. Pretreatment of the sample under 30 ml/min of argon flow was done in the same equipment before the actual reduction program. In the pretreatment, the sample was heated to 200  $^{\circ}\text{C}$  with a temperature ramp rate of 5  $^{\circ}\text{C}/\text{min}$ , and then the temperature was held at 200  $^{\circ}\text{C}$  for 120 minutes. After the pretreatment, the temperature was decreased to 50  $^{\circ}\text{C}$  before the actual reduction program.

**Table 8:** Reduction program used for the ex-situ reduction of catalysts before experiments

Catalyst	Ex-situ reduction program
5 wt.% Ni/H-Y-5.1	1. Heat from 50 $^{\circ}\text{C}$ to 250 $^{\circ}\text{C}$ at 2 $^{\circ}\text{C}/\text{min}$
5 wt.% Fe/H-Y-5.1	2. Hold at 250 $^{\circ}\text{C}$ for 120 minutes
5 wt.% Fe - 5 wt. % Ni/H-Y-5.1	3. Heat from 250 $^{\circ}\text{C}$ to 500 $^{\circ}\text{C}$ at 2 $^{\circ}\text{C}/\text{min}$
9.5 wt.% Fe/H-Beta-38- $\text{FeCl}_3$	4. Hold at 500 $^{\circ}\text{C}$ for 120 minutes
	5. Decrease the temperature to 150 $^{\circ}\text{C}$
	6. Decrease the temperature further to 35 $^{\circ}\text{C}$

Steps 1–5 were performed under 30 ml/min of hydrogen flow, and step 6 was conducted under 30 ml/min of argon flow.

After the temperature reached 35  $^{\circ}\text{C}$ , 10 ml of solvent (hexadecane) was added to the catalyst and kept overnight.

## 2.3 Batch reactor set-up, analyses of the reaction products, and catalyst characterization

All the HDO experiments were performed in a 300 ml batch reactor (PARR instruments). The reactor was equipped with a mechanical stirrer used at 900 rpm to eliminate mass-transfer limitations. The samples were taken from the sampling lines, removing some drops as waste

before taking the samples. The heating was performed with a heating mantle at 10 °C/min rate until the desired temperature.

In all the experiments, isoeugenol and hexadecane were used as the reactant and the solvent, respectively. All the catalyst screening experiments were conducted at 300 °C for 3 hours and 30 bars of H<sub>2</sub> pressure. 100 ml of hexadecane, 100 mg of the catalyst, and 200 mg of isoeugenol were taken for the experiments. The reactor was flushed with high-purity argon three times followed by high-purity hydrogen three times. Then, the reactor was charged with 15 bars of hydrogen at room temperature, and the heating procedure was started. When the temperature reached 290 °C, the pressure inside the reactor was increased to 30 bars. After the experiments, the reactor was cooled to ambient temperature and depressurized. Five samples were taken in total at times 0, 1 min, 60 mins, 120 mins, and 180 mins, which were analyzed by GC. No gas samples were taken.

The experiments involving Fe, Ni, and Fe-Ni supported on H-Y-5.1 prepared by the same method were conducted at 300 °C for 4 hours and 30 bars of H<sub>2</sub> pressure. Seven samples were taken in total at times 0, 1 min, 30 mins, 60 mins, 120 mins, 180 mins, and 240 mins, which were analyzed by GC. One 5 ml gas sample was taken for the reaction conducted with Fe-Ni bimetallic catalyst when the reactor was cooled to 40 °C to study the gas phase in GC-FID.

### 2.3.1 Analysis of the reaction mixture

The GC analysis for the liquid phase was performed using a DB-1 capillary column (Agilent 122–103e) with 30 m in length, 250 µm internal diameter, and 0.5 µm film thickness. The carrier gas used was helium with a flowrate of 1.7 ml/min. The following temperature program was used: Hold at 60 °C for 5 minutes followed by heating with a temperature ramp of 3 °C/min until 135 °C. Then a ramp of 15 °C/min was applied until 300 °C. The same column and the same temperature program were used for the GC-MS analysis.

**Table 9:** GC retention times of compounds present in the liquid phase in the HDO of isoeugenol

Compound	Retention time (min)
pentane	1.7
hexane	2.1
cyclohexane	2.62
heptane	3.1
methylcyclohexane	3.44
1,4-dimethylcyclohexane	4.63
octane	5.25
1,3,5-trimethylcyclohexane	6.29
1,2,4-trimethylcyclohexane	8.012
1-ethyl-3-methylcyclohexane	8.476

1-ethyl-4-methylcyclohexane	8.577
propylcyclohexane	10.357
butylcyclopentane	10.546
propylbenzene	11.04
1-ethyl-2-methylbenzene	11.447
1-propylcyclohexene	11.619
1,4-diethylcyclohexane	12.032
1,2,3-trimethylbenzene	13.027
1-methyl-3-propylcyclohexane	13.155
decane	14.2
undecane	19.4
dodecane	24.5
4-propylphenol	26.21
tridecane	29.4
dihydroeugenol	31.0
isoeugenol-trans	32.1
1,2-dimethoxy-4-propylbenzene	32.11
tetradecane	32.6
isoeugenol-cis	33.1
pentadecane	34.5
hexadecane	35.8

The gas sample taken was analyzed using an Agilent 6890N-GC apparatus with a GC-Q capillary column having: 30 m x 530  $\mu\text{m}$  x 40  $\mu\text{m}$  dimensions. FID at 300 °C was used to detect light hydrocarbons at 300 °C, and TCD was used to identify gases containing oxygen at 250 °C. The following temperature program was used: Hold 8 minutes at 35 °C followed by heating with a temperature ramp of 20 °C/min to 230 °C. The temperature was kept constant at 230 °C for 30 minutes.

### 2.3.2 Catalyst characterization methods

#### **Scanning Electron Microscopy and Energy Dispersive X-rays Spectroscopy (SEM-EDS):**

Crystal morphology of the prepared catalysts was studied by SEM, and the elemental compositions were determined by EDX. SEM measurements were performed with a Zeiss Leo Gemini 1530 Scanning Electron Microscope with a Thermo Scientific UltraDry Silicon Drift Detector (SDD) [82]. An acceleration voltage of 15 kV was used for the X-ray analyzer.

**Transmission Electron Microscopy (TEM):** The metal particle size, textural properties, porosity, and periodicity of pores of catalysts were studied by Jeol JEM-1400Plus with 120 kV acceleration voltage and resolution of 0.38 nm equipped with Osis Quemesa 11 Mpix bottom-mounted digital camera [82]. Most of the Fe-based catalysts were not reduced before the TEM measurements. The set of monometallic and bimetallic catalysts synthesized on H-Y-5.1

zeolite were reduced using the same reduction program as before the catalytic experiments. The particle size distributions of the catalysts were determined by ImageJ software.

**Temperature Programmed Reduction (TPR):** TPR measurements were performed in Microtrac Belcat II equipment. In a typical experiment, ca. 0.25 g of the catalyst sample was taken, followed by pre-treatment at 200 °C for 2 hours and cooling to 50 °C. Thereafter, the sample was heated to 800 °C with a ramp of 5 °C /min under 1.5 ml/min of hydrogen and 28.5 ml/min of argon (5 vol.% hydrogen and 95 vol.% argon). When reduction of the sample took place, hydrogen was consumed, which was recorded by a thermal conductivity detector (TCD).

**Nitrogen physisorption:** The surface area measurements were performed by Micromeritics 3Flex-3500. The degassing of the sample was performed before pre-treatment of the sample. First, a burette was degassed under vacuum for 2 minutes, and the weight of the empty degassed burette was measured. For sample degassing, ca. 0.25 g of the catalyst was heated overnight in the same burette at 200 °C under vacuum. The weight of the degassed sample was measured the following morning. In this step, the moisture from the catalyst was removed. Next, the sample was subjected to pre-treatment at 250 °C for 4 hours in the physisorption equipment. After this step, adsorption isotherms at -196 °C were recorded, and the moles of nitrogen adsorbed on the sample at different relative pressures were plotted. The specific surface areas of the synthesized microporous materials were calculated using the Dubinin-Radushkevich method. The micropore and mesopore volumes were obtained by the DFT method.

**Fourier-transform infrared (FTIR) spectroscopy:** The qualitative and quantitative determination of both Brønsted and Lewis acid sites of the catalyst were performed by ATI Mattson FTIR using pyridine as a probe molecule. A thin self-supporting pellet of the catalyst of the size of 10–20 mg and radius 0.65 cm was prepared and placed inside the FTIR cell. Under vacuum, the cell temperature was increased to 450 °C for pretreatment and kept there for 1 hour. After that, the temperature was decreased to 100 °C, and the background spectrum of a sample was recorded. The probe molecule (pyridine) was adsorbed at 100 °C for 30 mins and then desorbed by evacuation at different temperatures. Three different desorption temperatures, defined as 250 °C–350 °C as weak, medium, and strong sites, 350 °C–450 °C as medium, and strong sites, and pyridine not desorbed even at 450 °C as strong sites [83]. The spectra of the sample were recorded at every temperature ramp. Scanning was performed under vacuum at 100 °C, and spectral bands at 1545 cm<sup>-1</sup> and 1450 cm<sup>-1</sup> were used to identify Brønsted and Lewis acid sites, respectively. Quantification of the acid sites was performed using the molar extinction parameters reported by Emeis [84]. The weight of the catalyst was taken into account in the calculations.

**X-Ray Diffraction (XRD):** The phase purity and crystal phase identification of a set of Ni, Fe, and Fe-Ni catalysts supported on H-Y-5.1 were determined by powder X-ray diffraction (XRD). XRD analysis was conducted for samples pre-reduced ex-situ with the same reduction program used before the catalytic experiments. The Bragg-Brentano focusing configuration was applied. XRD patterns of the samples were recorded on X-ray diffractometer D8 Advance (Bruker, Germany) using CuK $\alpha$  radiation ( $\lambda = 1.5418 \text{ \AA}$ ) and one-dimensional LynxEye detector with an angular range of 2.9° on the 2 $\theta$  scale by scanning in the 2 $\theta$ -angle range from 15° to

70° with a step of 0.05° and acquisition time of 3 s at each point. The sizes of the coherently scattering domains (CSD -  $D_{\text{XRD}}$ ) were determined from the broadening of diffraction peaks. The instrumental broadening of the diffraction lines was taken into account, which was recorded from the diffraction pattern of the international standard  $\alpha\text{-Al}_2\text{O}_3$  (SRM 1976).

The XRD measurements of other Fe-based catalysts were performed by using PANalytical Empyrean diffractometer with five axis goniometer. The incident beam optics consisted of a Bragg-Brentano HD x-ray mirror, fixed 1/4° divergence slit, 10 mm mask, 0.04 rad Soller slit, and 1° anti-scatter slit. The diffracted beam optics consisted of a 7.5 mm divergence slit, 0.04 rad Soller slit, and PIXcel detector array. The used X-ray tube was Empyrean Cu LFF. The X-ray radiation was filtered to include only Cu  $K\alpha_1$  and Cu  $K\alpha_2$  components.

**Mössbauer Spectroscopy:** The samples were characterized using  $^{57}\text{Fe}$  Mössbauer spectroscopy in transmission geometry. The spectra were measured using a 10-month old  $^{57}\text{Co}:\text{Rh}$  source (Ritverc Co. 50 mCi June 2020) at 77 K and 300 K using a maximum Doppler velocity of 11.0 mm/s. The velocity scale of the transducer was linear. The sample was cooled using an Oxford CF506 continuous-flow cryostat with liquid nitrogen for the 77 K measurements. The temperature was controlled using an Oxford Intelligent Temperature Controller ITC 502. All spectra were fitted using a home-written nonlinear least-squares program with the following Mössbauer parameters for the components: the quadrupole coupling constant  $eQV_{zz}$ , relative intensities, isomer shift  $\delta$  relative to  $\alpha\text{-Fe}$ , and internal hyperfine magnetic field  $B$  when present. All components had the same experimental linewidth  $\Gamma$ , but the additional Gaussian broadening for the magnetically-split components was modeled using a width  $\Delta B$  of the field distribution.

### 2.3.3 Formulae and definitions

The conversion in isoeugenol HDO was calculated by:

$$X_t = \frac{C_0 - C_t}{C_0} * 100\% \quad (2)$$

where  $X_t$  is the conversion of isoeugenol at time  $t$ ,  $C_0$  is the initial molar concentration, and  $C_t$  is the molar concentration at time  $t$ .

The sum of liquid phase compounds in GC was calculated by:

$$GCLPA = \frac{GCLPA_t}{GCLPA_0} * 100\% \quad (3)$$

where  $GCLPA_t$  is the sum of liquid-phase reactants and products at time  $t$ , and  $GCLPA_0$  is the sum of liquid-phase reactants and products at the beginning of the reaction (time 0). The

compounds that are not included in the formula are gas-phase products and heavy compounds adsorbed on the catalyst (coke).

Selectivity was calculated by:

$$S_{i,t} = \frac{\text{moles of products } i, t}{\Sigma \text{moles of products, } t} * 100\% \quad (4)$$

where  $S_{i,t}$  is the selectivity to a product  $i$  at time  $t$ .

Hydrodeoxygenation degree was calculated to evaluate the performance of the catalyst in removing oxygen from isoeugenol.

$$HDO = \frac{n_a^0 - n_a^t - \Sigma n_i * m_0}{n_a^0 - n_a^t} * 100\% \quad (5)$$

where  $n_a^0$  is the initial number of moles of reactant  $a$

$n_a^t$  is the number of moles of reactant  $a$  at time  $t$

$n_i$  is the number of moles of product  $i$  in the liquid phase

$m_0$  is the number of oxygen atoms in the product  $i$

### 3 Results and Discussion

#### 3.1 Catalyst characterization results

##### 3.1.1 Scanning Electron Microscopy and Energy Dispersive X-rays Spectroscopy (SEM-EDS)

SEM was used to study the morphological features such as shape, size, and crystal distributions of Fe- and Ni-modified catalysts. EDS was used to measure the chemical compositions of the pristine H-Y-5.1, H-Beta-38, H-Beta-25, H-Beta-300, and H-Mordenite zeolites along with their Fe-modified counterparts. The set of monometallic and bimetallic catalysts on H-Y-5.1 was denoted through as nominal loadings as their elemental compositions could not be measured by EDS. SEM micrographs of all catalysts exhibit well-defined crystallites which have retained their structures after introduction of Fe. SEM micrographs and crystal size distributions of the fresh and spent bimetallic Fe-Ni/H-Y-5.1 catalyst are presented in **Figure 8**. SEM micrographs of other catalysts are given in Appendix .

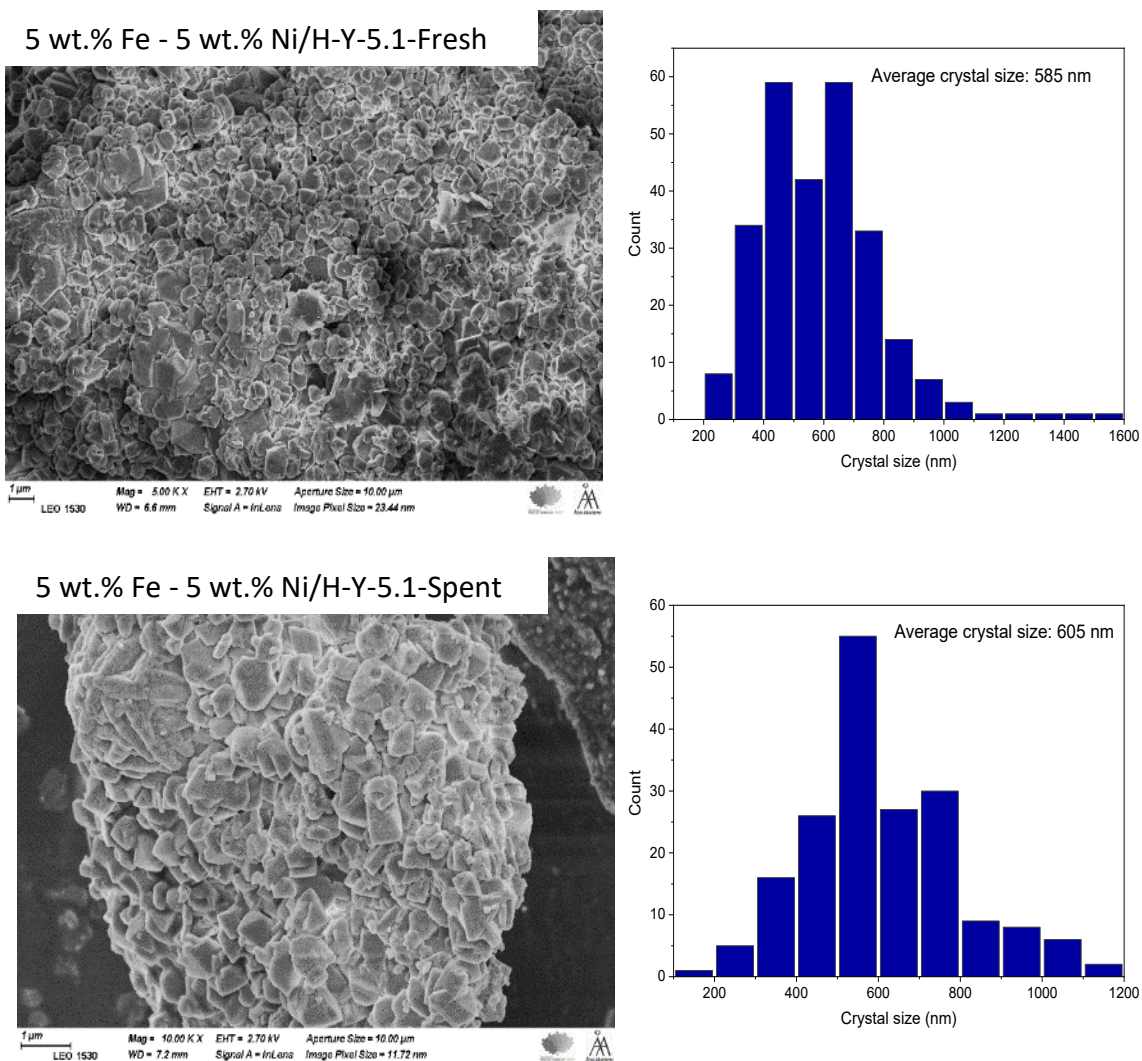


**Figure 8:** SEM micrographs (left) and crystal size distribution (right) of fresh and spent 5 wt.% Fe - 5 wt.% Ni/H-Y-5.1.

SEM micrographs of the metal-modified H-Y zeolites show well-ordered and uniform crystallites. As visible from **Figure 8**, the support of the bimetallic catalyst was kept intact during four hours of the HDO reaction, as the average crystal size and shapes are identical. Similar micrographs with intact structures were obtained for the Fe/H-Y-5.1 and Ni/H-Y-5.1 monometallic catalysts (**Figures S2, S3**). Furthermore, it was observed from the SEM micrographs that the structures of the parent zeolite, silica, and alumina supports were kept intact after metal modifications (Fe, Ni) for all the catalysts. Hence, it can be concluded that the methods of metal incorporation applied in the current work, such as ion-exchange, evaporation-impregnation, and deposition-precipitation, did not influence the morphological features of the parent supports.

### 3.1.2 Transmission Electron Microscopy (TEM)

Fe and Ni metal nanoparticle sizes were measured using TEM. TEM images and histograms of some of the catalysts tested in the HDO of isoeugenol are presented in **Figure 9** and **Figure 10**. The average size of Fe and Ni metal nanoparticles was measured from the plotted histograms. TEM images of other catalysts are shown in Appendix III.

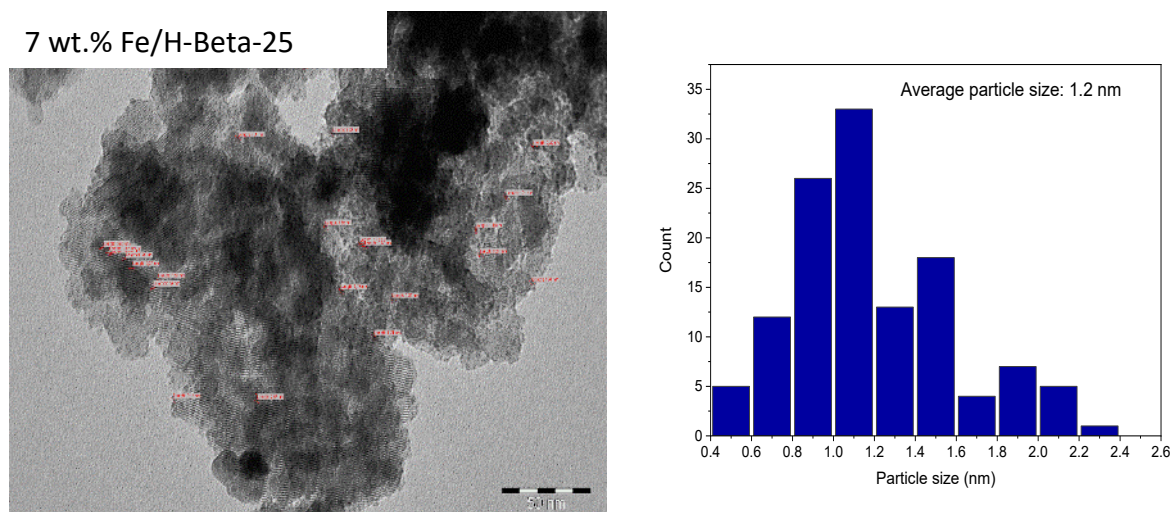


**Figure 9:** TEM micrograph (left) and the particle size distribution (right) of 7 wt.% Fe/H-Beta-25 prepared with the ferric acetate precursor.

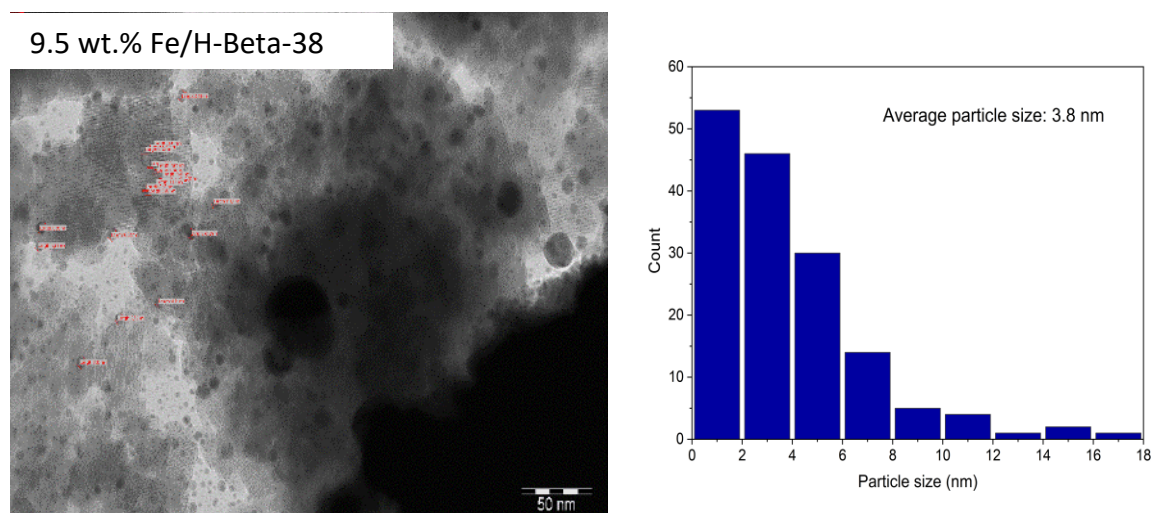


**Figure 10:** TEM micrograph (left) and the Fe particle size distribution (right) of 9.5 wt.% Fe/H-Beta-38 prepared with the ferric chloride precursor.

TEM micrographs of Fe-based catalysts prepared using both ferric acetate and ferric nitrate as precursors showed the presence of highly dispersed Fe nanoparticles with particle sizes in the range of 0.5–2 nm, whereas slightly larger Fe particles were found in the catalysts prepared with ferric chloride. The average Fe particle sizes of some of the synthesized Fe-based catalysts on Beta zeolites as a support are shown in **Table 10**:

**Table 10:** Average metal particle size of some Fe-Beta catalysts determined by TEM

Number	Catalyst	Iron precursor used	Average particle size (nm)
1	2.5 wt.% Fe/H-Beta-25	Ferric acetate	1
2	7 wt.% Fe/H-Beta-25	Ferric acetate	1.2
3	12.5 wt.% Fe/H-Beta-25	Ferric acetate	1.2
4	2 wt.% Fe/H-Beta-38	Ferric nitrate	1.3
5	7.5 wt.% Fe/H-Beta-25	Ferric nitrate	1
6	9.5 wt.% Fe/H-Beta-38	Ferric chloride	3.8

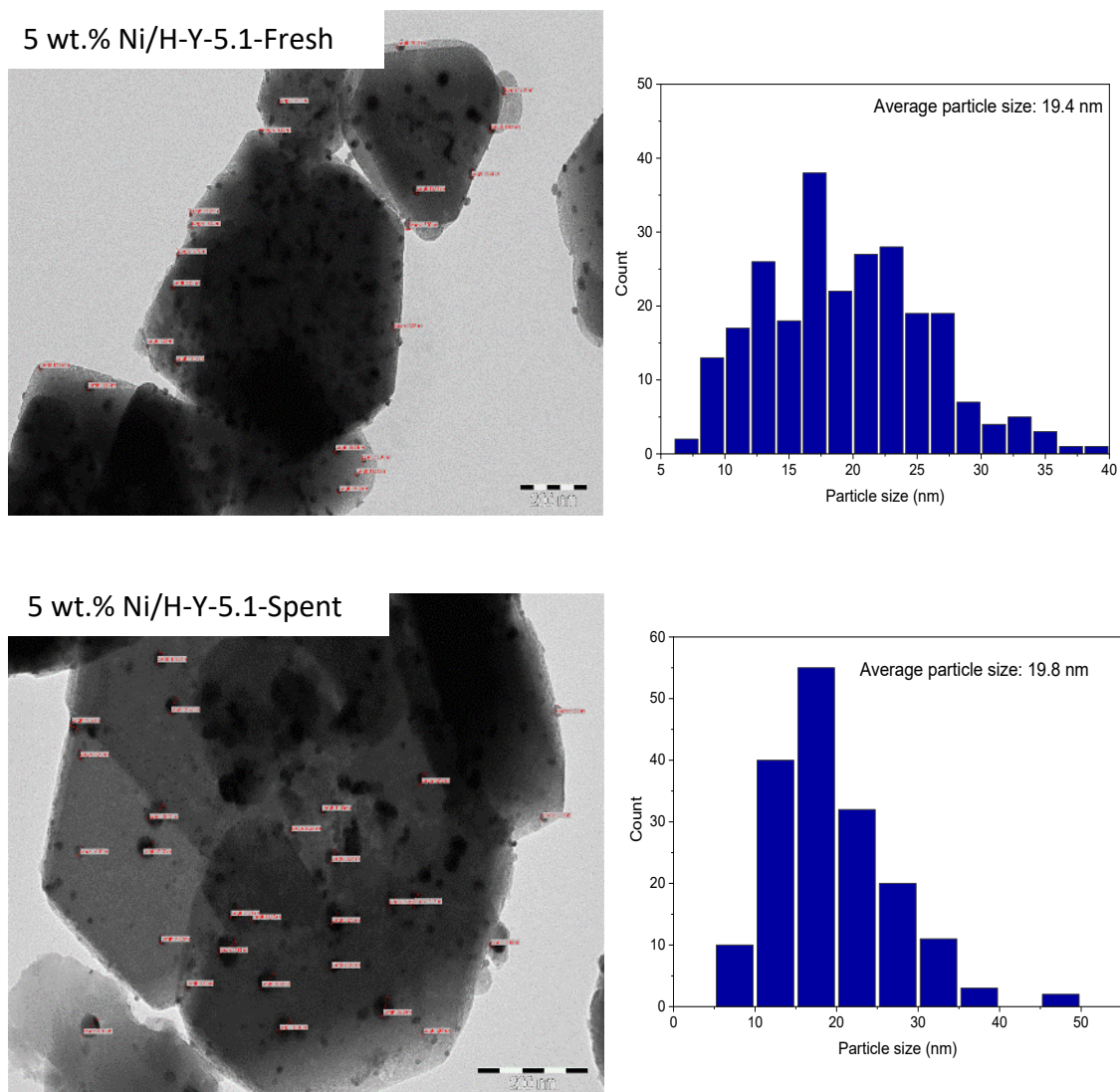


**Figure 11:** TEM micrographs (left) and particle size distributions (right) of the fresh and the spent 5 wt.% Ni/H-Y-5.1.

The TEM micrographs of Ni/H-Y-5.1 showed well-dispersed nanoparticles in the range of 5–50 nm with an average Ni particle size of 20 nm (**Figure 11**). The average particle size of fresh and spent Fe, Ni, and Fe-Ni catalysts synthesized on the H-Y-5.1 support was almost identical. This confirms that there was no sintering of Ni and Fe nanoparticles during the HDO reaction. TEM micrographs and particle size distribution of 5 wt.% Fe - 5 wt.% Ni/H-Y-5.1 showed that

the average nanoparticle size of Ni decreased with the addition of Fe, as the average nanoparticle of this bimetallic catalyst was 8 nm smaller than in the monometallic nickel catalyst. The particle size distribution of this Fe-Ni bimetallic catalyst was in the range of 1–25 nm (**Figure 12**). The metal nanoparticles dispersion was improved, and the particle size distribution was also decreased by the addition of Fe to monometallic Ni/H-Y-5.1. This might be due to the geometric and stabilizing effect which occurs because of the interactions between these two metals [42]. It was found that addition of the second metal as a promoter enhances stability, geometry, and dispersion of the active metallic sites by preventing sintering of the metal during the catalyst preparation or the reaction [77]. However, Ni and Fe nanoparticles could not be distinguished in these micrographs. TEM micrographs of 5 wt.% Fe/H-Y-5.1 show highly dispersed Fe nanoparticles with an average Fe particle size of 6 nm (**Figure 13**). Yang et al. obtained similar results in their TEM micrographs of 8 wt.% Fe/H-Y-9. In [48], highly dispersed Fe<sub>2</sub>O<sub>3</sub> nanoparticles were present on the surface of zeolite Y, having an average size of 5 nm without any obvious bulk Fe<sub>2</sub>O<sub>3</sub> particles [48].

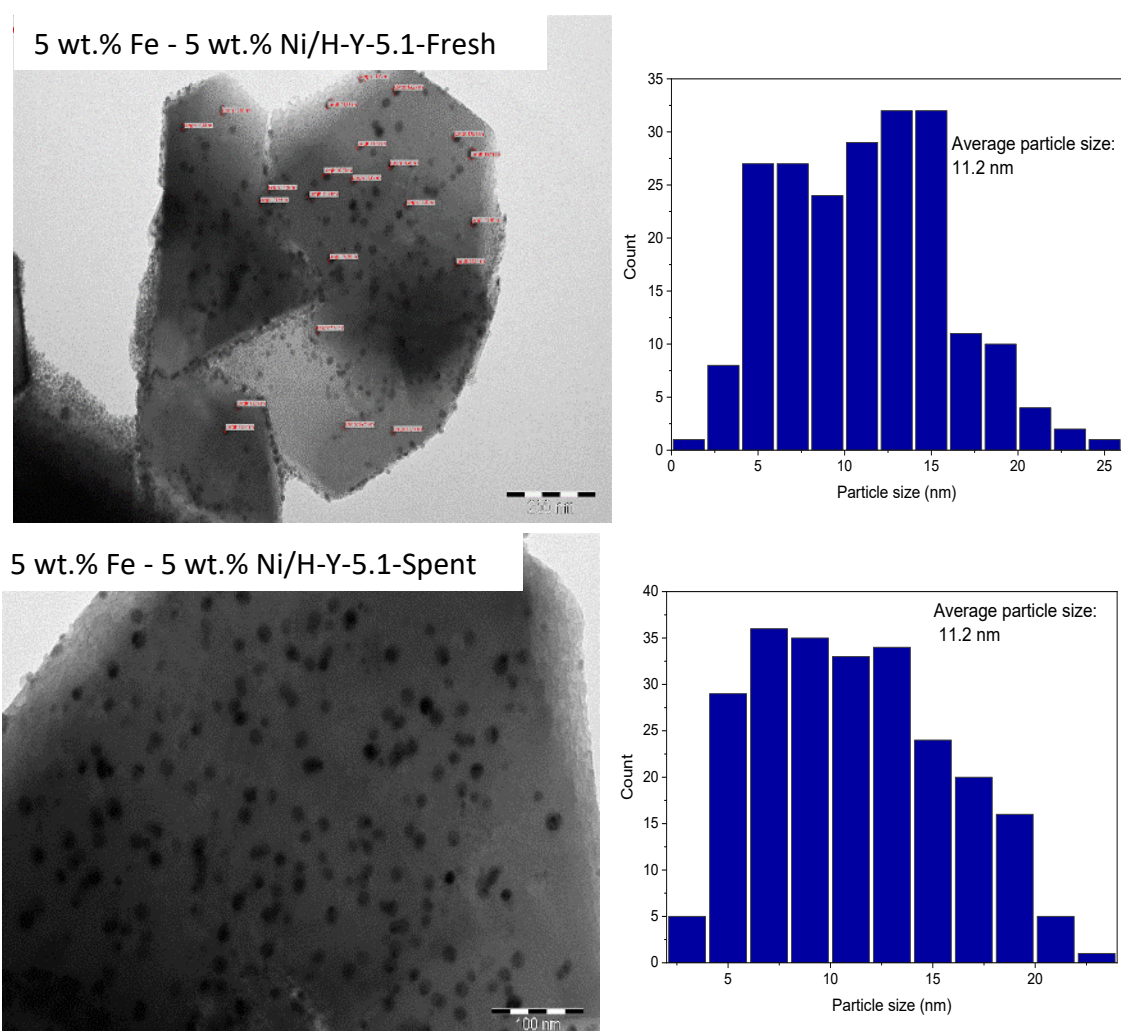
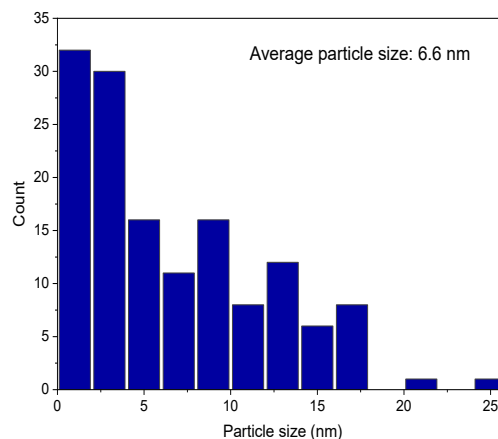
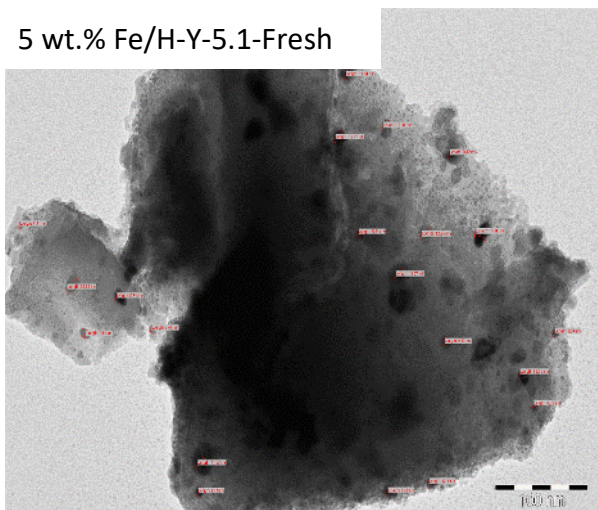


**Figure 12:** TEM micrographs (left) and particle size distributions (right) of fresh and spent 5 wt.% Fe - 5 wt.% Ni/H-Y-5.1.

5 wt.% Fe/H-Y-5.1-Fresh



5 wt.% Fe/H-Y-5.1-Spent

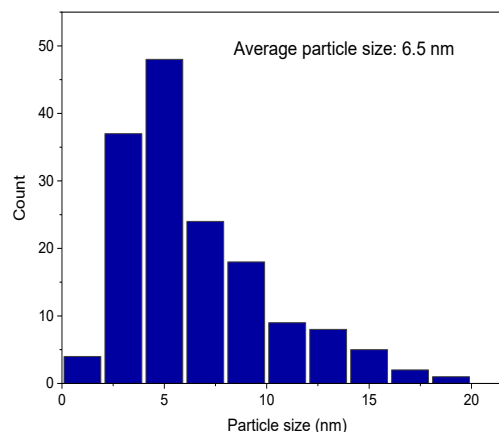
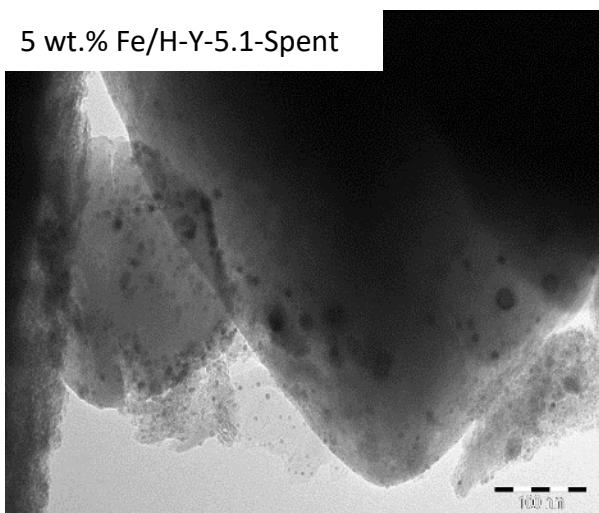


**Figure 13:** TEM micrographs (left) and particle size distributions (right) of fresh and spent 5 wt.% Fe/H-Y-5.1.

### 3.1.3 Temperature Programmed Reduction (TPR)

Reducibility of Fe species with hydrogen in the synthesized Fe-modified zeolites was studied using H<sub>2</sub>-TPR. It is well known that the reduction of hematite (Fe<sub>2</sub>O<sub>3</sub>), the oxide of iron with the highest oxygen content, to metallic iron takes place in stages. If the temperature lower than 570 °C is used, reduction of hematite to magnetite (Fe<sub>3</sub>O<sub>4</sub>) and then to metallic Fe occurs. When a reduction temperature is above 570 °C, an intermediate oxide called wüstite (Fe<sub>(1-x)</sub>O) must be considered, which is stable at these temperatures. The reduction pathway in this instance is hematite → magnetite → wüstite → metallic Fe [86], namely:

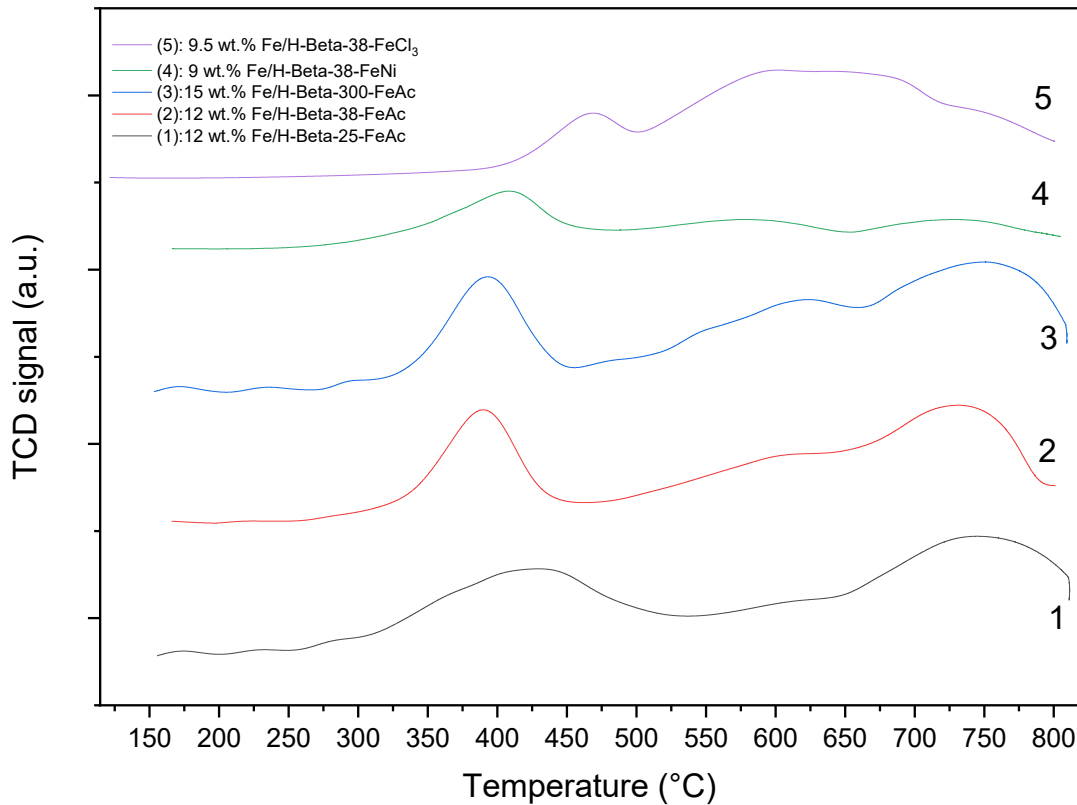
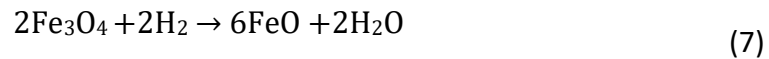
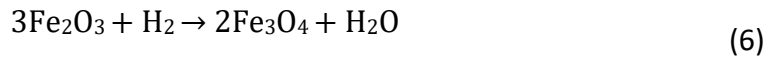


**Figure 14:** H<sub>2</sub>-TPR profiles of some Fe-modified Beta catalysts. Catalyst 1 is prepared with the deposition-precipitation method, and the rest of the catalysts are synthesized with the evaporation-impregnation method.

No clear reduction peak is observed for the H-Beta zeolites before the introduction of Fe [87]. From the TPR profiles, it can be concluded that the TPR profiles of the Fe catalysts prepared with different precursors show different reduction temperatures (see **Figure 14** and **Table 11**). All the catalysts show the reduction behavior typical for hematite ( $\alpha$ -Fe<sub>2</sub>O<sub>3</sub>) [88], which is in line with the XRD results (see section 3.1.6). The first reduction peak for all catalysts appears in the range of ~320-500 °C, with the peak for the catalyst prepared with the chloride precursor (no. 5 in **Figure 14**) coming the farthest. Catalysts 1, 2, and 3, synthesized using the ferric acetate precursor, have the first reduction peak centered at 420 °C, 390 °C, and 390 °C, respectively. An increase in the reduction temperature for catalyst 1 might be a different preparation method (deposition-precipitation) compared to catalysts 2 and 3 (evaporation-impregnation).

The first reduction peak for catalysts 4 and 5 was centered at 410 °C and 465 °C, respectively, which suggests that reduction of the catalyst prepared from the ferric nitrate precursor is

easier than the one synthesized from the chloride precursor. This can be due to the initiation of ferric nitrate and ferric acetate decomposition at a lower temperature of ca. 300 °C to form hematite, compared to ca. 320 °C or higher for ferric chloride [89–91]. Yan et al. [89] have stated that a lower temperature of the metal salt precursor decomposition leads to a better metal dispersion. This is in agreement with our work, as a better metal dispersion and a lower metal particle size were obtained using ferric acetate and nitrate precursor (see section 3.1.2). The first peak for all catalysts can be attributed to the reduction of Fe<sub>2</sub>O<sub>3</sub> to Fe<sub>3</sub>O<sub>4</sub> [92–94]. The peak around 600 °C and 700 °C can be attributed to the successive reduction of Fe<sub>3</sub>O<sub>4</sub> nanoparticles to FeO and FeO to metallic Fe [93], [95]. The peak close to 800 °C might be the direct reduction of Fe<sup>2+</sup> to metallic Fe upon the collapse of the zeolite framework [96]. Since the reduction temperature above 800 °C was used, the pathway Fe<sub>3</sub>O<sub>4</sub> → wüstite → Fe<sub>1-x</sub>O → Fe<sup>0</sup> also needs to be considered during the reduction process, especially for rapidly heated samples [88]. It is also possible that reduction of Fe in the prepared zeolites proceeds only to FeO because it is a metastable form of iron oxide on the Beta-supported zeolites. Interactions of the metal and the support (Fe-Al<sub>2</sub>O<sub>3</sub>) might further retard reduction of FeO to metallic Fe by stabilizing the FeO phase [56].

**Table 11:** H<sub>2</sub>-TPR results of different Fe-Beta catalysts

Catalyst	T <sub>max</sub> (°C)	Relative area
12 wt.% Fe/H-Beta-25-FeAc	420, 610, 750	2.7
12 wt.% Fe/H-Beta-38-FeAc	390, 610, 740	1.8
15 wt.% Fe/H-Beta-300-FeAc	390, 620, 755	1.8
9 wt.% Fe/H-Beta-38-FeN	410, 580, 740	1
9.5 wt.% Fe/H-Beta-38-FeCl <sub>3</sub>	465, 620, 760	2.2

The catalyst prepared with the iron chloride precursor exhibited the peaks for the reduction of isolated Fe<sup>3+</sup> to Fe<sup>2+</sup> (the first peak) and Fe<sub>x</sub>O<sub>y</sub> clusters (the second peak) [97]. The catalysts prepared from the ferric nitrate precursor showed considerably small peaks in the 600–800 °C, contrary to those prepared from other precursors. This might suggest that the catalyst prepared from the ferric nitrate precursor might be difficult to be reduced to metallic Fe.

The TPR results indicate that iron oxide formed in the catalysts cannot be reduced entirely under 400 °C. A typical hematite curve consists of two peaks with a low-temperature peak approximately covering 13% of the total TPR surface area [88,98]. The results from the obtained TPR profiles indicate that the hematite of the samples was not completely converted into Fe<sup>0</sup> during the reduction process.

The TPR of monometallic and bimetallic catalysts synthesized on H-Y-5.1 support (**Figure 15**) was performed to illustrate reducibility of these catalysts and to study interactions between Ni and Fe nanoparticles. The TPR profile of Fe/H-Y-5.1 exhibits a broad reduction curve in the range of 275 °C–500 °C with a peak temperature of 395 °C, which corresponds to reduction of Fe(III) to Fe(II) [99]. In this case, ferric nitrate was used as a precursor, and T<sub>max</sub> was lower than for the catalyst prepared from the ferric chloride precursor. The TPR curves indicate further a small hydrogen consumption at the temperature above 500 °C. The TPR profiles

indicate that from nitrate, only some Fe(II) species were converted into metallic Fe during the reduction process. Nováková et al. have shown that the amount of metallic Fe on HY zeolites after the reduction with hydrogen at 545 °C does not exceed 10% in the surface layers [100].

**Table 12:** H<sub>2</sub>-TPR results of monometallic and bimetallic catalysts synthesized on H-Y-5.1 support

Catalyst	T <sub>max</sub> (°C)	Relative area
5 wt.% Fe/H-Y-5.1	395, 525, 700	1
5 wt.% Ni/H-Y-5.1	375, 500, 625	2.6
5 wt.% Fe - 5 wt.% Ni/H-Y-5.1	395, 470, 625	4.6

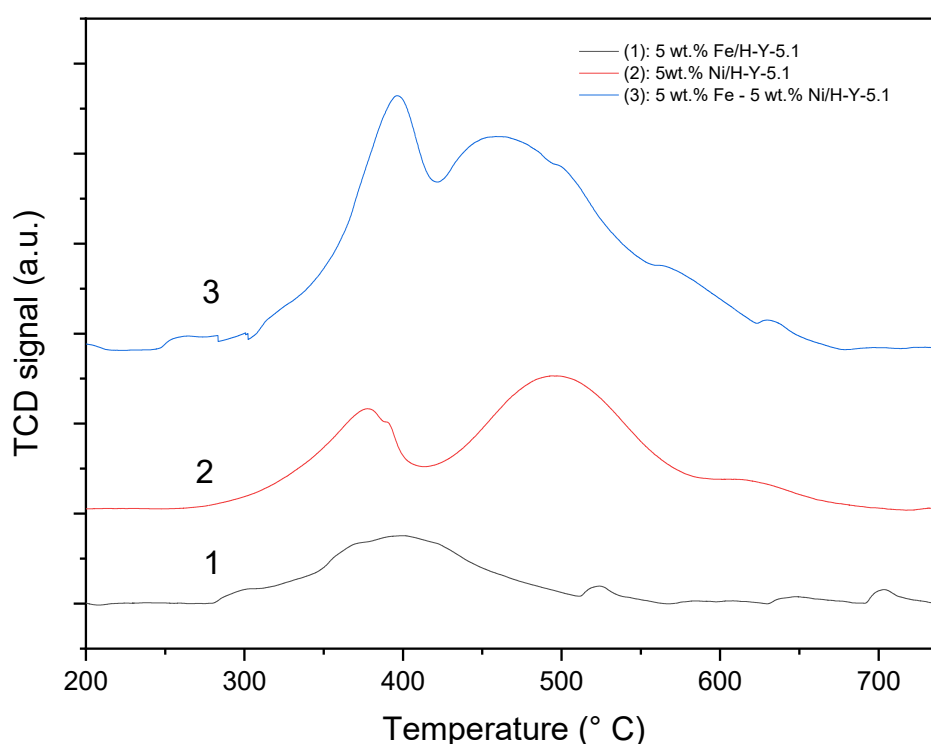


**Figure 15:** H<sub>2</sub>-TPR profiles of Fe/H-Y-5.1, Ni/H-Y-5.1, and Fe-Ni/H-Y-5.1.

The TPR profile of Ni/H-Y-5.1 shows three reduction peaks with the maximum temperatures at 375 °C and 500 °C, and 625 °C, respectively. The 1<sup>st</sup> reduction peak can be attributed to the reduction of free NiO crystallites, while the 2<sup>nd</sup> prominent peak and the 3<sup>rd</sup> small shoulder peak can be ascribed to the reduction of other Ni-species having stronger interactions with the support [101]. It could be due to the reduction of nickel aluminate or nickel silicate species. It is possible that the aluminum in the sample is located outside of the framework and reacts with NiO to form nickel aluminate (NiAl<sub>2</sub>O<sub>4</sub>) [56]. According to Misi et al. and Cheng et al. [56,102] the NiO phase is reducible below 500 °C and the nickel aluminate is reduced above 500 °C or 600°C, depending upon the zeolite support used. The 2<sup>nd</sup> peak is almost 1.9 times the 1<sup>st</sup> peak, suggesting that more nickel in the catalyst is bound to the zeolite. The nickel

zeolite could undergo reduction from Ni<sup>2+</sup> to Ni<sup>+</sup> and then to metallic Ni<sup>0</sup> [103]. The total nickel reduction can be written as:



The TPR profile of Fe-Ni/H-Y-5.1 exhibits two big peaks and one small shoulder peak identical to the profile of Ni catalyst. Interactions between Fe and Ni seem to intensify the peaks significantly. Introduction of Fe leads to an increase of the reduction temperature for NiO from 375 °C to 395 °C, which can be attributed to the interactions between Ni and Fe [54,55]. These interactions might be due to formation of an alloy or an intermetallic compound. The maximum temperature of 2<sup>nd</sup> peak decreased by almost 30 °C compared to the monometallic Ni catalyst.

The peaks in Fe-Ni/H-Y-5.1 illustrate the simultaneous reduction of iron oxide and nickel oxide. As the peaks increased significantly compared to monometallic Ni and Fe catalysts, it can be concluded that Ni promoted the reduction of Fe<sub>2</sub>O<sub>3</sub>. According to the literature, the easy hydrogen dissociation on the pre-reduced Ni sites followed by the spilling of the dissociated hydrogen to the Fe oxide sites can promote the reduction of Fe species [55,104].

According to these profiles, it is evident that the complete reduction of Fe and Ni species occurs only at temperatures above 600 °C. However, reduction at such a high temperature can lead to sintering of active metals and destruction of the zeolite framework. A reduction temperature of 500 °C is a good compromise based on the obtained H<sub>2</sub>-TPR profiles [101].

### 3.1.4 Nitrogen physisorption

The Dubinin-Radushkevich surface areas and DFT pore volumes of 5 wt.% Fe/H-Y-5.1, 5 wt.% Ni/H-Y-5.1, and 5 wt.% Fe - 5 wt.% Ni/H-Y-5.1 catalysts studied using nitrogen physisorption are given in **Table 13**. The surface areas and the pore volumes of Fe- and Ni-modified H-Y-5.1 catalysts are much smaller than the pristine H-Y-5.1 zeolite catalyst, which is around 897 m<sup>2</sup>/g, according to the literature [105]. A decrease in the surface area of more than 30% for these catalysts can be attributed to blockage of the pores of H-Y-5.1 zeolite with a relatively large pore size by Fe and Ni metal nanoparticles. A decrease in the pore volume in the metal impregnated H-Y-5.1 might be because the metallic species occupy some space inside the zeolite pores [43]. As shown in **Figure 16** (left), all zeolites display type I isotherm with an H4-type hysteresis loop indicating the presence of micropores. The pore volume was almost entirely in the micropore range. The pore width of all metal-modified H-Y-5.1 zeolites was similar to the pristine H-Y-5.1, suggesting that the metal-impregnated zeolites retained their structures.

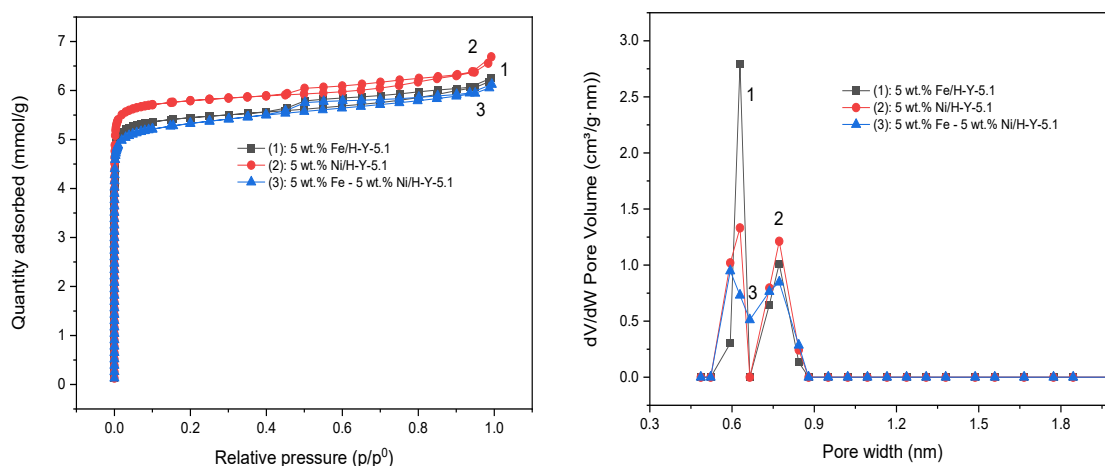


**Figure 16:** N<sub>2</sub> adsorption–desorption isotherms (left) and pore distribution curves (right) of 5 wt.% Fe/H-Y-5.1, 5 wt.% Ni/H-Y-5.1, and 5 wt.% Fe - 5 wt.% Ni/H-Y-5.1

**Table 13:** Textural properties of Ni, Fe, and Ni-Fe/H-Y-5.1 catalysts.

Number	Catalyst	Iron precursor used	Specific surface area (m <sup>2</sup> /g)	Micropore volume (cm <sup>3</sup> /g)	Meso- and macropore volume (cm <sup>3</sup> /g)
1	H-Y-5.1 [106]	–	897	0.32	0.06
2	5 wt.% Fe/H-Y-5.1	Ferric nitrate	555	0.22	0.02
3	5 wt.% Ni/H-Y-5.1	Ferric nitrate	585	0.23	0.02
4	5wt.% Fe - 5 wt. % Ni/H-Y-5.1	Ferric nitrate	540	0.21	0.02

**Table 14:** Textural properties of Fe catalysts prepared with the ion-exchange method

Number	Catalyst	Iron precursor used	Specific surface area (m <sup>2</sup> /g)	Micropore volume (cm <sup>3</sup> /g)	Meso- and macropore volume (cm <sup>3</sup> /g)
1	H-Beta-25 [105]	–	681	0.24	0.45
2	7 wt.% Fe/H-Beta-25	Ferric acetate	474	0.19	0.35
3	12.5 wt.% Fe/H-Beta-25	Ferric acetate	378	0.16	0.30
4	H-Beta-38 [107]	–	827	0.3	n/d
5	9 wt.% Fe/H-Beta-38	Ferric acetate	551	0.23	0.08
6	5.5 wt.% Fe/H-Y-5.1	Ferric acetate	760	0.27	0.13

It can be seen from **Table 15** that the specific surface area decreased with increasing metal loading as expected. The surface area and mesopore volume of Fe/H-Y-5.1 prepared with the ferric acetate precursor were higher than the ones prepared with the ferric nitrate precursor for different preparation methods and higher metal loading.

**Table 15:** Textural properties of Fe catalysts prepared with the evaporation-impregnation method and the deposition-precipitation method

Number	Catalyst	Iron precursor used	Specific surface area (m <sup>2</sup> /g)	Micropore volume (cm <sup>3</sup> /g)	Meso-and macropore volume (cm <sup>3</sup> /g)
1	7.5 wt.% Fe/H-Beta-25	Ferric nitrate	436	0.18	0.32
2	9 wt.% Fe/H-Beta-38	Ferric nitrate	517	0.21	0.09
3	9.5 wt.% Fe/H-Beta-38	Ferric chloride	442	0.19	0.06
4	12 wt.% Fe/H-Beta-38	Ferric acetate	418	0.17	0.10
5	10 wt.% Fe/H-Beta-300	Ferric nitrate	519	0.22	0.04
6	15 wt.% Fe/H-Beta-300	Ferric acetate	386	0.16	0.07
7	8 wt.% Fe/H-Y-5.1	Ferric acetate	750	0.30	0.39
<b>Deposition-precipitation method</b>					
8	12 wt.% Fe/H-Beta-25	Ferric acetate	388	0.15	0.35

### 3.1.5 Fourier-transform infrared (FTIR) spectroscopy

The acidic properties, such as the amount of Brønsted and Lewis acid sites in the metal-modified Fe and Ni heterogeneous catalysts, were determined using the FTIR pyridine adsorption-desorption method (**Table 16**). The results revealed that addition of Fe to H-Beta-25 led to a loss of strong Brønsted and Lewis acid sites of the parent H-Beta-25. Only 12 wt.% Fe/H-Beta-38 exhibited strong acid sites. Deposition of the metal on H-Beta-38 led to the formation of Lewis acid sites at the expense of Brønsted sites, which is in accordance with Suerz et al. [107]. 7 wt.% Fe/H-Beta-25 and 12.5 wt.% Fe/H-Beta-25 both prepared by the ion-exchange method showed similar acid sites, with the former containing slightly more Brønsted sites.

**Table 16:** Acidity measurements of the synthesized Fe-modified catalysts by FTIR

Catalyst	Preparation method	Brønsted acid sites (W, M, S) in $\mu\text{mol/g}$	Lewis acid sites (W, M, S) in $\mu\text{mol/g}$	Total acid sites in $\mu\text{mol/g}$
H-Beta-25 [108]	–	62, 87, 120	34, 15, 113	431
7 wt.% Fe/H-Beta-25	Ion-exchange	91, 108, 0	61, 15, 0	275
12.5 wt.% Fe/H-Beta-25	Ion-exchange	70, 116, 0	63, 20, 0	269
12 wt.% Fe/H-Beta-25	Deposition-precipitation	55, 90, 0	63, 15, 0	223
H-Beta-38 [107]	–	17, 40, 221	19, 9, 2	309
12 wt.% Fe/H-Beta-38	Evaporation-impregnation	40, 50, 29	55, 10, 0	184
H-Beta-300 [108]	–	15, 57, 10	26, 4, 0	112
15 wt.% Fe/H-Beta-300	Evaporation-impregnation	13, 31, 0	23, 19, 0	86
8 wt.% Fe/H-Y-5.1	Evaporation-impregnation	91, 85, 0	21, 7, 0	204

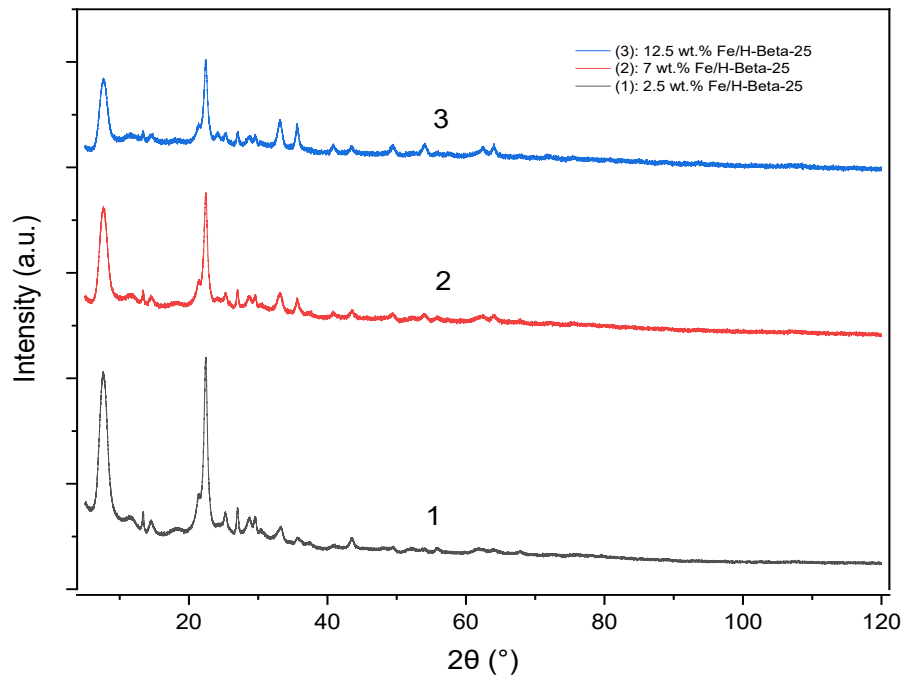
Notation: **W**- weak acid site, **M**-medium acid site, **S**-strong acid site

Acidity of 8 wt.% Fe/H-Y-5.1 was found to be 204  $\mu\text{mol/g}$  comprising weak and medium Brønsted and Lewis acid sites. Acidity of Fe, Ni, and Fe-Ni on H-Y-5.1 support has not been measured in the current work. However, from the literature, it is known that acidity of a zeolite decreases with an increase in the metal loading [43,109]. As the bimetallic Fe-Ni catalyst consists of double the metal loading (10 wt.%) compared to the monometallic Fe and Ni catalysts (5 wt.% each), the bimetallic catalyst should have fewer acid sites than the monometallic counterparts.

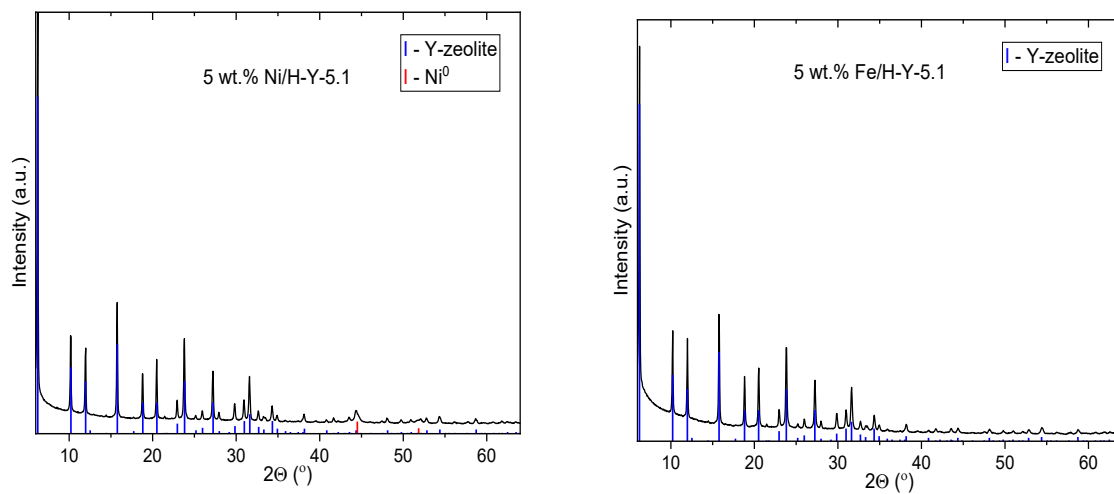
### 3.1.6 X-Ray Diffraction (XRD)

The structural features of the Fe- and Ni-modified zeolite catalysts were measured using X-ray powder diffraction. The XRD patterns of Fe-modified H-Beta-25 catalysts presented in **Figure 17**, clearly show the typical structures of the H-Beta zeolite. However, a gradual decrease in the characteristic Beta peak intensities with an increase in Fe loading can be observed, which might be due to the adverse effect of the Fe loading on these peaks [110], [111]. Sun et al. [111] have stated that the Fe-modifications on ZSM-5 support might decrease the degree of crystallinity of the ZSM-5 support resulting in decreased XRD peak intensities. The XRD patterns also exhibited the presence of the hematite ( $\text{Fe}_2\text{O}_3$ ) phase, with the peaks becoming sharper with an increase in metal loading. The hematite peaks were observed in  $2\theta = 33.3^\circ$ ,  $2\theta = 35.6^\circ$ ,  $2\theta = 49.5^\circ$ , and  $2\theta = 54.1^\circ$ . There might also be possible magnetite ( $\text{Fe}_3\text{O}_4$ ) and Fe phases in the samples. From the TEM measurements, the particle sizes of these

samples were found to be less than 3 nm. These particles are not detected by XRD due to limitations of the instrument, therefore not all possible phases might have been detected.



**Figure 17:** XRD patterns of 2.5 wt.%, 7 wt.%, and 12.5 wt.% H-B-25 prepared by the ion-exchange method with the ferric acetate precursor.



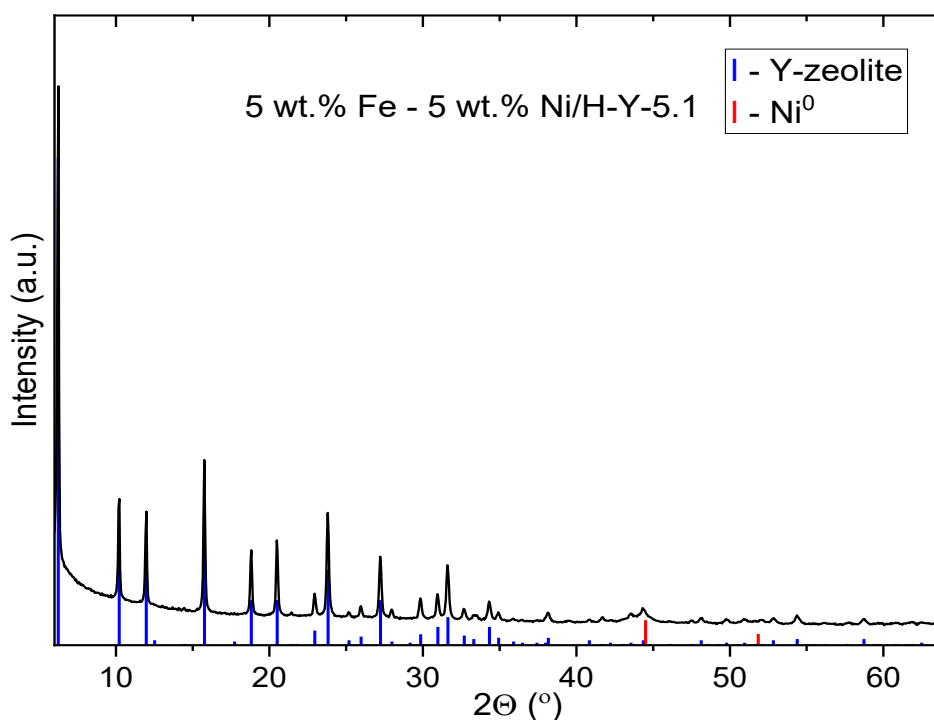


**Figure 18:** XRD images of 5wt.% Ni/H-Y-5.1, 5 wt.% Fe/H-Y-5.1, and 5 wt.% Fe - 5 wt.% Ni/H-Y-5.1.

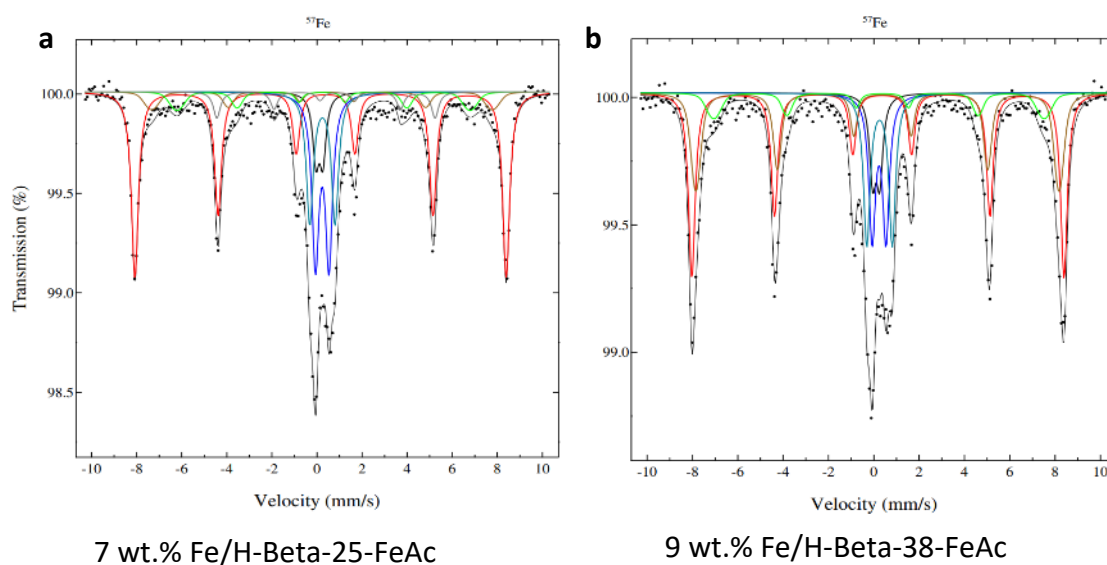
The XRD images of the Fe and Ni catalysts synthesized on H-Y-5.1 support clearly show the typical structure of the Y phase of the zeolite (**Figure 18**) with an average crystal size diameter of more than 100 nm. This is in agreement with the SEM measurements, which showed that the average crystal sizes of these metal-modified zeolites were between 500 and 600 nm (see section 3.1.1). In all synthesized catalysts, the nickel phase was detected at  $2\theta = 44.7^\circ$  and  $2\theta = 51.9^\circ$  which can be attributed to  $\text{Ni}^0$  (1 1 1) and (2 0 0) respectively [51,85]. The crystallized iron-containing phase was not detected by XRD in both monometallic and bimetallic samples synthesized with the H-Y-5.1 support. This might be due to the uniform dispersion of Fe on the Y zeolite without formation of a large-particle crystal structure and an incomplete reduction of Fe oxides at 500 °C [104]. Yang et al. [48] have stated that detecting  $\text{Fe}_2\text{O}_3$  peaks with Fe loading lower than 9% on Y zeolite is difficult because of the small  $\text{Fe}_2\text{O}_3$  nanoparticles formed. Analogous results were obtained by Zhang et al. and Li et al. during Fe-modifications on H-Beta, HY, and H-ZSM-5 zeolites [110,112].

The intensity of diffraction peaks due to the presence of NiO decreased in the bimetallic catalyst compared to the monometallic Ni catalyst. This might be due to a better dispersion of NiO by the addition of Fe oxides, which indicates interactions between Fe and Ni oxides [104]. This result was supported by a decrease in the average metal particle size of the bimetallic catalyst evident from TEM (see section 3.1.2). The average particle sizes of synthesized monometallic and bimetallic catalysts on H-Y-5.1 support, determined by XRD and TEM, are shown in **Table 17**.

**Table 17:** Average particle size determined by TEM and XRD

Number	Catalyst	Iron precursor used	Average metal particle size from TEM (nm)	Average metal particle size from XRD (nm)
1	5 wt.% Fe/H-Y-5.1	Ferric nitrate	6.6	>3
2	5 wt.% Ni/H-Y-5.1	Ferric nitrate	19.4	17
3	5 wt.% Fe - 5 wt. % Ni/H-Y-5.1	Ferric nitrate	11.1	9

### 3.1.7 Mössbauer Spectroscopy

**Figure 19:** Mössbauer spectra of two different Fe-modified zeolites prepared by the ion-exchange method: 7 wt.% Fe/H-Beta-25-FeAc (left) and 9 wt.% Fe/H-Beta-38-FeAc (right).

All six samples (**Figure 19**, **Figures S10**, and **S11**) were fitted with 3 to 4 magnetic sextets (drawn in red, brown, green, and gray), each representing a magnetically ordered iron species. Additionally, two paramagnetic doublets (drawn with blue and turquoise lines) were needed to complete the along with a small fraction of paramagnetic iron (drawn with a black line) in the beryllium window of the detector. The spectra recorded at 300 K are dominated by a red sextet with a substantial quadrupole coupling, seen as a larger distance between lines one and two compared to that between lines five and six. The internal field value of 50–51 T and the isomer shift value of just below 0.4 mm/s for  $\alpha$ -iron indicates that this is a trivalent Fe-species closely related to hematite ( $\text{Fe}_2\text{O}_3$ ), being probably hematite with a small particle size, although not in the nm range. Nanoparticles of (anti)ferromagnetic species do not have an internal field, as they are superparamagnetic at room temperature. It should be pointed out that hematite should undergo the so-called Morin transition (at  $\sim 200$  K), which affects the quadrupole splitting in

such a way that when the distance between lines 1 and 2 is larger than that between the 5<sup>th</sup> and 6<sup>th</sup> lines, the situation is opposite at low temperatures. This is seen for the sample 7.5 wt.% Fe/H-Beta-25-FeN (**Figure S11a**) prepared by the evaporation-impregnation method, confirming presence of hematite in this sample. If the samples do not differ chemically too much it is probably safe to say that all red components are hematite.

The following two sextets in brown and green seem to appear as a pair, i.e., their intensities are more or less locked, with one of them having a field of 46.5–49.5 T and the other 40–45 T. That would suggest a slightly lower oxidation state than 3+ as high-spin Fe<sup>3+</sup> should have a field exceeding 50 T. Magnetite (Fe<sub>3</sub>O<sub>4</sub>) is the most likely candidate exhibiting two Fe species at room temperature: Fe<sup>3+</sup> and valence mixed Fe<sup>2.5+</sup> species. Upon cooling down, the spectrum should undergo a change as the mixed-valence is split into Fe<sup>3+</sup> and Fe<sup>2+</sup>. However, this is seen only in catalysts samples containing pure Fe<sub>2</sub>O<sub>3</sub> or Fe<sub>3</sub>O<sub>4</sub> crystals. Magnetite should generally have a significantly larger isomer shift value than hematite which was not visible in this work. Nevertheless, tentatively the green and brown components are assigned to the magnetite-like compounds.

Additionally, a very weak magnetic component (gray) with a field of 25–30 T is seen in some of the samples (**Figures S10a, S11a, S11b** at room temperature and **Figures 19a, S11a, S11b** at 77 K). It has a high isomer shift value being unambiguously identified as Fe<sup>2+</sup> and accounting only for a few percent of the total Fe content and such component can be an impurity.

The two paramagnetic compounds could be due to hematite and/or magnetite nanoparticles. In principle, they should lose intensity to the magnetic ones upon cooling, and while this perhaps is the case in 12 wt.% Fe/H-Beta-25-FeAc and 9 wt.% Fe/H-Mor-20-FeAc, the effect is generally small. Maybe even lower temperatures should be employed to turn the two paramagnetic ones into regular sextets. Speculating further, it can be stated that there is more hematite than magnetite in the sample, subsequently if this holds also for the assumed superparamagnetic species, then the blue color in the spectra represents hematite, and the turquoise color represents magnetite.

## 3.2 Hydrodeoxygenation of isoeugenol

### 3.2.1 HDO of isoeugenol on Fe-based monometallic catalysts

A blank experiment without any catalyst was performed using isoeugenol as a reactant and hexadecane as a solvent to elucidate the hydrogenation activity at 300 °C and 30 bar total pressure for 3 hours. The same operating parameters used by Lindfors et al. [21] for HDO with Ni catalysts were chosen to compare the obtained results. The mass balance closure requires analysis of the products in the solid, liquid, and gas phases. In this work, however, only the liquid phase has been quantitatively analyzed by GC. Thus, the incomplete mass balance could be due to the strong adsorption of oligomers and coke on the active sites of the catalyst, and formation of gaseous products [18].

As can be observed from **Figure 20**, a complete conversion of isoeugenol was obtained under the used operating conditions without any catalyst. Rapid hydrogenation of isoeugenol to dihydroeugenol already took place in the first minute of the experiment, which has also been reported by Bjelić et al. [113]. The GCLPA decreased sharply in the first minute of the reaction and then stabilized at over 85%. The GCLPA calculations did not include hexane, heptane, octane, and nonane as they were detected in the initial sample, and it was difficult to identify if these compounds formed later in the experiment originated from the solvent or the reactant. While the dihydroeugenol conversion was around 15%, only hexane, heptane, octane, and nonane were seen in the products in the liquid phase as determined by GC-MS. It must be noted that all these compounds were also present as impurities in the solvent. The dihydroeugenol conversion of 15% might be due to formation of the gas-phase products during the blank experiment. The GC equipment error also needs to be considered during the calculations. From this experiment, it was clear that the HDO of the reactant does not occur in the studied conditions without a catalyst. Similar results were obtained by Alda-Onggar et al. [22] at 250 °C and 30 bar total pressure using isoeugenol as the reactant and dodecane as the solvent.

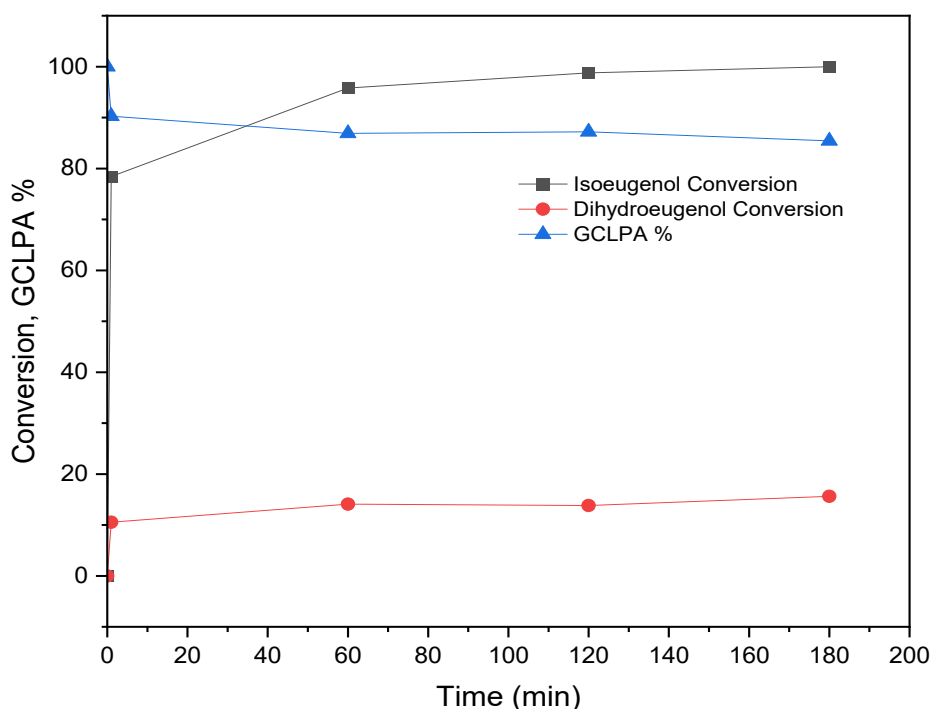


**Figure 20:** Conversion of isoeugenol, dihydroeugenol, and GCLPA % versus time in isoeugenol HDO at 300 °C and 30 bar total pressure in the absence of any catalyst.

In **Figure 21**, cracking of the solvent because of the acidic properties of Fe/H-Beta-38 catalyst can be observed. Such strong cracking activity of Fe/H-Beta-38 compared to other zeolites used in the study might be due to the presence of strong Brønsted acid sites after Fe loading on H-Beta-38, which were absent in other metal-modified zeolites (see **section 3.1.5**). As the cracking products of the solvent and the products of the HDO reaction with isoeugenol coincide, it is difficult to identify the origin of the formed products. Cracking of the solvent in

the absence of the reactant resulted in formation of primarily light hydrocarbons. Most of the small peaks could not be identified by GC-MS.

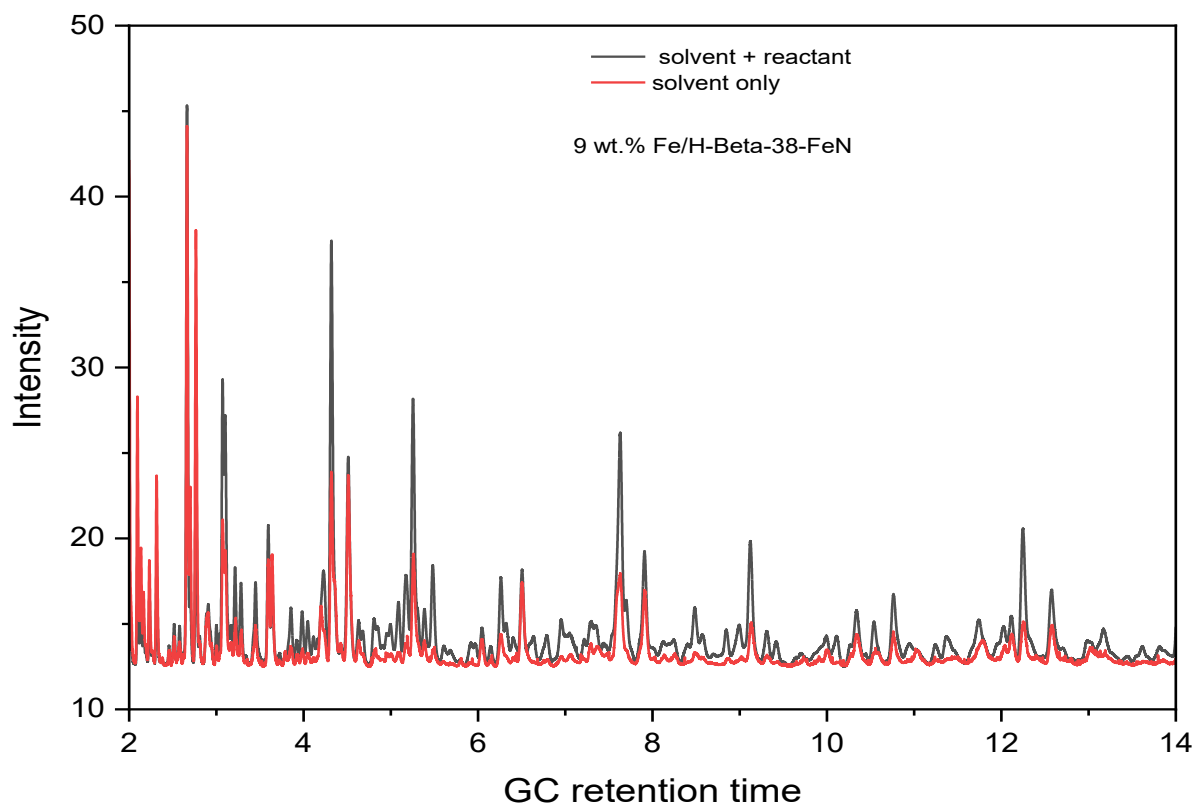


**Figure 21:** GC retention times of the products formed during experiment using an unreduced 9 wt.% Fe/H-Beta-38-FeN with the solvent only (red) and solvent with the reactant (black).

HDO of isoeugenol conducted over different unreduced Fe-modified catalysts yielded dihydroeugenol as the main product (**Appendix V, Table S1**). Activity of these catalysts was poor in the studied conditions, and only cracking products were obtained on catalysts prepared using H-Beta-38 zeolitic support. The results are difficult to be compared with the existing literature because the HDO of isoeugenol over Fe-modified zeolites have not been performed previously. The catalysts did not produce the desired deoxygenated products. The reason for such low activity might be the strong adsorption and retention of phenolic compounds on the acidic sites of Fe/H-Beta. Analogous results were obtained by Sirous-Rezaei et al. [50] in the HDO of guaiacol over Fe/H-Beta-38 catalyst. In their study, the HDO activity of Fe/H-Beta-38 decreased by ca. 87% when the reaction temperature was reduced from 350 °C to 300 °C. They stated that an increase in adsorption energy occurs with a decrease in the reaction temperature because of the exothermic nature of adsorption reactions [47,50]. Therefore, stronger adsorption and retention of phenolics occurs at 300 °C than 350 °C, leading to a lower catalytic activity. The strong adsorption might be due to substantial interactions between hydroxyl groups from phenolic molecules and oxygen atoms linked with the framework aluminum from zeolite, forming phenolate ions [50]. As H-Beta consists of microscopic structure and narrow channels, low diffusivity of bulky phenolic molecules inside the catalytic channels leads to the blockage of pores [50].

Only reduced 9.5 wt.% Fe/H-Beta-38-FeCl<sub>3</sub> displayed slight deoxygenation activity, yielding of 4-propylphenol of c.a. 6% and traces of propylcyclohexane. However, the unreduced 9.5 wt.% Fe/H-Beta-38-FeCl<sub>3</sub> catalyst did not show significant deoxygenation activity. The better catalytic activity of the reduced catalyst might be due to presence of the Fe in the magnetite and metallic Fe phase compared to hematite phase in the unreduced counterparts. Even a non-acidic Fe/SiO<sub>2</sub> catalyst did not exhibit any deoxygenation. Summarizing, Fe-based monometallic catalysts were found to be unsuitable for the HDO of isoeugenol in the used operating conditions. Hence, the decision was taken to apply bimetallic Fe-Ni catalysts which have better activity according to the literature.

### 3.2.2 HDO of isoeugenol on Fe-Ni-based bimetallic catalysts

The HDO of isoeugenol was conducted with a set of catalysts synthesized using the same preparation method on H-Y-5.1 support to study the synergistic effects of Fe and Ni. The set of catalysts prepared for this study consisted of monometallic 5 wt.% Fe/H-Y-5.1 and 5 wt.% Ni/H-Y-5.1, and bimetallic 5 wt.% Fe - 5 wt.% Ni/H-Y-5.1.

**Reduced 5 wt.% Fe/H-Y-5.1** exhibited poor activity in the HDO of isoeugenol. Analogous results were obtained by Fang et al. [45] in the HDO of guaiacol over Fe/CNT. Dihydroeugenol was formed as the main product with a yield of 73% and selectivity to the liquid phase products visible in GC analysis of 96% along with traces of 1,2-dimethoxy-4-propylbenzene. Complete conversion of isoeugenol was reached after 60 min (**Figure 22a**). The carbon balance in the liquid phase was ca. 80%.

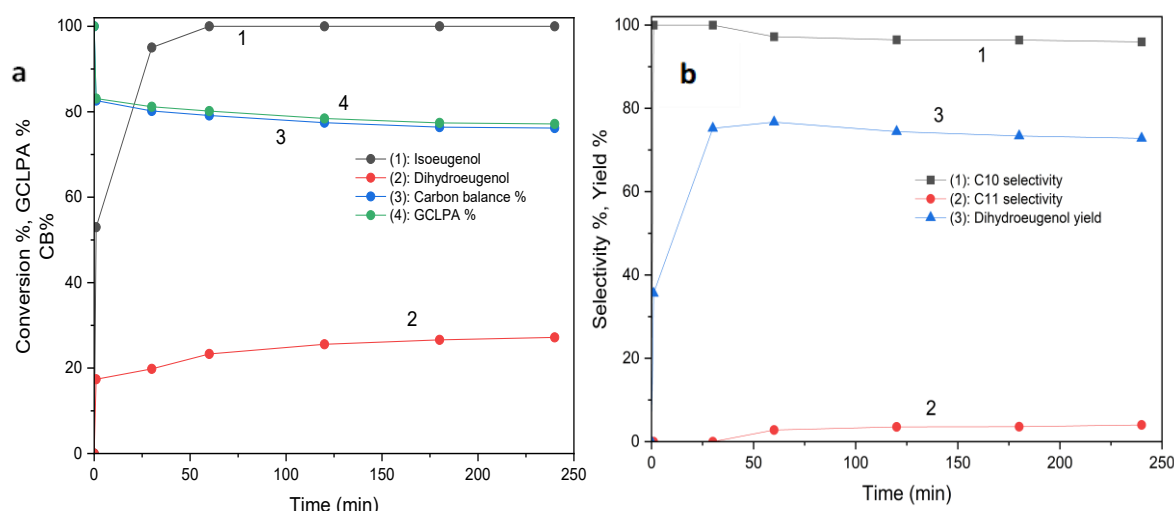


**Figure 22:** a) Conversion of isoeugenol, dihydroeugenol, GCLPA% and CB% versus time and b) selectivity to products by the carbon number and the yield versus time over 5 wt.% Fe/H-Y-5.1

**Reduced monometallic 5 wt.% Ni/H-Y-5.1** showed high activity in the HDO of isoeugenol with complete conversion of dihydroeugenol after 240 min but poor selectivity implying that reaction pathways for various products have similar rates (**Figure 23a**). It is known from the

literature that Ni is active in the hydrogenation of aromatic rings due to its ability to efficiently dissociate H<sub>2</sub> [42],[45]. In this work, light hydrocarbons were detected in the catalytic reaction of isoeugenol over Ni/H-Y-5.1 with the yields of 19% methyl heptane (2 and 3) and 18% methyl hexane (2 and 3). Similarly, methylated butane, pentane, octane, and nonane were formed. Detection of these compounds in high concentrations indicates that ring-opening took place over Ni/H-Y-5.1 catalyst. The C-C bond hydrogenolysis of the reactant followed by cracking on the Brønsted acid sites of the acidic zeolitic support might have produced light paraffins. It has been reported that in the HDO of guaiacol (a compound similar to isoeugenol), demethylation and ring-opening take place at high temperatures [114]. Tran et al. [114] observed ring-opening of guaiacol due to high C-C bond hydrogenolysis activity of Ni in the HDO of guaiacol over an acidic Ni/Al-MCM-41 catalyst.

The yields of cyclic compounds, i.e., propylcyclohexane, ethyl-methylcyclohexane, and butylcyclopentane were 5%, 6%, and 2%, respectively. A combined yield of 28% was obtained for the products that could not be identified by GC-MS. The compounds formed in the gas phase were not identified, therefore analysis of the gas phase should be conducted in the future.

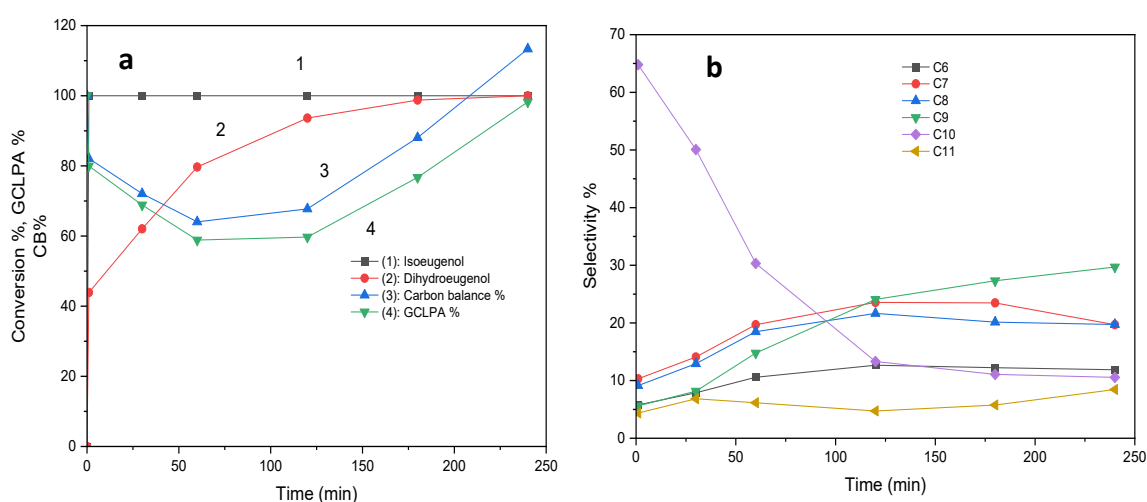


**Figure 23: a)** Conversion of isoeugenol, dihydroeugenol, GCLPA% and CB% versus time and **b)** selectivity by the carbon number and the yield versus time over 5 wt.% Ni/H-Y-5.1.

The calculated yield and the carbon balance for the products formed in the liquid phase over Ni/H-Y-5.1 catalyst were exceeding 100%, which can be explained by the following reasons:

- Calibration values for quantification by GC analysis of all products were not determined, but estimated based on their molecular weights, carbon numbers, and proximity of GC retention times to the calibrated compounds.
- Some compounds could not be identified by GC-MS. Hence, their calibration also needed to be approximated based on their GC retention time.
- Cracking of the solvent on the acid sites of the catalyst.

**Reduced bimetallic 5 wt.% Fe - 5 wt.% Ni/H-Y-5.1** exhibited high activity and reasonable selectivity in the HDO of isoeugenol. There was a complete conversion of dihydroeugenol after 2 hours of the reaction. The yields of propylcyclohexane, ethyl-methylcyclohexane, butylcyclopentane, and propylbenzene were 18%, 15%, 7%, and 3%, respectively. The GC retention times of the products along with the names of the compounds formed in the catalytic HDO reaction over this catalyst are shown in **Figure 24** and **Table 18**. The molar concentrations of the products, the reactant conversion, the carbon balance, GCLPA%, and selectivity % are shown in **Figure 25**. An almost 3.5-fold increase in the yields of these compounds and a considerable decrease in the yields of light hydrocarbons were observed, compared to the monometallic Ni/H-Y-5.1 catalyst. The reduction in the yield of light hydrocarbons might be due to a decline in ring-opening reactions and less acid sites, as the acid sites can crack the bigger hydrocarbons. Although the acidity of the Fe-Ni/H-Y-5.1 was not determined, it most probably exhibits lower acidity than its parent zeolite as in [43,109]. The qualitative gas phase analysis showed the presence of methane and propane.

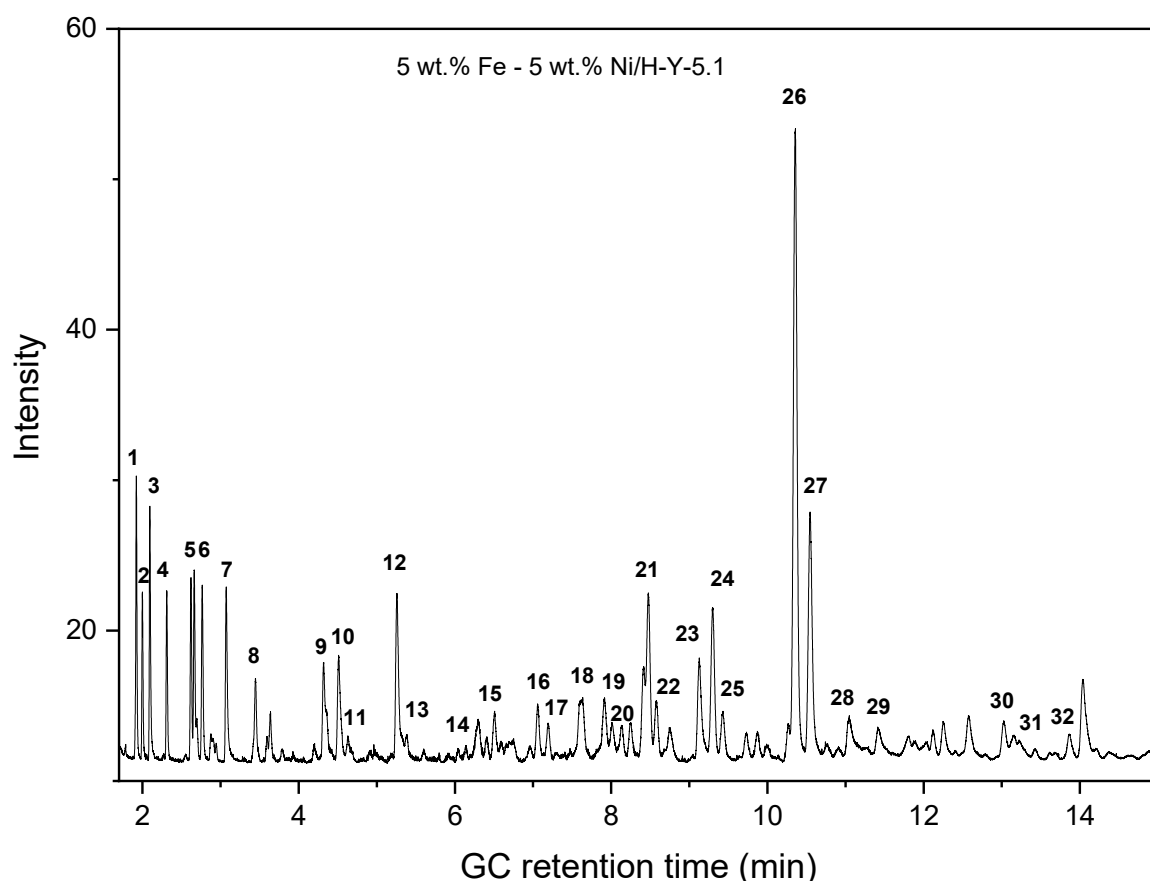


**Figure 24:** GC retention times of the products formed during the HDO of isoeugenol with 5 wt.% Fe - 5 wt.% Ni/H-Y-5.1.

A reaction yield of over 100% in the liquid phase was obtained similar to those obtained over Ni/H-Y-5.1. GCLPA was found to be ca. 72%. Additionally, an increase in GCLPA% and carbon balance was observed with increasing reaction duration (also observed in Ni/H-Y-5.1).

Possible reasons for the increment in carbon balance and GCLPA % with the increase in reaction time are:

- At the beginning of the reaction, the phenolics could have been strongly adsorbed to the catalyst. As the reaction proceeds, the aromatic ring is hydrogenated, and the products desorb to the bulk liquid.
- The gas-phase products could have reacted with cyclohexane derivatives in the liquid-phase producing alkylated compounds.
- The cracked products were formed from the solvent (n-hexadecane).

**Table 18:** Name of the products formed during the HDO of isoeugenol with 5 wt.% Fe - 5 wt.% Ni/H-Y-5.1 as identified by GC-MS.

Number (same as Figure 23)	GC retention time (min)	Name of compound	Yield %
1	1.921	2-methylpentane	2
2	2	3-methylpentane	
3	2.094	hexane	n/d
4	2.311	methylcyclopentane	3
5	2.62	cyclohexane	7
6	2.765+2.882	2-methylhexane + 3-methylhexane	6
7	3.072	heptane	n/d
8	3.447	methylcyclohexane	4
9	4.32	2-methylheptane	10
10	4.512	3-methylheptane	
11	4.631	1,2-dimethyl-trans-cyclohexane	2
12	5.257	octane	n/d
13	5.381	1,2-dimethyl-cis-cyclohexane	same as 11
14	6.297	1,3,5-trimethylcyclohexane	same as 16,17
15	6.505	2,5-dimethylheptane	
16	7.059	1,2,4-trimethylcyclohexane	9
17	7.191	1,3,5-trimethylcyclohexane	
18	7.623	2-methyloctane	6
19	7.913	3-methyloctane	
20	8.012+8.135+8.248	1,2,4-trimethylcyclohexane (cis+trans)	same as 16,17
21	8.476	1-ethyl-3-methylcyclohexane	15
22	8.577	1-ethyl-4 methyl-trans-cyclohexane	
23	9.128	nonane	n/d
24	9.3	1-ethyl-4 methyl-trans-cyclohexane	same as 21, 22
25	9.429	1-ethyl-4 methyl-cis-cyclohexane	
26	10.357	propylcyclohexane	18
27	10.546	butylcyclopentane	7
28	11.04	propylbenzene	3
29	11.447	1-ethyl-2-methylbenzene	4

30	13.027	1,2,3-trimethylbenzene	—
31	13.155	1-methyl-3-propylcyclohexane	—
32	13.866	1-methyl-2-propylcyclohexane	—

**Note:** hexane, heptane, octane, and nonane are not considered in the mass balance and yield calculations. The yields of all dimethylcyclohexane and trimethylcyclohexane are combined.

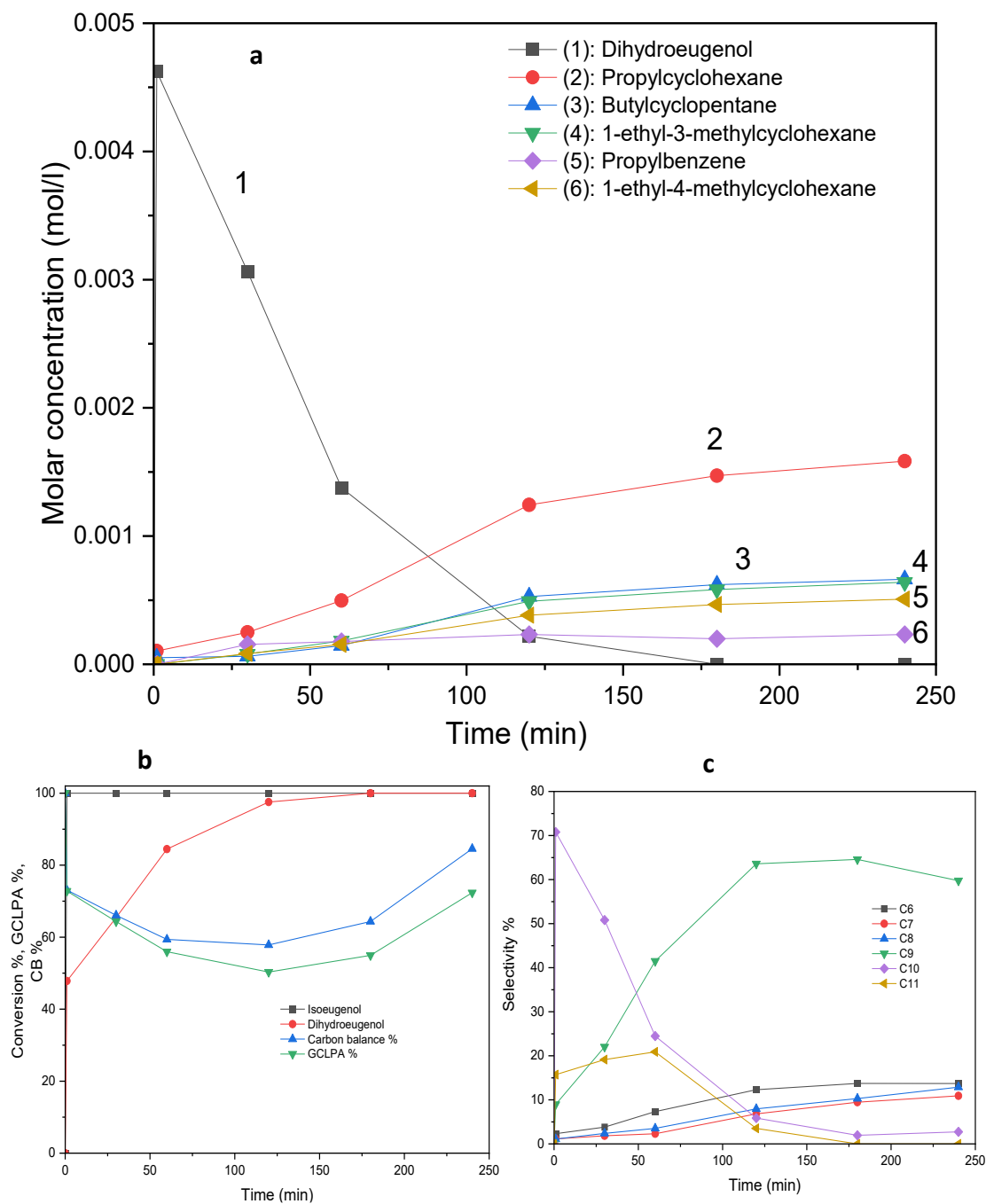


**Figure 25:** a) Molar concentrations of the products versus time, b) conversion of isoeugenol, dihydroeugenol, GCLPA% and CB% versus time, and c) selectivity by the carbon number versus time over 5 wt.% Fe - 5 wt.% Ni/H-Y-5.1.

Fe/H-Y-5.1 showed no deoxygenation activity, hence, an increase in the yields of deoxygenated aromatics and cycloalkanes over bimetallic Fe-Ni compared to the monometallic Ni catalyst is due to the synergy between Fe and Ni sites. There are several studies in the literature stating that bimetallic Fe-Ni catalysts exhibit better HDO performance than monometallic Ni catalysts due to the synergistic effect between Fe and Ni [42,43,55]. A decrease in the average metal particle size and an increase in the relative H<sub>2</sub>-TPR area of the bimetallic catalyst compared to the monometallic Ni catalyst obtained from the characterization results suggest interactions between Fe and Ni. The results from isoeugenol transformation over these catalysts are presented in **Table 19**.

**Table 19:** The results from HDO of isoeugenol over Fe, Ni, and Fe-Ni catalysts. Nomenclature: DH (dihydroeugenol) and PCH (propylcyclohexane).

Entry	Catalyst	Initial rate for isoeugenol transformation (mol/s/g <sub>cat</sub> )	Conversion of DH after 4 h (%)	Yield of DH after 4 h (%)	GCLPA (%)	Yield of PCH (%) at 80 % conversion of DH (after 4 h)
1	5 wt.% Fe/H-Y-5.1	8.9*10 <sup>-5</sup>	27	73	77	0 (0)
2	5 wt.% Ni/H-Y-5.1	1.4*10 <sup>-4</sup>	100	0	98	2 (5)
3	5 wt.% Fe - 5 wt.% Ni /H-Y-5.1	1.5*10 <sup>-4</sup>	100	0	72	7 (18)

### Proposed reaction pathway

In the HDO of isoeugenol with a bimetallic Fe-Ni catalyst, 1,2-dimethoxy-4-propylbenzene as an intermediate was already formed in the 1<sup>st</sup> minute of the reaction. Tieuli et al.[18] stated that heavy products such as 1,2-dimethoxy-4-propylbenzene are formed in the HDO of isoeugenol with an acidic catalyst. Formation of 1,2-dimethoxy-4-propylbenzene implies that there is fast dehydration of dihydroeugenol to 2-methoxy-4-propylbenzene and then methoxylation to 1,2-dimethoxy-4-propylbenzene. Due to the fast reaction step, the intermediate 2-methoxy-4-propylbenzene is not observed.

In this study, 2-methoxy-4-propylcyclohexanol, 2-methoxy-4-propylcyclohexanone, and 4-propyl-1,2-cyclohexanediol were not observed, indicating that the hydrogenation of aromatic ring occurs after the demethylation and demethoxylation reactions. The major deoxygenated products of the reaction, which are propylcyclohexane and butylcyclopentane were also formed already in the 1<sup>st</sup> minute. Such fast generation of these compounds indicates that the aromatic ring hydrogenation proceeds rapidly in combination with ring contraction on the acidic sites of the H-Y-5.1 support (**steps 1–9 Figure 26**). For cyclohexane and propylcyclohexane, the ring contraction generates methylcyclopentane and

butylcyclopentane, respectively. Shafaghat et al. [43] have reported formation of similar products (methylcyclopentane and methylcyclohexane) in the HDO of simulated phenolic bio-oil over Ni, Fe, and Fe-Ni/H-Beta.

In HDO of isoeugenol, 4-propylphenol and 1-propylcyclohexene were also formed as intermediates. The formation of 1-propylcyclohexene implies that the Ni particles with sizes of over 11 nm are less active in the phenyl ring hydrogenation compared to Pt on zeolites used by Bomont et al. [23], where no such intermediate was formed [18]. Propylcyclohexene intermediate was also observed by Tieuli et al. [18] in the HDO of isoeugenol over Ni/SBA-15 mesoporous catalyst containing Ni particles of around 20 nm.

As depicted in **Figure 26**, demethoxylation in the HDO of isoeugenol is subsequently followed by dehydration on the acidic sites and hydrogenation of the ring on the metal sites to form propylcyclohexane. Han et al. [42] observed that methoxy groups in eugenol HDO were removed by demethoxylation instead of demethylation over Fe-Ni/MCSs, which is in accordance with this work. The authors [42] stated that the propyl side chain of eugenol did not undergo hydrogenolysis. However, over bimetallic Fe-Ni/H-Y-5.1, the propyl side chain of isoeugenol underwent hydrogenolysis after ring hydrogenation. This might be because the H-Y-5.1 support is more acidic than the MCSs, which indicates that acidic sites are needed to break the alkyl side chain of isoeugenol. Bomont et al. [23] obtained analogous results with removal of the propyl chain after ring hydrogenation over an acidic Pt/H-Beta catalyst.

The results suggest that addition of Fe facilitates deoxygenation but suppresses the hydrogenation activity of Ni, such as phenolic ring-opening compared to the monometallic Ni catalyst [42]. The possible synergy between formed Fe-Ni sites and Ni sites, which are needed to activate C–O bonds and dissociate H<sub>2</sub> for dehydroxylation reaction, respectively, facilitates the HDO of isoeugenol for the formation of aromatics and cycloalkanes [42].

The bimetallic Fe-Ni catalyst was found to have high activity in alkyl transfer (transalkylation) reactions. Various alkylated products of cyclohexane, such as ethyl-methylcyclohexane (yield of 15%), methylcyclohexane, dimethylcyclohexane, and trimethylcyclohexane were formed. Zhu et al. have stated that the Brønsted acid sites of H-Beta catalyze methyl transfer reactions from the methoxy group to the aromatic ring in the HDO of anisole over Pt/H-Beta. The presence of active Pt improves the rate of cleavage of the methoxy bond and thus the rate of transalkylation. In Fe-Ni/H-Y-5.1 catalyst, the Brønsted acid sites of H-Y-5.1 might catalyze methyl transfer reactions with the synergy of Fe-Ni sites, as more alkylated products were observed on the bimetallic catalyst than on the monometallic catalyst.

In both Ni and Fe-Ni catalysts supported on an acidic H-Y-5.1 zeolite, hexane, heptane, octane, and nonane were formed as the products. These might have been formed by cracking of nonane formed after the ring-opening of propylcyclohexane or as a result of the cracking of the solvent.

Based on the product identification with GC-MS, the following reaction network was proposed for the isoeugenol HDO over Fe-Ni/H-Y-5.1.

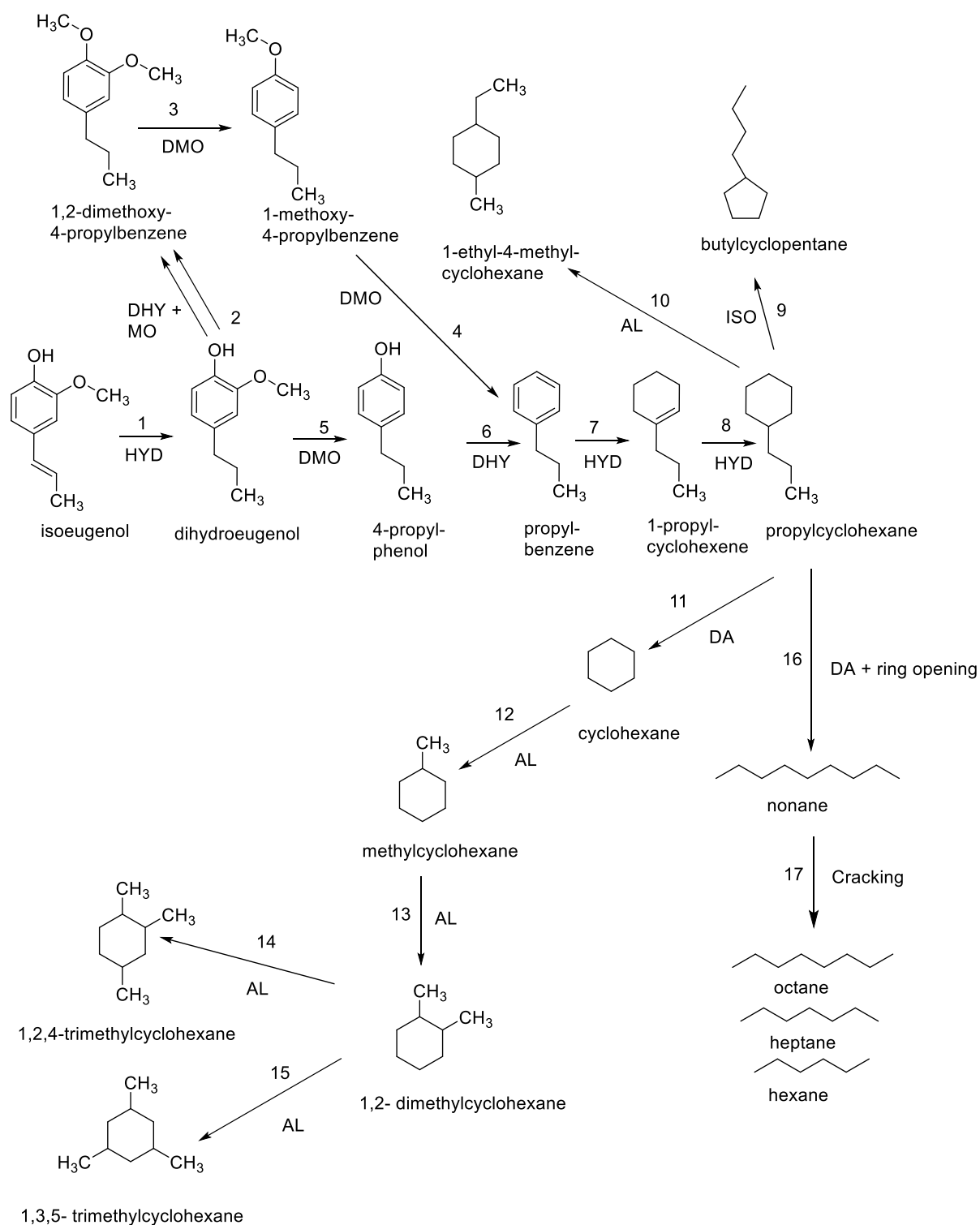


**Figure 26:** The proposed reaction pathways for the HDO of isoeugenol over Fe-Ni/H-Y-5.1.

Nomenclature used:

HYD: hydrogenation  
 DMO: demethoxylation  
 DHY: dehydration

MO: methoxylation  
 DA: dealkylation  
 AL: alkylation

## 4 Conclusions and Recommendations

As the world is transitioning away from fossil fuels, lignocellulosic biomass is scrutinized as a source of renewable fuels and chemicals. Political motivations and environmental concerns have increased the research in lignin, an underutilized resource currently, as a potential source of bio-oils. However, bio-oils obtained for example by fast pyrolysis need to be catalytically upgraded to reduce their oxygen content making them compatible with the current petroleum-based infrastructures. Since bio-oils are a complicated mixture of many aromatic compounds, a lignin-derived phenolic compound isoeugenol was selected as a model compound for this study. The catalytic hydrodeoxygenation reaction (HDO) of isoeugenol was conducted over different Fe-, Ni-, and Fe-Ni-based catalysts supported on zeolites in a batch reactor at 300 °C and 30 bar total pressure for 3 hours or 4 hours with hexadecane as a solvent. Iron was chosen for the metal modifications of zeolites because it is inexpensive, oxophilic, and environmentally friendly. This thesis aims to contribute to the ever-growing knowledge of the HDO of phenolic compounds as the HDO of isoeugenol over Fe- and Fe-Ni-based catalysts was conducted for the first time in this work.

The review of the relevant literature revealed that Fe-Ni bimetallic catalysts are more active in the HDO of phenolic compounds than their monometallic counterparts due to the synergistic effects of these metals. Activity of the Fe-Ni bimetallic catalysts was found to follow a volcanic curve depending on the mass ratios between Fe and Ni. There are only a few papers in the literature about the HDO of phenolic compounds over Fe-based catalysts. Monometallic Fe was found to be a compromise between activity and selectivity in the HDO reactions as it removes oxygen selectively from phenolic compounds by direct deoxygenation with low H<sub>2</sub> consumption but exhibits low activity.

In this study, various Fe-, Ni-, and Fe-Ni modified catalysts were synthesized and characterized to study the influence of Fe precursors, methods of preparation, acidity, metal loading, and zeolitic structure on the catalytic performance. The SEM images of the prepared catalysts showed that the catalysts retained their structures after Fe-introduction, and TEM images indicated presence of highly dispersed nanoparticles in the prepared catalysts. Fe species in the prepared catalysts were mainly in the hematite (Fe<sub>2</sub>O<sub>3</sub>) form, according to the XRD and Mössbauer results. H<sub>2</sub>-TPR studies indicated that the Ni species were easier to be reduced than Fe species, as the Fe particles need a higher temperature for complete reduction. The specific surface areas and acid sites of all the studied catalysts decreased after the metal modifications as observed previously for other catalytic systems.

Unreduced Fe-based catalysts exhibited poor activity in the HDO of isoeugenol in the applied operating conditions. A lot of cracking products were formed, and it was difficult to identify them by GC-MS. It was also difficult to assess the origin of the products as cracking of the solvent was observed in a blank experiment performed with the solvent and the catalyst. Only the reduced 9.5 wt.% Fe/H-Beta-38-FeCl<sub>3</sub> showed slight deoxygenation activity visible through formation of 4-propyl phenol of ca. 6% and traces of propylcyclohexane. Poor performance of Fe might be due to the presence of Fe in the hematite form for unreduced catalysts or rapid catalyst deactivation due to blockage of the catalyst pores by strong

adsorption and trapping of phenolics during the experiments. Even in reduced catalysts, Fe was observed mostly in the magnetite form. Because the desired deoxygenated products such as propylcyclohexane were not formed over the initially selected Fe-based catalysts, a suite of Fe, Ni, and Fe-Ni catalysts on H-Y-5.1 support was prepared to study the synergistic effects of bimetallic catalysts.

A reduction temperature of 500 °C was chosen for the set of catalysts on H-Y-5.1 support based on the obtained H<sub>2</sub>-TPR profiles. The synthesized Fe-based catalysts exhibited a high metal dispersion according to TEM imaging. However, the reduced 5 wt.% Fe/H-Y-5.1 displayed low activity in the HDO of isoeugenol following the same trend as other studied Fe-based catalysts. Dihydroeugenol with a yield of 73% was formed as the main product over this catalyst.

The reduced 5 wt.% Ni/H-Y-5.1 exhibited high hydrogenation activity but poor selectivity in the HDO of isoeugenol. Ni nanoparticles with an average size of 19 nm were found to be active in aromatic ring hydrogenation and ring-opening reactions leading to formation of light hydrocarbons. The aromatic ring-opening reactions are not desirable due to a relatively high H<sub>2</sub> consumption. The yield of the desired product propylcyclohexane was just 5% after 4 hours. The carbon balance exceeding 100% suggests cracking of the solvent over this catalyst. Although complete HDO of isoeugenol was achieved over this catalyst, it was not selective towards the desired deoxygenated aromatic and cyclic compounds.

The reduced bimetallic 5 wt.% Fe - 5 wt.% Ni/H-Y-5.1 (with Fe to Ni weight ratio of 1:1) exhibited both high activity and reasonable selectivity in the HDO of isoeugenol. This was the best catalyst of all the tested Fe-based catalysts in this work. The yields of the desired deoxygenated compounds such as propylcyclohexane, ethyl-methylcyclohexane, butylcyclopentane, and propylbenzene were 18%, 15%, 7%, and 3%, respectively. An almost 3.5-fold increase in the yields of these compounds and a considerable decrease in the yields of light hydrocarbons were observed, compared to the monometallic Ni/H-Y-5.1 catalyst.

The average nanoparticles size in the prepared bimetallic Fe-Ni catalyst was 11nm being 8 nm smaller than for the monometallic Ni catalyst. Such decrease in the average metal particle size, diffraction peaks of NiO phase, and an increase in the relative H<sub>2</sub>-TPR area of the bimetallic catalyst compared to the monometallic Ni catalyst indicate the synergy between Fe and Ni particles. The Fe-Ni sites are needed to activate C–O bonds while Ni sites are required for H<sub>2</sub> dissociation and subsequent dehydroxylation. The synergy between these two sites facilitates the HDO of isoeugenol to form cycloalkanes and deoxygenated aromatics. This study shows that application of two relatively cheap metals Fe and Ni in tandem over a zeolitic support has a potential to produce an efficient HDO catalyst. The results obtained from this study are in accordance with the literature where bimetallic catalysts have exhibited better performance in the HDO of phenolic compounds compared to the respective monometallic catalysts due to the synergy between Fe and Ni metallic sites.

HDO of isoeugenol over mostly unreduced Fe-based catalysts was carried in this work. HDO activity of Fe/H-Beta-38 catalyst was improved after reduction at 500 °C. Hence, further

experiments could be performed with reduced Fe-based catalysts prepared by ferric acetate precursor, which exhibited excellent metal dispersion.

HDO of isoeugenol over Fe-Ni-based bimetallic catalysts should be further investigated with different weight ratios of Fe and Ni as the HDO activity of the bimetallic catalysts can be fine-tuned by adjusting the Fe to Ni ratio. Interactions between Fe and Ni active sites could also be clarified by characterization of catalysts with different Fe to Ni ratios. Reaction should be conducted at 350 °C to study the adsorption of phenolics on the catalyst surface as adsorption and retention of phenolics decrease with increasing temperature. Similarly, characterization could be done to study coke deposition inside the pores of the zeolitic supports. The GC calibration of the products should be done to obtain more precise results. Quantification of the acid sites of the synthesized catalysts should be done to better explain the obtained catalytic results. Further experiments should be done by varying the reduction temperatures of the catalysts to see the effects of reduction temperatures on the HDO of isoeugenol as reduction temperature influences the oxidation state of the Fe-modified catalysts. Additionally, solventless HDO experiments should be conducted, which would make product identification and calculations simpler. Such experiments are the most relevant in the context of eventual industrial implementation.

## 5 References

- [1] A.M. Robinson, J.E. Hensley, J.W. Medlin, *ACS Catal.* **2016**, 6, 5026–5043.
- [2] P. Mäki-Arvela, D.Y. Murzin, *Catalysts* **2017**, 7, 265.
- [3] J. Zakzeski, P.C.A. Bruijninx, A.L. Jongerius, B.M. Weckhuysen, *Chem. Rev.* **2010**, 110, 3552–3599.
- [4] M. Saidi, F. Samimi, D. Karimipourfard, T. Nimmanwudipong, B.C. Gates, M. Reza Rahimpour, *Energy Environ. Sci.* **2014**, 7, 103–129.
- [5] S. Kasakov, H. Shi, D. M. Camaioni, C. Zhao, E. Baráth, A. Jentys, J. A. Lercher, *Green Chem.* **2015**, 17, 5079–5090.
- [6] A.P.P. Pires, Y. Han, J. Kramlich, M. Garcia-Perez, *BioResources* **2018**, 13, 2632–2657.
- [7] P. Mäki-Arvela, M. Martínez-Klimov, D.Yu. Murzin, *Fuel* **2021**, 306, 121673.
- [8] X. Zhu, L.L. Lobban, R.G. Mallinson, D.E. Resasco, *J. Catal.* **2011**, 281, 21–29.
- [9] P. Bajpai, *Pretreatment of Lignocellulosic Biomass for Biofuel Production*, Springer Singapore, Singapore, **2016**.
- [10] S. Sun, S. Sun, X. Cao, R. Sun, *Bioresour. Technol.* **2016**, 199, 49–58.
- [11] J. Ralph, K. Lundquist, G. Brunow, F. Lu, H. Kim, P.F. Schatz, J.M. Marita, R.D. Hatfield, S.A. Ralph, J.H. Christensen, W. Boerjan, *Phytochem. Rev.* **2004**, 3, 29–60.
- [12] A.V. Bridgwater, *Biomass Bioenergy* **2012**, 38, 68–94.
- [13] M. Sharifzadeh, M. Sadeqzadeh, M. Guo, T.N. Borhani, N.V.S.N. Murthy Konda, M.C. Garcia, L. Wang, J. Hallett, N. Shah, *Prog. Energy Combust. Sci.* **2019**, 71, 1–80.
- [14] P. M. Mortensen, D. Gardini, H.W.P. de Carvalho, C. D. Damsgaard, J.-D. Grunwaldt, P. A. Jensen, J. B. Wagner, A. D. Jensen, *Catal. Sci. Technol.* **2014**, 4, 3672–3686.
- [15] A. Demirbas, *Appl. Energy* **2011**, 88, 17–28.
- [16] N.K.G. Silva, R.A.R. Ferreira, R.M. Ribas, R.S. Monteiro, M.A.S. Barrozo, R.R. Soares, *Fuel* **2021**, 287, 119509.
- [17] C. Teles, R. Rabelo Neto, G. Jacobs, B. Davis, D. Resasco, F. Noronha, *ChemCatChem* **2017**, 9, 2850–2863.
- [18] S. Tieuli, P. Mäki-Arvela, M. Peurla, K. Eränen, J. Wärnå, G. Cruciani, F. Menegazzo, D.Yu. Murzin, M. Signoretto, *Appl. Catal. Gen.* **2019**, 580, 1–10.
- [19] M. Zhang, Y. Hu, H. Wang, H. Li, X. Han, Y. Zeng, C.C. Xu, *Mol. Catal.* **2021**, 504, 111438.
- [20] T.M.H. Dabros, M.Z. Stummann, M. Høj, P.A. Jensen, J.-D. Grunwaldt, J. Gabrielsen, P.M. Mortensen, A.D. Jensen, *Prog. Energy Combust. Sci.* **2018**, 68, 268–309.
- [21] C. Lindfors, P. Mäki-Arvela, P. Paturi, A. Aho, K. Eränen, J. Hemming, M. Peurla, D. Kubička, I.L. Simakova, D.Yu. Murzin, *ACS Sustain. Chem. Eng.* **2019**, 7, 14545–14560.
- [22] M. Alda-Onggar, P. Mäki-Arvela, K. Eränen, A. Aho, J. Hemming, P. Paturi, M. Peurla, M. Lindblad, I.L. Simakova, D.Yu. Murzin, *ACS Sustain. Chem. Eng.* **2018**, 6, 16205–16218.
- [23] L. Bomont, M. Alda-Onggar, V. Fedorov, A. Aho, J. Peltonen, K. Eränen, M. Peurla, N. Kumar, J. Wärnå, V. Russo, P. Mäki-Arvela, H. Grénman, M. Lindblad, D.Y. Murzin, *Eur. J. Inorg. Chem.* **2018**, 24, 2841–2854.
- [24] C. Zhang, J. Xing, L. Song, H. Xin, S. Lin, L. Xing, X. Li, *Catal. Today* **2014**, 234, 145–152.
- [25] J. Qi, X. Sun, S.-F. Tang, Y. Sun, C. Xu, X. Li, X. Li, *Appl. Catal. Gen.* **2017**, 535, 24–31.
- [26] T. Nimmanwudipong, R.C. Runnebaum, S.E. Ebeler, D.E. Block, B.C. Gates, *Catal. Lett.* **2012**, 142, 151–160.
- [27] X. Li, L. Chen, G. Chen, J. Zhang, J. Liu, *Renew. Energy* **2020**, 149, 609–616.
- [28] A. Bjelić, M. Grilc, B. Likozar, *Chem. Eng. J.* **2020**, 394, 124914.

- [29] L. Hu, X.-Y. Wei, Y.-H. Kang, X.-H. Guo, M.-L. Xu, Z.-M. Zong, *J. Energy Inst.* **2021**, 96, 269–279.
- [30] A.E. Coumans, E.J.M. Hensen, *Catal. Today* **2017**, 298, 181–189.
- [31] M. Anand, A.K. Sinha, *Bioresour. Technol.* **2012**, 126, 148–155.
- [32] H.W. Lee, B.R. Jun, H. Kim, D.H. Kim, J.-K. Jeon, S.H. Park, C.H. Ko, T.-W. Kim, Y.-K. Park, *Energy* **2015**, 81, 33–40.
- [33] A. Corma, *J. Catal.* **2003**, 216, 298–312.
- [34] J. Weitkamp, *Solid State Ion.* **2000**, 131, 175–188.
- [35] E. Koohsaryan, M. Anbia, *Chin. J. Catal.* **2016**, 37, 447–467.
- [36] Y. Tao, H. Kanoh, L. Abrams, K. Kaneko, *Chem. Rev.* **2006**, 106, 896–910.
- [37] S. Kulprathipanja, *Zeolites in Industrial Separation and Catalysis*, John Wiley & Sons, **2010**.
- [38] V.R. Stamenkovic, B.S. Mun, M. Arenz, K.J.J. Mayrhofer, C.A. Lucas, G. Wang, P.N. Ross, N.M. Markovic, *Nat. Mater.* **2007**, 6, 241–247.
- [39] J.R. Kitchin, J.K. Nørskov, M.A. Barteau, J.G. Chen, *J. Chem. Phys.* **2004**, 120, 10240–10246.
- [40] J. Rebelli, M. Detwiler, S. Ma, C.T. Williams, J.R. Monnier, *J. Catal.* **2010**, 270, 224–233.
- [41] J. Xu, T. White, P. Li, C. He, J. Yu, W. Yuan, Y.-F. Han, *J. Am. Chem. Soc.* **2010**, 132, 10398–10406.
- [42] Q. Han, M.U. Rehman, J. Wang, A. Rykov, O.Y. Gutiérrez, Y. Zhao, S. Wang, X. Ma, J.A. Lercher, *Appl. Catal. B Environ.* **2019**, 253, 348–358.
- [43] H. Shafaghat, P.S. Rezaei, W.M.A.W. Daud, *J. Ind. Eng. Chem.* **2016**, 35, 268–276.
- [44] Y. Shi, E. Xing, K. Wu, J. Wang, M. Yang, Y. Wu, *Catal. Sci. Technol.* **2017**, 7, 2385–2415.
- [45] H. Fang, J. Zheng, X. Luo, J. Du, A. Roldan, S. Leoni, Y. Yuan, *Appl. Catal. Gen.* **2017**, 529, 20–31.
- [46] X. Xu, E. Jiang, Z. Li, Y. Sun, *Fuel* **2018**, 221, 440–446.
- [47] P.S. Rezaei, H. Shafaghat, W.M.A.W. Daud, *Green Chem.* **2016**, 18, 1684–1693.
- [48] X. Yang, X. Cheng, A.A. Elzatahry, J. Chen, A. Alghamdi, Y. Deng, *Chin. Chem. Lett.* **2019**, 30, 324–330.
- [49] International Zeolite Association, *Database Zeolite Struct.* (n.d.).
- [50] P. Sirous-Rezaei, J. Jae, J.-M. Ha, C.H. Ko, J.M. Kim, J.-K. Jeon, Y.-K. Park, *Green Chem.* **2018**, 20, 1472–1483.
- [51] L. Nie, P.M. de Souza, F.B. Noronha, W. An, T. Sooknoi, D.E. Resasco, *J. Mol. Catal. Chem.* **2014**, 388–389, 47–55.
- [52] R.N. Olcese, M. Bettahar, D. Petitjean, B. Malaman, F. Giovanella, A. Dufour, *Appl. Catal. B Environ.* **2012**, 115–116, 63–73.
- [53] Y.-P. Zhao, F.-P. Wu, Q.-L. Song, X. Fan, L.-J. Jin, R.-Y. Wang, J.-P. Cao, X.-Y. Wei, *J. Energy Inst.* **2020**, 93, 899–910.
- [54] N. Zhao, Y. Zheng, J. Chen, *J. Energy Chem.* **2020**, 41, 194–208.
- [55] D. Han, W. Yin, D. Luo, H. He, S. Wang, S. Xia, *Fuel* **2021**, 305, 121545.
- [56] S.E.E. Misi, A. Ramli, *J. Appl. Sci.* **2011**.
- [57] T. Ishihara, K. Eguchi, H. Arai, *Appl. Catal.* **1987**, 30, 225–238.
- [58] S. Cheng, L. Wei, J. Julson, M. Rabnawaz, *Energy Convers. Manag.* **2017**, 150, 331–342.
- [59] M. Ishikawa, M. Tamura, Y. Nakagawa, K. Tomishige, *Appl. Catal. B Environ.* **2016**, 182, 193–203.
- [60] V.N. Bui, D. Laurenti, P. Afanasiev, C. Geantet, *Appl. Catal. B Environ.* **2011**, 101, 239–245.

- [61] R.N. Olcese, J. Francois, M.M. Bettahar, D. Petitjean, A. Dufour, *Energy Fuels* **2013**, 27, 975–984.
- [62] S.L. Yohe, H.J. Choudhari, D.D. Mehta, P.J. Dietrich, M.D. Detwiler, C.M. Akatay, E.A. Stach, J.T. Miller, W.N. Delgass, R. Agrawal, F.H. Ribeiro, *J. Catal.* **2016**, 344, 535–552.
- [63] A.K. Deepa, P.L. Dhepe, *ChemPlusChem* **2014**, 79, 1573–1583.
- [64] C. Ju, M. Li, Y. Fang, T. Tan, *Green Chem.* **2018**, 20, 4492–4499.
- [65] J. Sun, A.M. Karim, H. Zhang, L. Kovarik, X.S. Li, A.J. Hensley, J.-S. McEwen, Y. Wang, *J. Catal.* **2013**, 306, 47–57.
- [66] S. Yurdakal, C. Garlisi, L. Özcan, M. Bellardita, G. Palmisano, in: G. Marci, L. Palmisano (Eds.), *Heterog. Photocatal.*, Elsevier **2019**, 87–152.
- [67] J.-M. Jehng, I.E. Wachs, G.S. Patience, Y.-M. Dai, *Can. J. Chem. Eng.* **2021**, 99, 423–434.
- [68] C. Pirola, F. Galli, G.S. Patience, *Can. J. Chem. Eng.* **2018**, 96, 2317–2320.
- [69] P. Heidebrecht, V. Galvita, K. Sundmacher, *Chem. Eng. Sci.* **2008**, 63, 4776–4788.
- [70] Y.-S. Bae, A.Ö. Yazaydin, R.Q. Snurr, *Langmuir* **2010**, 26, 5475–5483.
- [71] B. Stuart, in: *Kirk-Othmer Encycl. Chem. Technol.*, American Cancer Society, **2015**, 1–18.
- [72] O.B. Belskaya, I.G. Danilova, M.O. Kazakov, R.M. Mironenko, A.V. Lavrenov, V.A. Likholobov, *FTIR Spectroscopy of Adsorbed Probe Molecules for Analyzing the Surface Properties of Supported Pt (Pd) Catalysts*, IntechOpen, **2012**.
- [73] H. Khan, A.S. Yerramilli, A. D’Oliveira, T.L. Alford, D.C. Boffito, G.S. Patience, *Can. J. Chem. Eng.* **2020**, 98, 1255–1266.
- [74] J. Haber, J.H. Block, B. Delmon, *Pure Appl. Chem.* **1995**, 67, 1257–1306.
- [75] X. Li, K. Zhu, J. Pang, M. Tian, J. Liu, A.I. Rykov, M. Zheng, X. Wang, X. Zhu, Y. Huang, B. Liu, J. Wang, W. Yang, T. Zhang, *Appl. Catal. B Environ.* **2018**, 224, 518–532.
- [76] P. Gütlich, *Z. Für Anorg. Allg. Chem.* **2012**, 638, 15–43.
- [77] C. De Blasio, *Fundamentals of Biofuels Engineering and Technology*, Springer International Publishing AG, Cham, SWITZERLAND, **2019**.
- [78] K. Maštovská, S.J. Lehotay, *J. Chromatogr. A* **2003**, 1000, 153–180.
- [79] M. Campanati, G. Fornasari, A. Vaccari, *Catal. Today* **2003**, 77, 299–314.
- [80] N. Kumar, P. Mäki-Arvela, S.F. Diáz, A. Aho, Y. Demidova, J. Linden, A. Shepidchenko, M. Tenhu, J. Salonen, P. Laukkanen, A. Lashkul, J. Dahl, I. Sinev, A.-R. Leino, K. Kordas, T. Salmi, D.Yu. Murzin, *Top. Catal.* **2013**, 56, 696–713.
- [81] M. Stekrova, P. Mäki-Arvela, N. Kumar, E. Behraves, A. Aho, Q. Balme, K.P. Volcho, N.F. Salakhutdinov, D.Yu. Murzin, *J. Mol. Catal. Chem.* **2015**, 410, 260–270.
- [82] E. Kholkina, N. Kumar, K. Eränen, M. Peurla, H. Palonen, J. Salonen, J. Lehtonen, D.Yu. Murzin, *Ultrason. Sonochem.* **2021**, 73, 105503.
- [83] D. Kubička, N. Kumar, P. Mäki-Arvela, M. Tiitta, V. Niemi, T. Salmi, D.Y. Murzin, *J. Catal.* **222** (2004) 65–79.
- [84] C.A. Emeis, *J. Catal.* **1993**, 141, 347–354.
- [85] C. Li, G. Xu, Y. Zhai, X. Liu, Y. Ma, Y. Zhang, *Fuel* **2017**, 203, 23–31.
- [86] D. Spreitzer, J. Schenk, *Steel Res. Int.* **2019**, 90, 1900108.
- [87] N. Zhu, Z. Lian, Y. Zhang, W. Shan, H. He, *Chin. Chem. Lett.* **2019**, 30, 867–870.
- [88] W.K. Jozwiak, E. Kaczmarek, T.P. Maniecki, W. Ignaczak, W. Maniukiewicz, *Appl. Catal. Gen.* **2007**, 326, 17–27.
- [89] Q. Yan, J. Li, X. Zhang, J. Zhang, Z. Cai, *Nanomaterials* **2018**, 8, 840.
- [90] M.A.A. Elmasry, A. Gaber, E.M.H. Khater, *J. Therm. Anal.* **1996**, 47, 757–763.
- [91] E.-K. Lee, K.-D. Jung, O.-S. Joo, Y.-G. Shul, *J. Mol. Catal. Chem.* **2005**, 239, 64–67.

- [92] J. Deng, J. Liu, W. Song, Z. Zhao, L. Zhao, H. Zheng, A. Chinghuan Lee, Y. Chen, J. Liu, *RSC Adv.* **2017**, 7, 7130–7139.
- [93] Y. Min Park, J. Min Cho, G. Young Han, J. Wook Bae, *Catal. Sci. Technol.* **2021**, 11, 3251–3260.
- [94] N. Martín, M. de L. Rodríguez, D. Solís-Casados, M. Viniegra, N. Martín, M. de L. Rodríguez, D. Solís-Casados, M. Viniegra, *J. Mex. Chem. Soc.* **2020**, 64, 327–338.
- [95] D. dos Santos Monteiro, M.O. da Guarda Souza, *J. Therm. Anal. Calorim.* **2016**, 123, 955–963.
- [96] G. Delahay, D. Valade, A. Guzmán-Vargas, B. Coq, *Appl. Catal. B Environ.* **2005**, 55, 149–155.
- [97] S. Song, G. Wu, W. Dai, N. Guan, L. Li, *Catal. Sci. Technol.* **2016**, 6, 8325–8335.
- [98] H.-Y. Lin, Y.-W. Chen, C. Li, *Thermochim. Acta* **2003**, 400, 61–67.
- [99] M. Nagai, O. Uchino, J. Okubo, S. Omi, *In. Stud. Surf. Sci. Catal.*, Elsevier **1997**, 105, 989–995.
- [100] J. Nováková, L. Kubelková, B. Wichterlová, T. Juška, Z. Dolejšek, *Zeolites* **1982**, 2, 17–22.
- [101] N. Czuma, K. Zarębska, M. Motak, M.E. Gálvez, P. Da Costa, *Fuel* **2020**, 267, 117139.
- [102] Z.X. Cheng, X.G. Zhao, J.L. Li, Q.M. Zhu, *Appl. Catal. Gen.* **2001**, 205, 31–36.
- [103] W. Gac, M. Greluk, G. Słowik, Y. Millot, L. Valentin, S. Dzwigaj, *Appl. Catal. B Environ.* **2018**, 237, 94–109.
- [104] X. Yu, J. Chen, T. Ren, *RSC Adv.* **2014**, 4, 46427–46436.
- [105] Z. Vajglová, N. Kumar, M. Peurla, J. Peltonen, I. Heinmaa, D. Yu. Murzin, *Catal. Sci. Technol.* **2018**, 8, 6150–6162.
- [106] Z. Vajglová, N. Kumar, P. Mäki-Arvela, K. Eränen, M. Peurla, L. Hupa, M. Nurmi, M. Toivakka, D.Y. Murzin, *Ind. Eng. Chem. Res.* **2019**, 58, 18084–18096.
- [107] R. Suerz, K. Eränen, N. Kumar, J. Wärnå, V. Russo, M. Peurla, A. Aho, D. Yu. Murzin, T. Salmi, *Chem. Eng. Sci.* **2021**, 229, 116030.
- [108] M. Stekrova, N. Kumar, S.F. Díaz, P. Mäki-Arvela, D.Yu. Murzin, *Catal. Today* **2015**, 241, 237–245.
- [109] D. Kubička, N. Kumar, T. Venäläinen, H. Karhu, I. Kubičková, H. Österholm, D.Yu. Murzin, *J. Phys. Chem. B* **2006**, 110, 4937–4946.
- [110] S. Zhang, H. Zhang, X. Liu, S. Zhu, L. Hu, Q. Zhang, *Fuel Process. Technol.* **2018**, 175, 17–25.
- [111] L. Sun, X. Zhang, L. Chen, B. Zhao, S. Yang, X. Xie, *J. Anal. Appl. Pyrolysis* **2016**, 121, 342–346.
- [112] Z. Li, W. Yi, Z. Li, X. Bai, P. Fu, C. Tian, Y. Zhang, *Energy Sources Part A: Recovery Util. and Environ. Eff.* **2020** 1–13.
- [113] A. Bjelić, M. Grilc, B. Likozar, *Chem. Eng. J.* **2018**, 333, 240–259.
- [114] N.T.T. Tran, Y. Uemura, A. Ramli, *Procedia Eng.* **2016**, 148, 1252–1258.

## 6 Appendix I: Experimental set-up



**Figure S1:** Batch reactor used for all experiments of HDO of isoeugenol.

## 7 Appendix II: SEM images

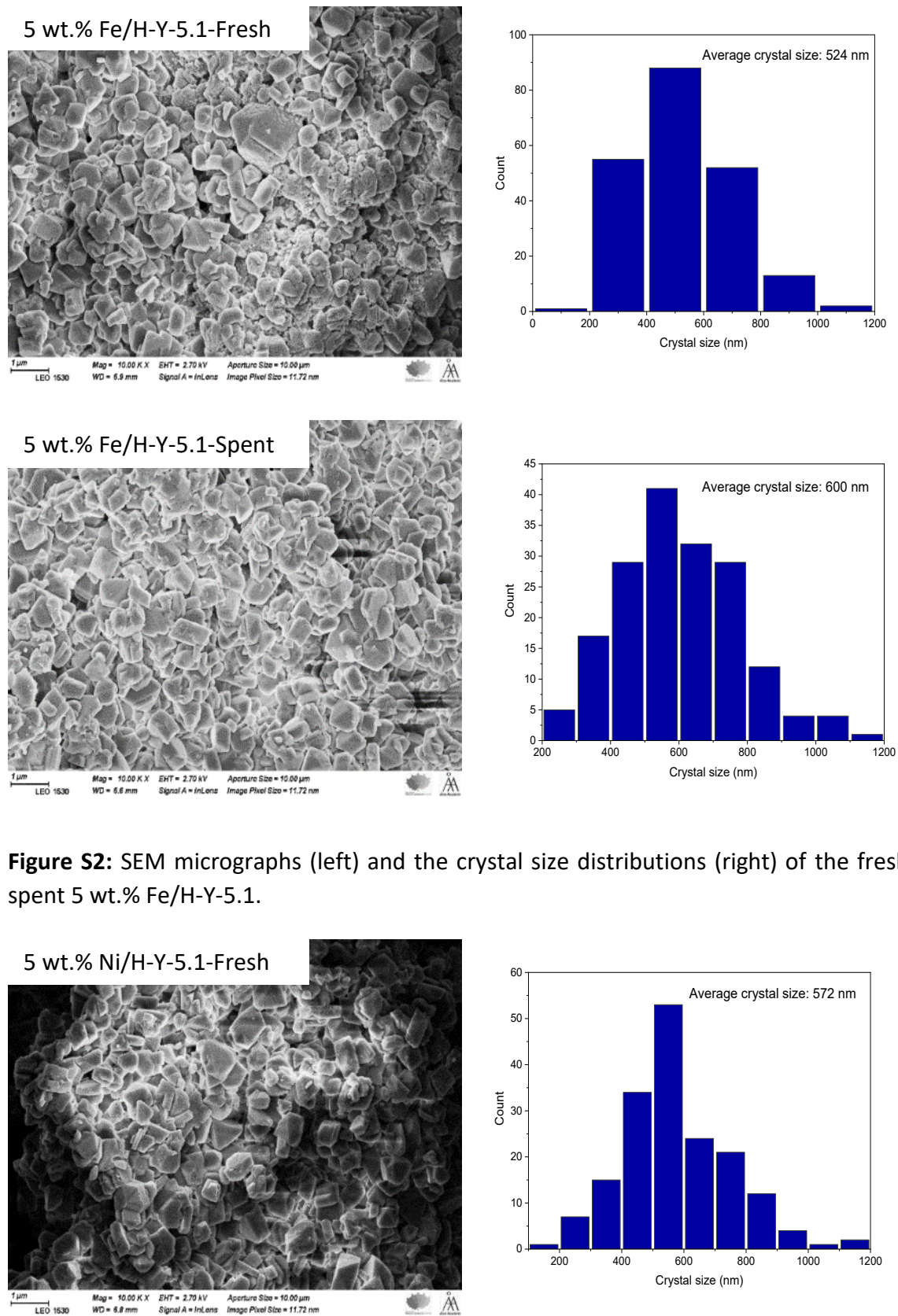


**Figure S2:** SEM micrographs (left) and the crystal size distributions (right) of the fresh and spent 5 wt.% Fe/H-Y-5.1.

5 wt.% Ni/H-Y-5.1-Spent

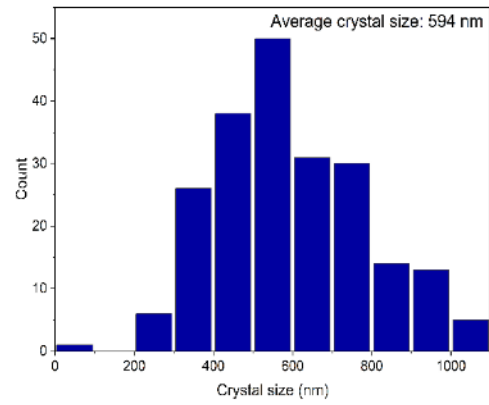
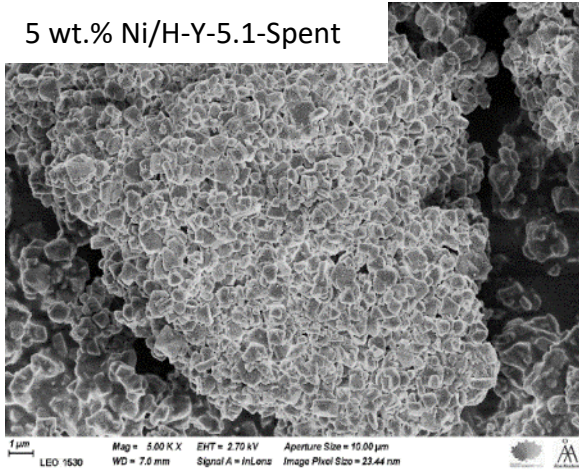
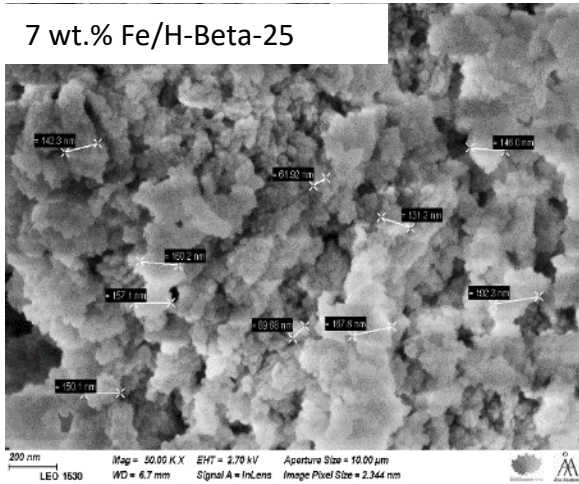
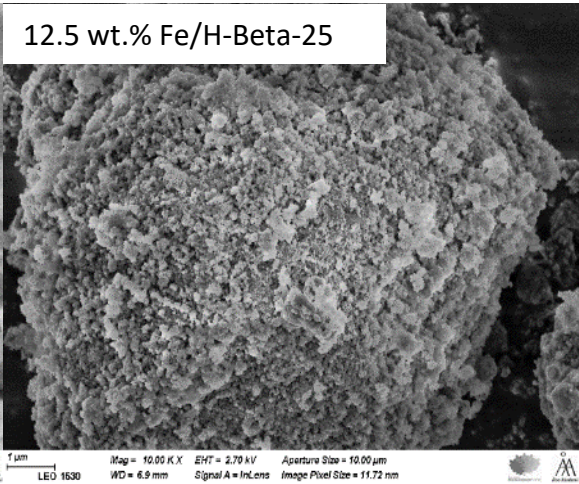


Figure S3: SEM micrographs (left) and the crystal size distributions (right) of the fresh and spent 5 wt.% Ni/H-Y-5.1.

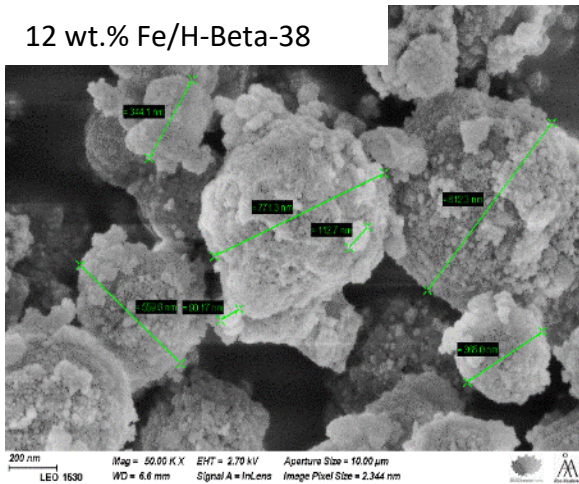
7 wt.% Fe/H-Beta-25



12.5 wt.% Fe/H-Beta-25



12 wt.% Fe/H-Beta-38



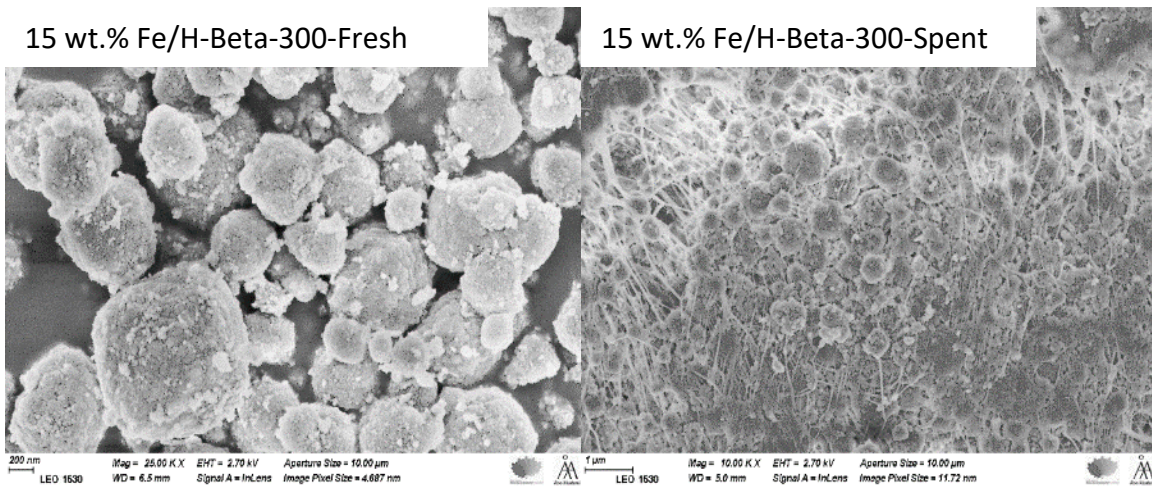
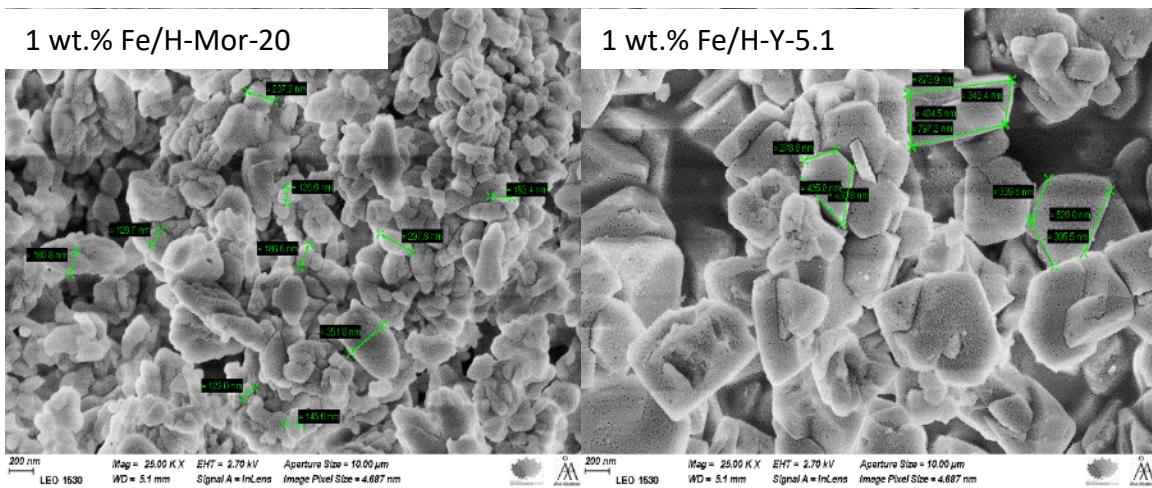
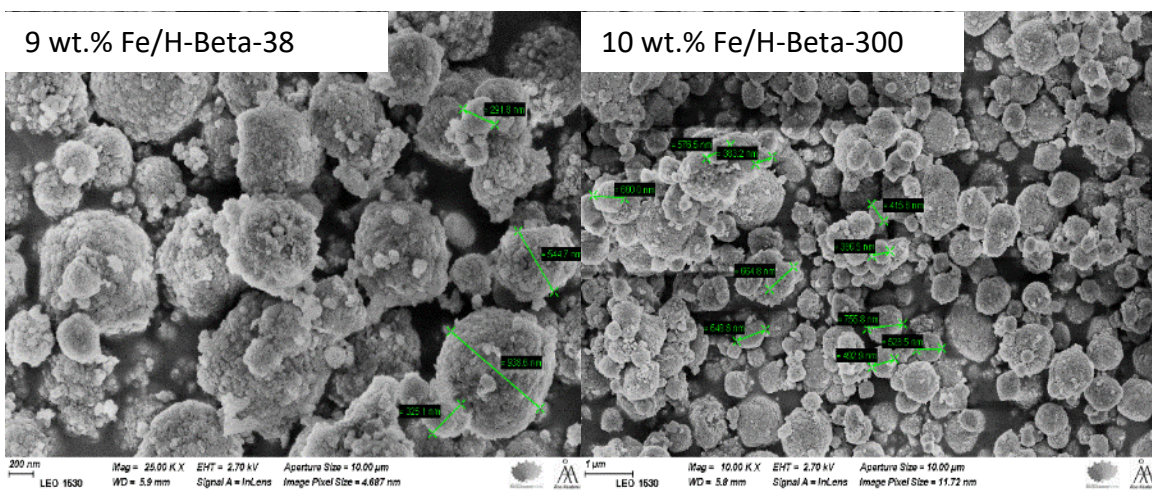
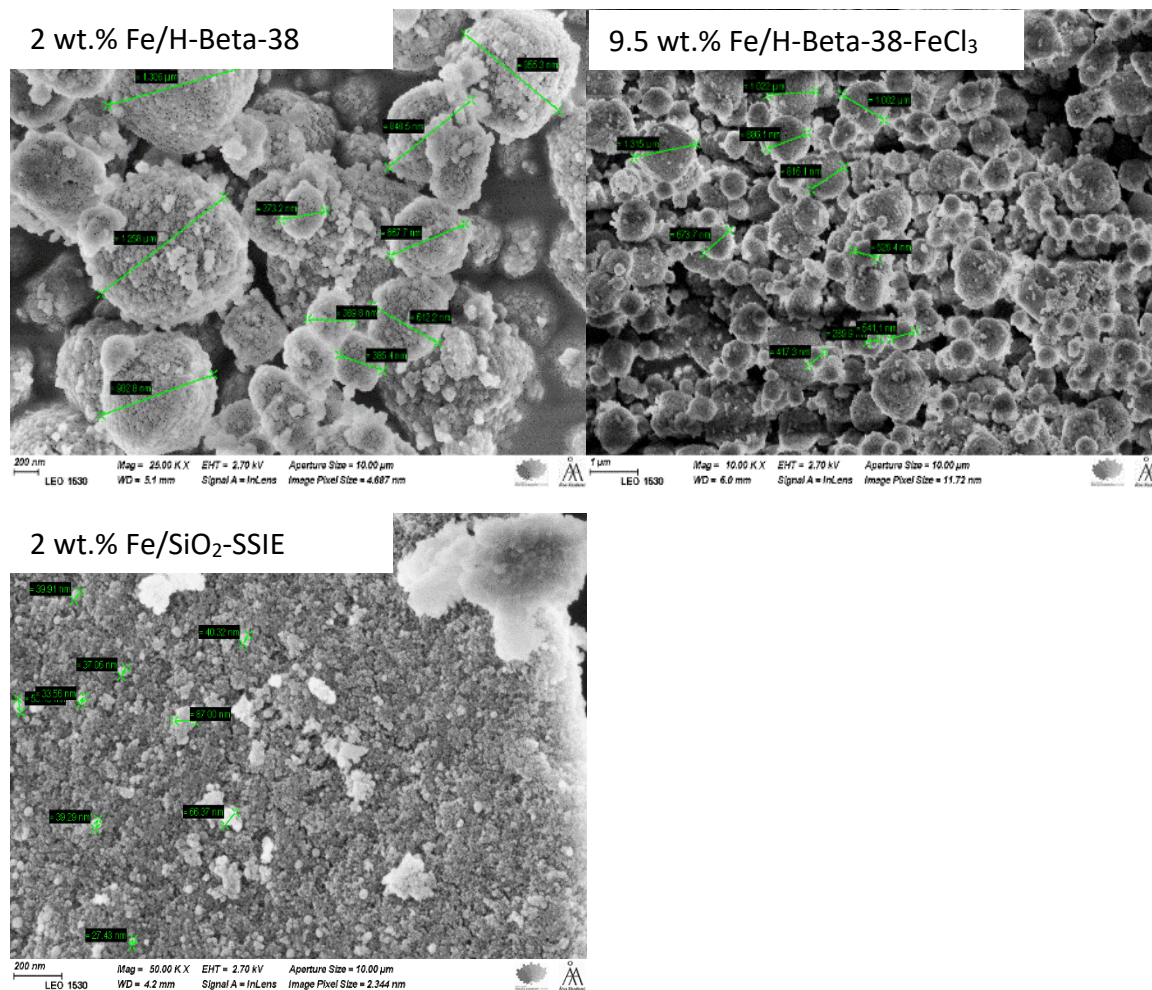


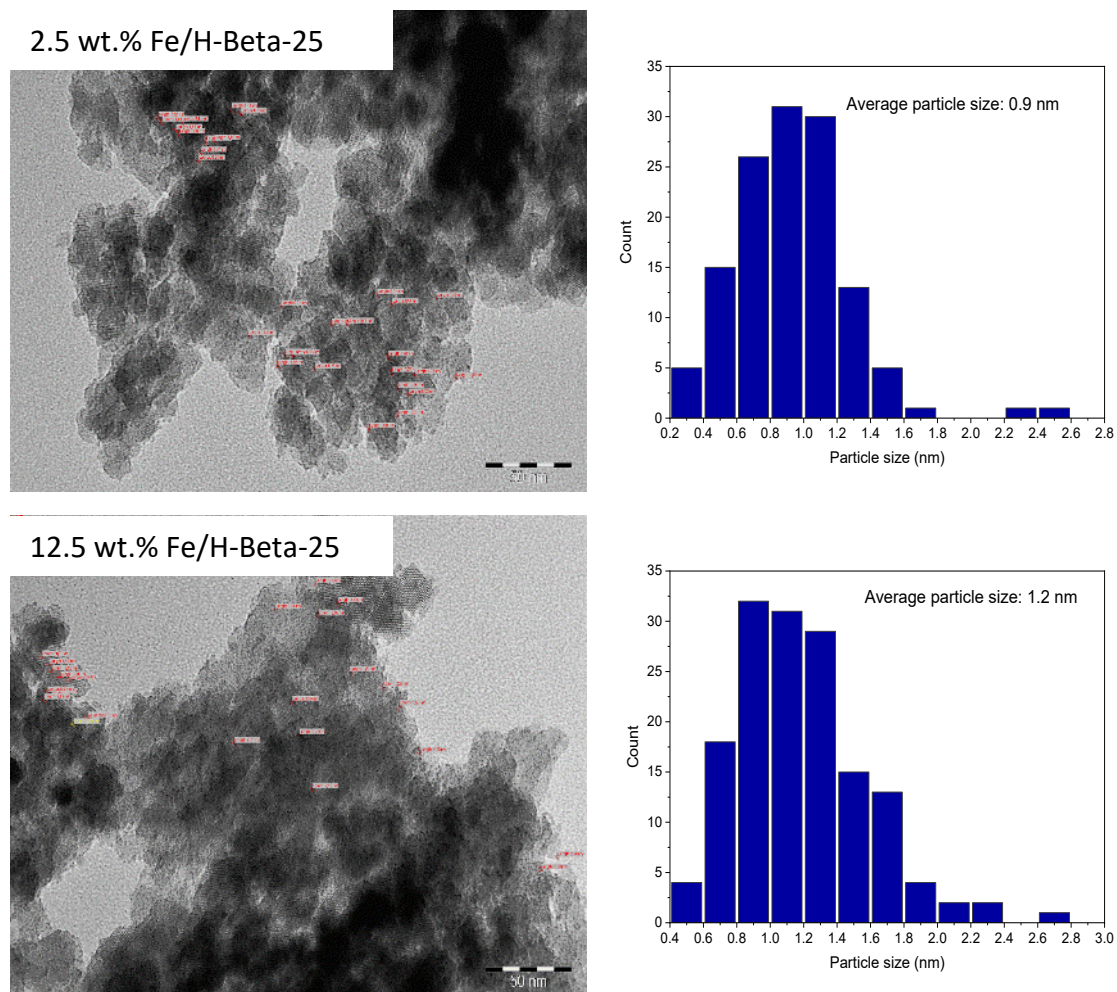
Figure S4: SEM images of Fe-modified catalysts prepared with the ferric acetate precursor.



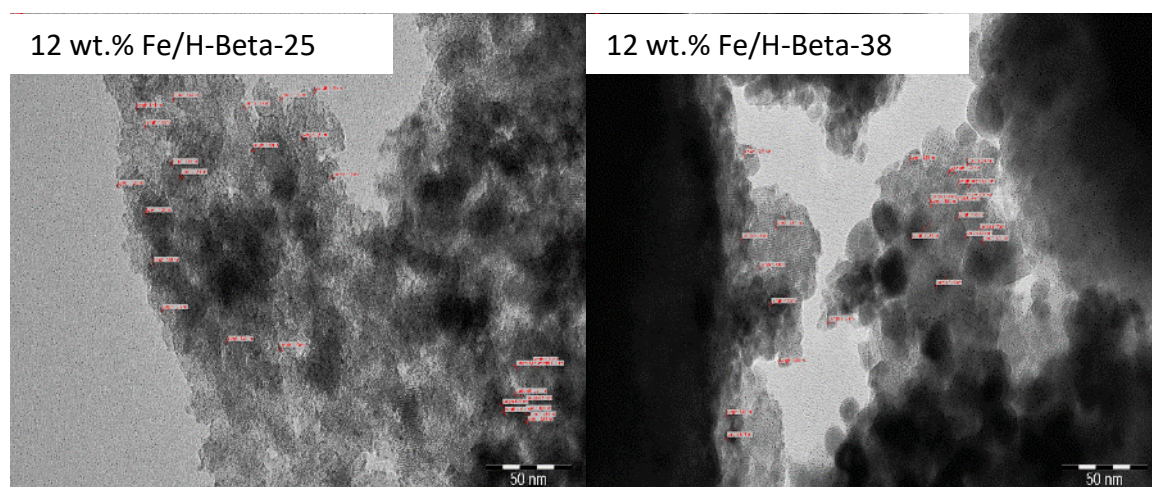


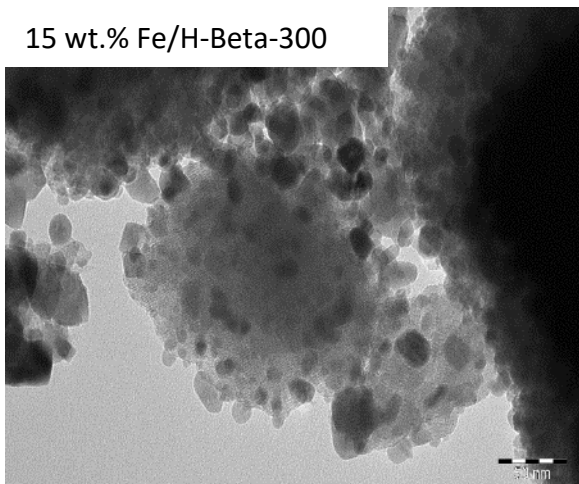
**Figure S5:** SEM images of Fe-modified catalysts prepared with the ferric nitrate precursor (first 5) and the ferric chloride precursor (last one).

## 8 Appendix III: TEM images

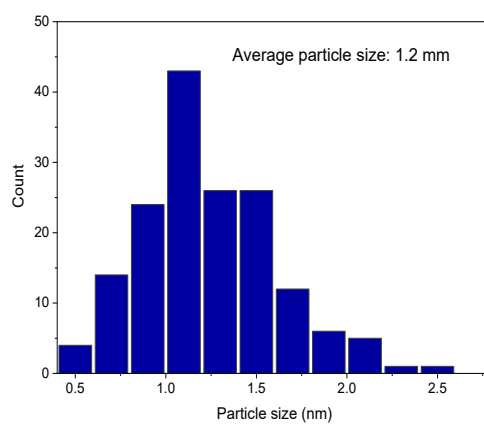
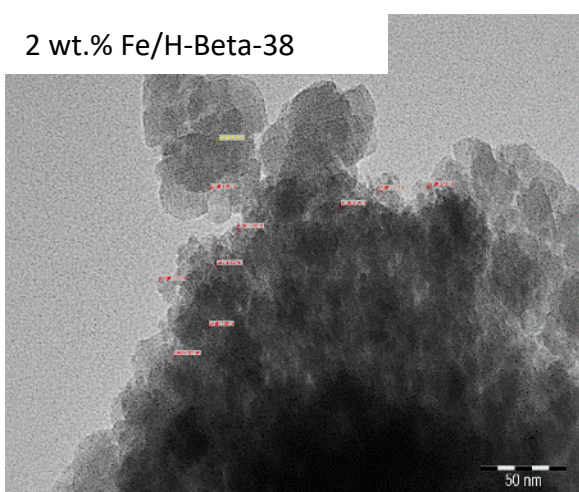


**Figure S6:** TEM images (left) and histograms (right) of Fe-modified catalysts prepared with the ferric acetate precursor.

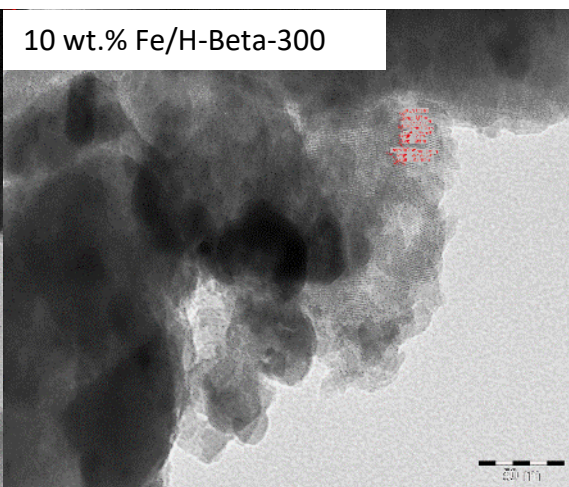
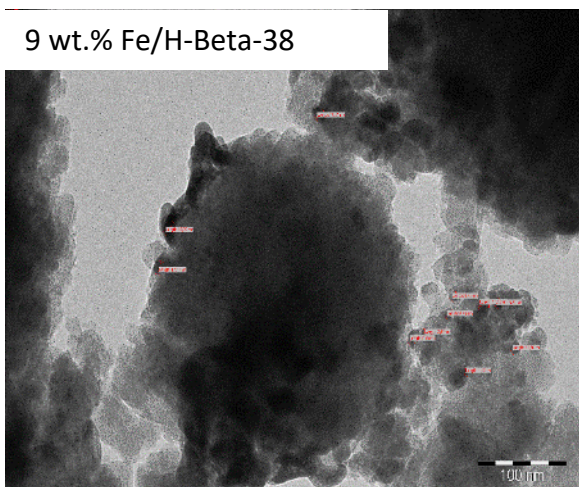




**Figure S7:** TEM images of Fe-modified catalysts prepared with the ferric acetate precursor.



**Figure S8:** TEM images (left) and histograms (right) of Fe-modified catalysts prepared with the ferric nitrate precursor.



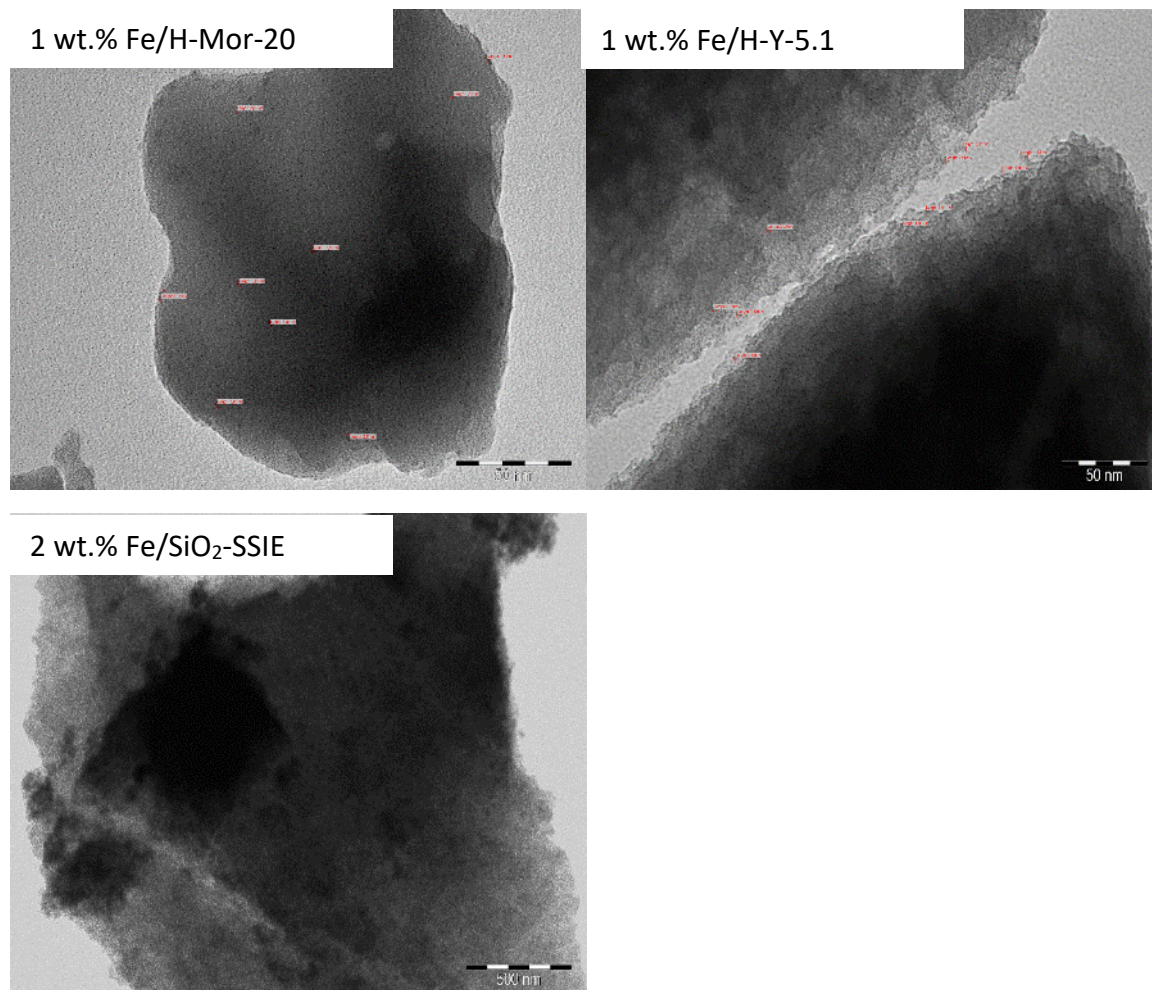


**Figure S9:** TEM images of Fe-modified catalysts prepared with the ferric nitrate precursor.

## 9 Appendix IV: Mössbauer spectra

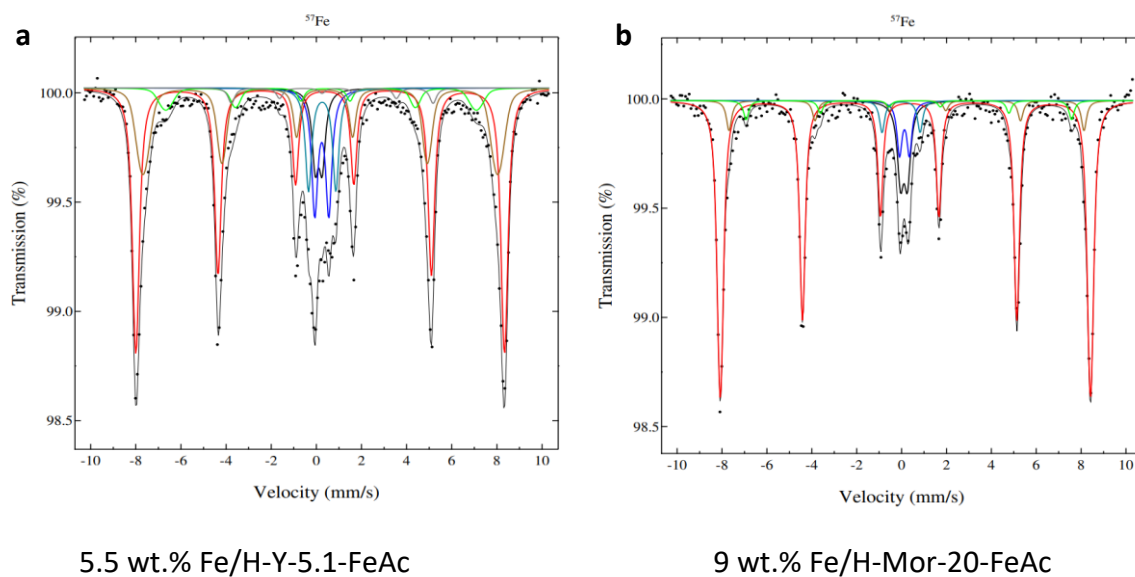


**Figure S10:** Mössbauer spectra of Fe-modified catalysts prepared with the ion-exchange method.

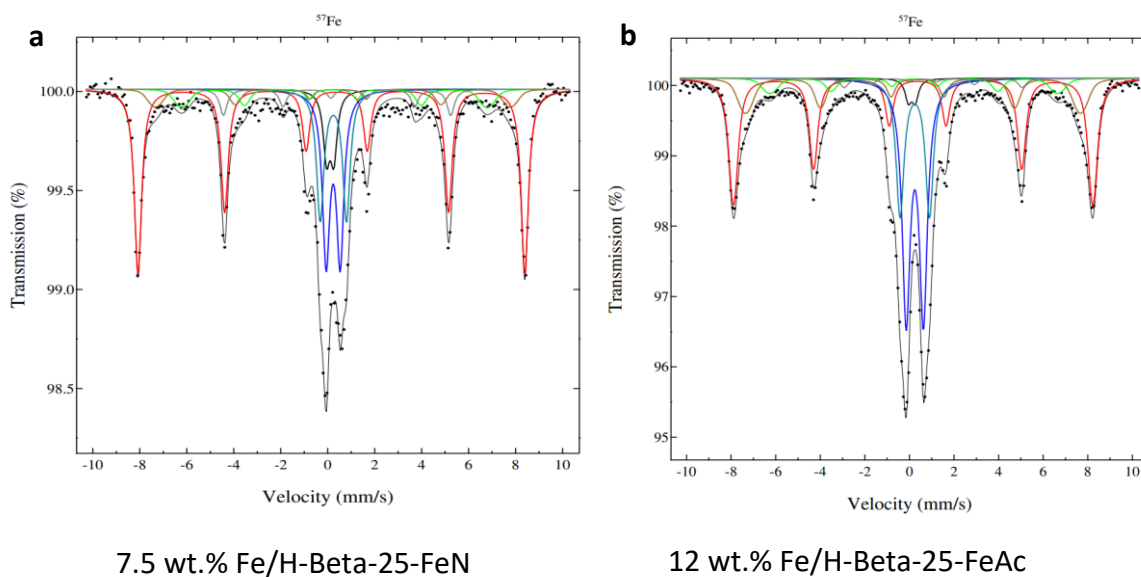


**Figure S11:** Mössbauer spectra of Fe-modified catalysts: **a**) 7.5 wt.% Fe/H-Beta-25-FeN synthesized by the evaporation-impregnation method **b**) 12 wt.% Fe/H-Beta-25-FeAc synthesized by the deposition-precipitation method.

## 10 Appendix V: Experiments performed in the HDO of isoeugenol

**Table S1: List of experiments performed in the HDO of isoeugenol**

**Operating conditions:** solvent: 100 ml hexadecane, reactant: 200 mg isoeugenol, pressure: 30 bar, stirring speed: 900 rpm, time: 3 hours or 4 hours, and temperature: 300 °C

Catalyst	Conversion of isoeugenol and GCLPA	selectivity of final products	Yield of final products	HDO %	Remarks
6.5 wt. % Fe/H-Beta-25-FeAc	100%, 70%	Dihydroeugenol (100%)	Dihydroeugenol (70%)	0	Unreduced catalyst, prepared with ion-exchange method. No cracking product observed.
12.5 wt. % Fe/H-Beta-25-FeAc	100%, 72%	Dihydroeugenol (100%)	Dihydroeugenol (72%)	0	Unreduced catalyst, prepared with ion-exchange method. No cracking product observed.
2 wt.% Fe/SiO <sub>2</sub>	100%, 80%	Dihydroeugenol (100%)	Dihydroeugenol (80%)	0	Unreduced catalyst used from another project.
2 wt.% Fe/H-Beta-38-FeNi	100%, 60%	Dihydroeugenol (100%)	Dihydroeugenol (60%)	0	Unreduced catalyst prepared by ion-exchange method.
1 wt.% Fe/H-Mor-20	100%, 75%	Dihydroeugenol (100%)	Dihydroeugenol (75%)	0	Unreduced catalyst prepared by ion-exchange method.
9.5 wt.% Fe-H-Beta-38-FeCl <sub>3</sub>	100%, 41%	Dihydroeugenol (100%)	Dihydroeugenol (41%)	0	Unreduced catalyst. Lots of cracking products formed which cannot be identified by GC-MS. GCLPA only included dihydroeugenol.
9.5 wt.% Fe-H-Beta-38-FeCl <sub>3</sub>	100%, 50%	Dihydroeugenol (86%) 4-propylphenol (12%), Propylcyclohexane (2%)	Dihydroeugenol (44%) 4-propylphenol (6%), propylcyclohexane (0.76%)	n/d	Reduced catalyst. Lots of cracking products formed which cannot be identified by GC-MS.

9 wt.% Fe/H-Beta-38-FeN	100%, 22%	Dihydroeugenol (100%)	Dihydroeugenol (22%)	n/d	Lots of cracking products formed that were difficult to be identified by GC-MS. GCLPA only included dihydroeugenol.
5 wt.% Fe/H-Y-5.1	100%, 77%	Dihydroeugenol (96%), 1,2-dimethoxypropylbenzene (4%)	Dihydroeugenol (73%), 1,2-dimethoxypropylbenzene (3%)	0	Reduced catalyst. Not active
5 wt.% Ni/H-Y-5.1	100%, 98%	methyl heptane (14%), methyl hexane (13%), propylcyclohexane (4%)	methyl heptane (19%), methyl hexane (18%), propylcyclohexane (5%)	100	Only nickel catalyst used in the project. Catalyst was reduced before the experiment. Active but not selective
5 wt.% Fe - 5 wt.% Ni /H-Y-5.1	100%, 72%	Propylcyclohexane (17%), ethylmethylcyclohexane (14%), butylcyclopentane (7%)	Propylcyclohexane (18%), ethylmethylcyclohexane (15%), butylcyclopentane (7%)	100	Only bimetallic Fe-Ni catalyst used in the project. Catalyst was reduced before the experiment. Active and selective towards aromatics and cycloalkanes.

## 11 Appendix VI: Mass spectra comparison

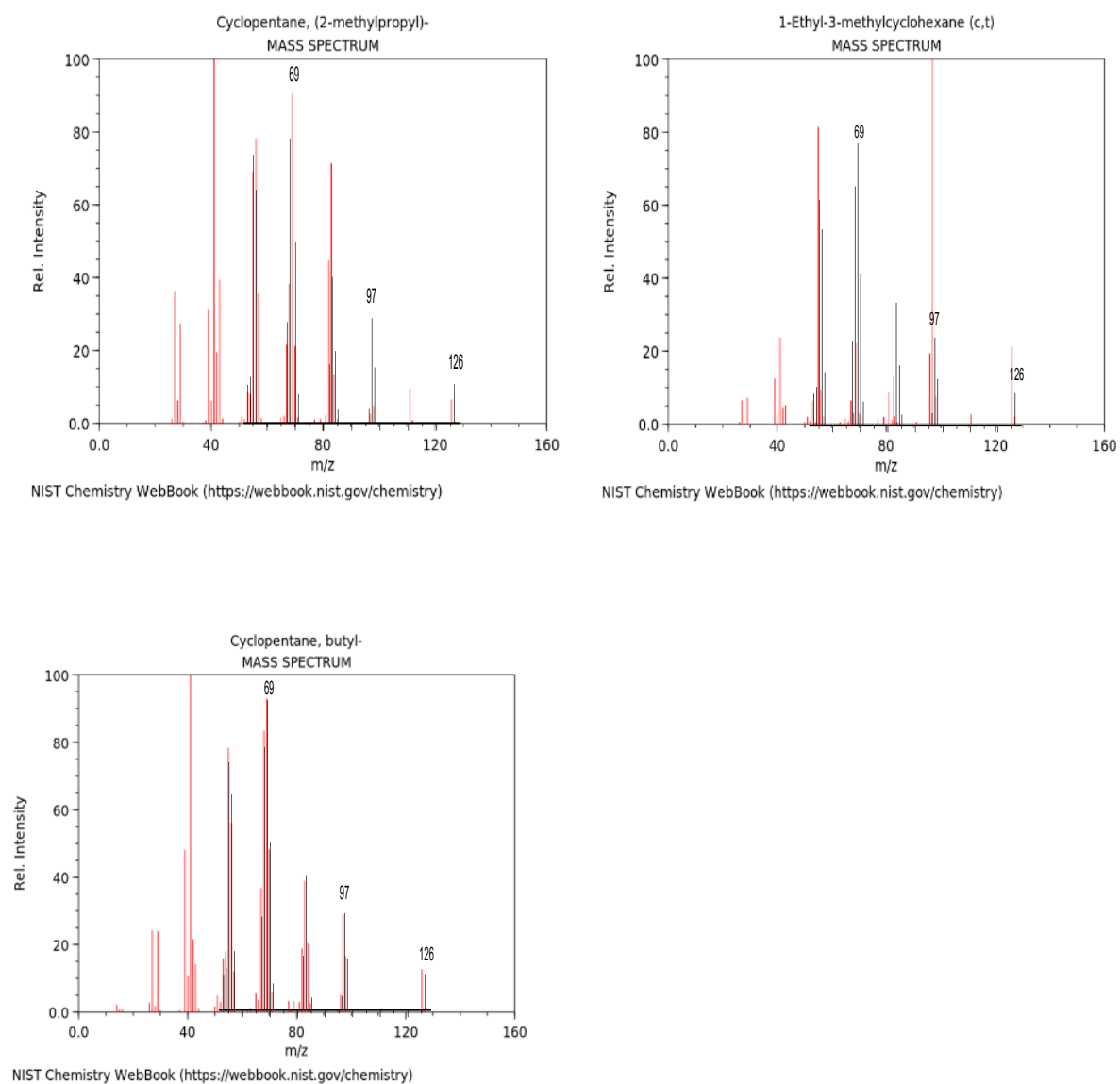


**Figure S12:** Comparison of the mass spectra to determine the compound formed with GC retention time of 10.5 min on 5 wt.% Ni/H-Y-5.1, and 5 wt.% Fe - 5wt.% Ni/H-Y-5.1. The best match was found to be with butylcyclopentane.